

DANIEL HEINRICH

ULTRAFAST COHERENT EXCITATION OF A $^{40}\text{Ca}^+$ ION

ULTRAFAST COHERENT EXCITATION OF A $^{40}\text{Ca}^+$ ION

DANIEL HEINRICH

Thesis submitted to the
Fakultät für Mathematik, Informatik und Physik
of the Leopold-Franzens-Universität Innsbruck,
in partial fulfillment of the requirements for the degree of

Doctor of Philosophy
(Physics)

Carried out under supervision of o. Univ.-Prof. Dr. Rainer Blatt at the Institut für
Quantenoptik und Quanteninformation, Innsbruck

November 2019

Hofstadter's Law:

It always takes longer than you expect,
even when you take into account Hofstadter's Law.

— Douglas Hofstadter

ABSTRACT

The ability to perform entangling gate operations between qubits is very important in modern physics. The duration of motional-sideband-resolving entangling gate operations in ion qubits has a physical lower limit on the order of tens of motional periods. This limits the number of gate operations that can be applied within the coherence time of the ion qubits. An entangling ultrafast phase gate operation has been proposed which can potentially be orders of magnitude faster than previous gates.

This thesis makes an experimental step towards realizing the ultrafast phase gate operation. It shows how to meet all requirements of the gate operation and details the last necessary steps towards its experimental implementation. In particular, the thesis presents experiments with a pulsed laser system which delivers picosecond pulses at a repetition rate of 5 GHz. It is resonant to the $4S_{1/2} \leftrightarrow 4P_{3/2}$ transition in $^{40}\text{Ca}^+$ for coherent population transfer to implement the ultrafast phase gate operation. The optical pulse train is derived from a mode-locked, stabilized optical frequency comb and inherits its frequency stability. Using a single trapped ion, four techniques are implemented for measuring the ion-laser coupling strength and characterizing the pulse train emitted by the laser. Finally, it is estimated that the realization of the gate operation requires a factor of 4 increase in the available laser intensity.

ZUSAMMENFASSUNG

Die Fähigkeit, Qubits zu verschränken, ist in der modernen Physik von großer Wichtigkeit. Die Zeitdauer von verschränkenden Quantengatteroperationen, die die Bewegungsseitenbänder von Ionenqubits spektral auflösen, ist physikalisch nach unten auf mehrere zehn Mikrosekunden begrenzt. Dies limitiert ebenso die Anzahl an Quantengatteroperationen, die innerhalb der Kohärenzzeit der Ionenqubits durchgeführt werden können. Eine verschränkende, ultraschnelle Phasengatteroperation wurde vorgeschlagen, die das Potenzial hat, um Größenordnungen schneller zu sein als bisherige Quantengatteroperationen.

Die vorliegende Arbeit macht einen Schritt in Richtung der Realisierung der ultraschnellen Phasengatteroperation. Die Arbeit zeigt, wie alle Voraussetzungen für die Implementierung der ultraschnellen Phasengatteroperation erfüllt werden können und führt die letzten, notwendigen Schritte zur experimentellen Umsetzung auf. Insbesondere werden Experimente mit einem gepulsten Lasersystem vorgestellt, das pikosekundenlange Pulse mit einer Repetitionsrate von 5 GHz aussendet, die resonant zum $4S_{1/2} \leftrightarrow 4P_{3/2}$ Übergang in $^{40}\text{Ca}^+$ sind und diesen kohärent anregen, um die ultraschnelle Phasengatteroperation zu verwirklichen. Der optische Pulszug nimmt seinen Ursprung in einem modengelockten und stabilisierten, optischen Frequenzkamm und erhält dessen Frequenzstabilität. Mithilfe eines einzelnen, gefangenen Ions werden vier Methoden angewendet, um die Ionen-Laser-Kopplungsstärke zu messen und den Pulszug zu charakterisieren. Schließlich zeigt eine Abschätzung, dass zur Realisierung der Gatteroperation die Intensität der Laserstrahlung noch um einen Faktor vier erhöht werden muss.

PUBLICATIONS

Some ideas and figures have appeared previously in the following publications:

- [1] M. Guggemos, D. Heinrich, Ó. A. Herrera-Sancho, R. Blatt, and C. F. Roos. “Sympathetic cooling and detection of a hot trapped ion by a cold one.” In: *New J. Phys.* 17.10 (2015), p. 103001. DOI: [10.1088/1367-2630/17/10/103001](https://doi.org/10.1088/1367-2630/17/10/103001).
- [2] D. Heinrich, M. Guggemos, M. Guevara-Bertsch, M. I. Hussain, C. F. Roos, and R. Blatt. *Ultrafast coherent excitation of a $^{40}\text{Ca}^+$ ion*. 2018. arXiv: [1812.08537v1](https://arxiv.org/abs/1812.08537v1).
- [3] D. Heinrich, M. Guggemos, M. Guevara-Bertsch, M. I. Hussain, C. F. Roos, and R. Blatt. “Ultrafast coherent excitation of a $^{40}\text{Ca}^+$ ion.” In: *New J. Phys.* 21.7 (2019), p. 073017. DOI: [10.1088/1367-2630/ab2a7e](https://doi.org/10.1088/1367-2630/ab2a7e).

ACKNOWLEDGMENTS

A work like this would not be possible without the support and encouragement of all the people directly and indirectly involved in its development. It was a lot of fun working in such a large group at the bleeding edge of quantum technology.

Therefore, I would first like to thank Rainer Blatt for giving me the opportunity to come to Innsbruck and join his group, and for having the confidence in me to tackle such an ambitious project.

The project would not even have existed without our senior scientists Mike Chwalla and Christian Roos. Even though the former left our group about a year after he initiated the project, he always helped with words and deeds during that time. The latter then took the lead of the project and always had an open ear for the problems that arose.

Another colleague, whose contributions to the project can not be overestimated is Michael Guggemos. We started our projects at about the same time and shared many ups and downs. Also, his successor, Milena Guevara-Bertsch and our PostDocs, Andrey Herrera-Sancho and Irtiza Hussain, all helped to advance the project and keep the apparatus running.

My appreciation also goes to the rest of the group, from Ben Ames to Florian Zähringer, for many helpful discussions that greatly helped to progress the project.

Many thanks are due to the administrative and other non-scientific staff: Markus Knabl, Elisabeth Huck, Doris Corona, Klaus Falschlunger, Valentin Staubmann, David Jordan, Thomas Holleis, Gerhard Hendl, Andreas Strasser, Bernhard Öttl and especially Stefan Haslwanter, whose expertise greatly helped in planing the trap and who manufactured most of its parts.

Last but not least, I want to say thank you to my family, especially my wife Alina, my parents, grandparents and my brother Simon. They have always supported me and made me feel loved and appreciated. Without them, I would not be who I am today.

Finally, I wish to thank everybody whom I may have forgotten above and ask your forgiveness. Thank you.

CONTENTS

I INTRODUCTION, THEORY AND PREREQUISITES

1	INTRODUCTION	3
2	TRAPPING $^{40}\text{Ca}^+$ IONS IN PAUL TRAPS	7
2.1	Paul traps	7
2.1.1	Quantum harmonic oscillator and phase space	8
2.1.2	Few ion crystals	11
2.2	The $^{40}\text{Ca}^+$ ion	15
2.3	Atom-light interaction	16
2.4	Electric field of a laser pulse	19
2.4.1	Temporally defined pulses	20
2.4.2	Spectrally defined pulses	20
3	QUANTUM INFORMATION PROCESSING WITH TRAPPED IONS	23
3.1	Quantum information, general	23
3.2	Quantum computation	26
3.3	Quantum computation with trapped ions	29
4	ULTRAFAST PHASE GATES	31
4.1	The GZC phase gate scheme	31
4.2	Pulse sequences for fast phase gates	36
4.2.1	Fast GZC gate scheme	36
4.2.2	Duan gate scheme	37
4.2.3	FRAG gate scheme	39
4.2.4	Comparison of fast gate schemes	42
4.3	Requirements for an experimental realization	43
4.3.1	GZC scheme in $^{40}\text{Ca}^+$	43
4.3.2	Requirements on a laser system for a fast phase gate operation	44

II THE LASER, EXPERIMENTAL SETUP AND RESULTS

5	A PULSED LASER SYSTEM FOR AN ULTRAFAST PHASE GATE OPERATION	49
5.1	Seed laser: an optical frequency comb	49
5.2	Pulse amplification and filtering	53
5.3	Pulse picking	56
5.3.1	Modes of operation	61
5.4	Frequency upconversion	62

6	LASER CHARACTERIZATION	69
6.1	Light spectra	69
6.2	FROG measurements	71
6.3	Pulse switching characteristics	77
7	EXPERIMENTAL SETUP	83
7.1	The ion trap	83
7.2	Laser systems and optical setup	85
7.3	Experimental control	89
7.3.1	Electronics	91
7.3.2	Software	93
8	EXPERIMENTAL RESULTS	95
8.1	Pulse simulation models	95
8.1.1	CW modes model	96
8.1.2	Quantum operation model	98
8.1.3	Lindblad master equation solving models	99
8.1.4	Simulation examples	100
8.2	Ion-state manipulation with pulses	101
8.2.1	Coherent population trapping	104
8.2.2	Coherent excitation using many pulses	107
8.2.3	Coherent excitation using few pulses	111
8.2.4	Single pulse with area π	113
8.2.5	Ramsey contrast decay and revival	116
8.2.6	Conclusion	120
III SUMMARY, OUTLOOK AND APPENDIX		
9	SUMMARY AND OUTLOOK	127
9.1	Summary	127
9.2	Outlook	129
9.3	Conclusions	132
A	PREPARING THE LASER SYSTEM FOR DAILY WORK	135
B	TRICS – TRAPPED ION CONTROL SOFTWARE	141
B.1	TrICS GUI	141
B.2	TrICS Daemon	143
B.3	Trixit	143
B.4	Version Control And Continuous Integration	144
BIBLIOGRAPHY		145

LIST OF FIGURES

Figure 2.1	Scheme of a linear Paul trap	8
Figure 2.2	Phase space diagram	10
Figure 2.3	Normal modes of a two ion crystal	14
Figure 2.4	Level scheme of $^{40}\text{Ca}^+$	16
Figure 2.5	Energy level diagram for a two-level system	17
Figure 3.1	Bloch sphere representation of a qubit	24
Figure 3.2	Possible qubit states in $^{40}\text{Ca}^+$	29
Figure 3.3	Phase space representation of two trapped ions	30
Figure 4.1	Trajectory of the COM state in phase space	32
Figure 4.2	Effect of counter-propagating pulses on a TLS	32
Figure 4.3	Timing of the simple GZC pulse scheme	36
Figure 4.4	Timing of the fast GZC pulse scheme	37
Figure 4.5	Fast GZC pulse scheme	38
Figure 4.6	Timing of the Duan pulse scheme	39
Figure 4.7	Duan pulse scheme	40
Figure 4.8	Timing of the FRAG pulse scheme	41
Figure 4.9	FRAG pulse scheme	41
Figure 4.10	Gate time as a function of repetition rate	42
Figure 4.11	Effect of counter-propagating pulses on a 3LS	43
Figure 5.1	Schematic setup of our laser system	50
Figure 5.2	Pulse train in time and frequency domain	51
Figure 5.3	Schematic overview of the frequency comb	52
Figure 5.4	Intensity autocorrelation of chirped pulses	54
Figure 5.5	Schematic overview of the cavity locks	55
Figure 5.6	Schematic overview of the AWG setup	58
Figure 5.7	Schematic overview of the delay generator setup	59
Figure 5.8	Schematic switching sequence of Pockels cells	60
Figure 5.9	Pulse train mode	61
Figure 5.10	Single pulses mode	63
Figure 5.11	Conversion efficiencies	65
Figure 5.12	Schematic overview of the 393 nm optical setup	66
Figure 5.13	Knife edge measurement	66
Figure 6.1	Spectrum of the high power EDFA output	70
Figure 6.2	Spectrum of the 786 nm light	70
Figure 6.3	Schematic FROG and XFROG setups	71
Figure 6.4	Wave vector diagrams of nonlinear processes	73

Figure 6.5	Part I, screenshots of FROG measurements	75
Figure 6.5	Part II, screenshots of FROG measurements	76
Figure 6.6	Michelson interferometer	78
Figure 6.7	Interferometric phase measurements	79
Figure 6.8	Measurement of pulse intensity areas	81
Figure 7.1	Schematic view of the Paul trap	84
Figure 7.2	Schematic view of optical access to the ion	85
Figure 7.3	Schematic setup of the ablation laser	86
Figure 7.4	Schematic setup of the photo ionization lasers	87
Figure 7.5	Schematic setup of the 397 nm laser	88
Figure 7.6	Schematic setup of the repumping lasers	88
Figure 7.7	Schematic setup of the 729 nm laser	90
Figure 7.8	Schematic overview of the control system	91
Figure 8.1	Simplified three-level scheme of $^{40}\text{Ca}^+$	96
Figure 8.2	Simulated chirped pulse	101
Figure 8.3	Simulation of 500 pulses	102
Figure 8.4	Beginning and end of experimental sequences	103
Figure 8.5	Sequence for coherent population trapping	105
Figure 8.6	Experimental observation of a dark resonance	106
Figure 8.7	Experimental sequence of coherent excitation	108
Figure 8.8	Data of coherent excitation, many pulses	109
Figure 8.9	Simulation of coherent excitation, many pulses	110
Figure 8.10	Data of coherent excitation, few pulses	112
Figure 8.11	Probability to excite the ion	114
Figure 8.12	Simulated probability to excite the ion	115
Figure 8.13	Sequence of a Ramsey contrast experiment	116
Figure 8.14	Data sets of a Ramsey experiment	117
Figure 8.15	Experimental data of the Ramsey contrast	119
Figure 8.16	Simulation of a Ramsey contrast experiment	120
Figure 9.1	Proposed scheme for switching beam paths	130
Figure 9.2	Proposed scheme to split and combine pulses	130
Figure A.1	Typical f_{CEO} beat signal	136
Figure A.2	Screenshot of the FiberLaser tool	137
Figure A.3	Cavity lock signals	138
Figure B.1	Schematic overview of the control software	142

LIST OF TABLES

Table 4.1	Comparison of fast gate schemes	43
Table 5.1	Overview of important light parameters within the laser system	56
Table 7.1	Overview of the employed laser wavelengths and their purposes	86
Table 8.1	Summary of fit parameters for the different experiments	121

LISTINGS

ACRONYMS

AOM	acousto-optic modulator
ARP	adiabatic rapid passage
AWG	arbitrary waveform generator
BBO	barium borate
CEO	carrier envelope offset
CNOT	controlled NOT
CW	continuous wave
DDS	direct digital synthesizer
DFG	difference-frequency generation
ECDL	external cavity diode laser

EDFA	erbium doped fiber amplifier
EMCCD	electron-multiplying charge-coupled device
EOM	electro-optic modulator
FPGA	field-programmable gate array
FRAG	fast robust antisymmetric gate
FROG	frequency-resolved optical gating
FWHM	full width at half maximum
GZC	García-Ripoll, Zoller, and Cirac
IQOQI	Institute for Quantum Optics and Quantum Information
OSA	optical spectrum analyzer
PBS	polarizing beam splitter
PCF	photonic-crystal fiber
PDH	Pound-Drever-Hall
PLL	phase-locked loop
PM	polarization maintaining
PMT	photomultiplier tube
PPKTP	periodically-poled potassium titanyl phosphate
PPLN	periodically-poled lithium niobate
RF	radio frequency
RTP	rubidium titanyl phosphate
SHG	second harmonic generation
SM	single-mode
SNR	signal-to-noise ratio
SOA	semiconductor optical amplifier
TA	tapered amplifier

TOD	third-order dispersion
TrICS	Trapped Ion Control Software
TTL	transistor-transistor logic
UHV	ultra-high vacuum
WLM	wavelength meter
XFROG	cross-correlation FROG

Part I

INTRODUCTION, THEORY AND
PREREQUISITES

INTRODUCTION

The development of computational tools started thousands of years ago. One of the earliest of such devices was the abacus, which is still in use today in some parts of the world. Since then, the development progressed through mechanical analog computers and much later also electronic analog computers until the realization of Alan Turing's ideas of a digital computer [1]. Initially, most digital computers were electromechanical such as Konrad Zuse's Z3 and filled large rooms with thousands of relays. But with the fast paced development of the vacuum tube, the transistor and later the integrated circuit, computers quickly became smaller and smaller. According to Moore's law [2], the number of transistors in modern microchips doubles about every two years, which in a few years would lead to transistors the size of a single atom. Before that point is reached, new problems will arise which will prevent such small structures to behave as usual: Quantum effects will have to be considered. It is unlikely though, that this will be the end of the development of computers, the effects of quantum mechanics are both boon and bane.

In the early 1980s, a device was proposed which uses quantum-mechanical effects to calculate the result of certain computations [3]. Such a device has two applications. On the one hand, its well-known and controllable quantum system can be used to simulate the behavior of a more complex system, which classical computers can not do efficiently. This *quantum simulator* [4, 5] allows one to examine quantum systems that are very difficult or even impossible to isolate and control in the lab, and make predictions of their characteristics. On the other hand, such a quantum system can be used for the implementation of quantum algorithms most of which were developed in the 1990s. A *quantum computer* running e. g. Shor's algorithm [6], would be able to factorize an integer of length N in a time that is polynomial in $\log(N)$. The fastest known classical factoring algorithm is almost exponentially slower. Other quantum algorithms include those by Deutsch and Jozsa [7], which is one of the first quantum algorithms that would be faster than any classical algorithm, and the database search algorithm by Grover [8]. Shor and – independently – Steane also proposed a protocol for quantum error correction [9, 10] which is essential for

fault-tolerant quantum computing. Soon after, DiVincenzo published a list of requirements for building a quantum computer [11]. In short these requirements are

1. A scalable quantum system with well-known degrees of freedom (“qubits”),
2. The ability to initialize the qubits,
3. The quantum system must be isolated from the environment such that decoherence can be controlled for,
4. A “universal” set of quantum logic gates, which includes a transformation which is able to entangle qubits,
5. A way to reliably read out the qubit state.

Research groups working with different quantum systems, such as superconducting qubits, trapped ions and others, are trying to implement these requirements.

Trapped ions in particular are a well-studied and promising system for the implementation of a scalable quantum computer [12–16]. Two-qubit entangling gate operations have been demonstrated [17–20] and combined with single-qubit gate operations to build an elementary quantum processor [21–23]. The entangling gate operations in these experiments have been carried out in an adiabatic regime in which they rely on coupling to spectroscopically-resolved motional sidebands of the qubit transition. The requirement to resolve sidebands introduces an intrinsic limit to the duration of a gate operation: it has to be longer than the period of motion of the ions in the trap (about 1 μ s). Overcoming this limitation would advance the development of a scalable quantum computer as it would allow one to increase the number of gate operations (computational steps) that can be completed within the coherence time of the ion-qubits.

In 2003, García-Ripoll, Zoller, and Cirac proposed a two-qubit entangling gate operation, which can be completed in less than one trap period using counter-propagating, ultrashort laser pulses to apply qubit state-dependent momentum kicks[24]. Instead of resolving a motional sideband of the ion crystal, this ultrafast phase gate operation excites many motional states at once and can complete orders of magnitude faster than previous entangling gates. The proposal has spawned research in both the theoretical [25–29] and experimental field of physics. Several groups are working on its realization [30,

31] but so far, only single-qubit gate operations [32, 33] and single-ion spin-motion entanglement [34] have been reported on time scales shorter than the ion oscillation period. The creation of two-qubit entanglement by a train of ultrafast laser pulses within a few microseconds has been demonstrated in the ground-states of a pair of Yb^+ ions [35]. Recently, Schäfer et al. reported a two-ion entangling gate faster than the motional period using amplitude-shaped laser pulses [36].

Contrary to the approach taken by the group of Christopher Monroe, who is using pulses to drive stimulated Raman transitions to produce a qubit state-dependent kick [30, 32–35], the project described in this thesis uses resonant laser pulses to realize the state-dependent momentum kicks.

One difficulty in applying the fast gate operation is in restoring the excited motional states to their initial state. This requires precise control over the arrival time of pulses at the ion crystal which can be achieved either by delaying single pulses with respect to others or by using a high pulse repetition rate. So far and to my best knowledge, the highest repetition rate reported in a laser for fast quantum logic is 300 MHz [37]. Though not yet done experimentally, it has been shown that the gate time of the fastest phase gate operation¹ a laser of this repetition rate could implement is on the order of 0.5 trap periods (500 ns) [28, 31]. A higher repetition rate could significantly reduce the minimum required gate time.

The goal of this thesis is to design, build and characterize a laser system with the help of which it is possible to implement an ultrafast two-qubit phase gate operation using resonant, counter-propagating laser pulses in $^{40}\text{Ca}^+$ ions. A high repetition rate of 5 GHz ensures that the gate time can be well below a single oscillation period of the ion crystal in the trap potential. The choice of ion species allows us to access the knowledge and tool kits available in the Quantum Optics & Spectroscopy research group at the University of Innsbruck.

This thesis is organized in three parts. Part I introduces the thesis's topic and summarizes previous work which the thesis is based on. After the introduction, the theoretical, fundamental properties of Paul traps, the $^{40}\text{Ca}^+$ ion and ion-light interaction are introduced in chapter 2. There, the Hamiltonians for describing the ions' harmonic motion in the trap potential, a two-level system and the ion-laser interaction are summarized. Chapter 3 then gives an overview of quantum information processing with a focus on utilizing trapped ions as qubits.

¹ of the FRAG type, see section 4.2.3

A number of fundamental single and two-qubit gates are introduced along with previous experimental efforts in their implementation. In chapter 4, the proposal for the realization of an ultrafast phase gate operation using a pulsed laser is introduced and previous theoretical work is summarized with a focus on the implementation in $^{40}\text{Ca}^+$.

Part II contains a description of the experimental apparatus and results acquired during the work on the thesis as well as an outlook: Based on the theoretical proposal, a laser system was designed and set up, which is described in chapter 5. The system comprises a high repetition rate, ultrafast pulsed laser which is derived from a stabilized optical frequency comb. Its light is amplified at 1572 nm and the wavelength is shifted via cascaded SHG to 393 nm, resonant to the $4S_{1/2} \leftrightarrow 4P_{3/2}$ transition in $^{40}\text{Ca}^+$. The characterization in chapter 6 shows that the pulses are chirped and that it is possible to pick arbitrary pulse sequences out of the 5 GHz pulse train. Chapter 7 describes the experimental apparatus used for trapping and manipulating $^{40}\text{Ca}^+$ ions as well as the hardware and software of the experimental control system. Next, chapter 8 first introduces models for simulating the ion-light interaction and then describes the thesis' experimental results. These show that the laser can coherently drive the $4S_{1/2} \leftrightarrow 4P_{3/2}$ transition in $^{40}\text{Ca}^+$ and that it can create approximate π -pulses on that transition with only a single optical pulse: a key-requisite to implementing a resonant, ultrafast, two-qubit phase gate operation.

Finally, part III completes the thesis with a summary of the thesis and an outlook into possible future experiments in chapter 9, and with appendix A, which details the process of preparing the laser system for a measurement.

Experimenting with an ion-based quantum computer requires restricting ion movement to a region where the ion(s) can be manipulated. Common ion traps use electric and/or magnetic fields to confine the ions to a small region where they can be cooled by e. g. laser radiation to even the motional ground state. In order to prevent the ions from undergoing collisions with other atoms and molecules, the traps are typically placed under ultra-high vacuum ([UHV](#)) ($< 10^{-9}$ mbar).

This chapter summarizes the effects of the trapping potential and of a laser field on singly charged (calcium) atoms. In [section 2.1](#) the Paul trap and its trapping potential is introduced along references [\[38, 39\]](#). Next, the ion motion is first quantized and then the treatment is generalized for a few-ion crystal. The $^{40}\text{Ca}^+$ ion is introduced in [section 2.2](#) and [section 2.3](#) summarizes the interaction of a laser-light field with the internal and external degrees of freedom of an ion.

2.1 PAUL TRAPS

A typical linear Paul trap consists of six electrodes: Two pairs of radial electrodes and one pair of axial electrodes. Each pair is typically held at the same electrical potential and the electrodes of each pair are on opposite sides of the trap as illustrated in [figure 2.1](#). The radial electrodes create a time-varying, two-dimensional quadrupole field that confines the ions in the radial direction. One pair of the radial electrodes is usually held at a DC potential that defines the electric ground of the trap. To the other pair, a radio frequency ([RF](#)) signal of amplitude V_0 and angular frequency Ω_{Trap} is applied. The axial electrode pair is held at a DC potential U_0 which creates a harmonic potential that confines the ions in the axial direction. A trapped ion would be located in the middle of the trap, separated by R from the radial electrodes and by Z from the axial ones.

The radial electrodes create a two-dimensional quadrupole field

$$V(x, y, t) = \frac{\kappa_r V_0}{2R^2} \cos(\Omega_{\text{Trap}} t) (x^2 - y^2), \quad (2.1)$$

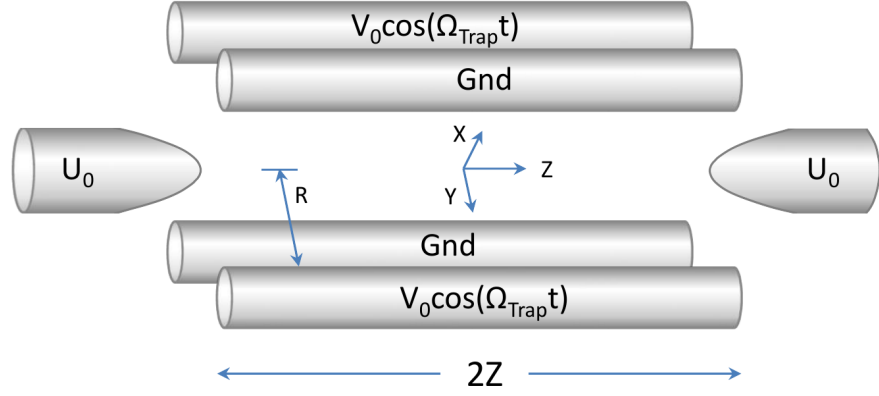


Figure 2.1: Scheme of a linear Paul trap. Figure source: [40]

where $\kappa_r \approx 1$ is a geometrical factor determined by the shape of the electrodes. The average motion of an ion of charge Q and mass M , on a time scale slow compared to $1/\Omega_{\text{Trap}}$, can be approximated by the motion in the pseudo-potential

$$\phi(x, y) = \frac{M\omega_r}{2Q}(x^2 + y^2), \quad (2.2)$$

in which the ion will oscillate at the radial oscillation frequency of

$$\omega_{x,y} \equiv \omega_r = \frac{\kappa_r Q V_0}{\sqrt{2} M R^2 \Omega_{\text{Trap}}} \quad (2.3)$$

in x and y direction.

The static potential created by the axial electrodes is given by

$$U(x, y, z) = \frac{\kappa_z U_0}{Z^2} \left(z^2 - \frac{1}{2}(x^2 + y^2) \right), \quad (2.4)$$

where $\kappa_z < 1$ is another geometrical factor determined by the shape of the electrodes. An ion will oscillate at the axial oscillation frequency of

$$\omega_z = \sqrt{\frac{\kappa_z Q U_0}{8 M Z^2}} \quad (2.5)$$

due to this harmonic potential.

2.1.1.1 Quantum harmonic oscillator and phase space

A newly trapped ion, which was created by laser ablating an atom from a target and ionizing it, usually comes along with kinetic and

potential energy on the order of 1 eV [41] ($\approx k_B 10^4$ K, with k_B the Boltzmann constant) and can thus be considered “hot”. In this regime the ion follows a classical trajectory through the trap volume. However, the utilization of nonclassical states and motional qubits requires that the ion is cooled to well below the quantum limit [39]

$$k_B T \ll \hbar \omega, \quad (2.6)$$

with k_B the Boltzmann constant and T the temperature of the ion. In this regime quantum effects start to matter, and the ion’s motion in the trapping potential has to be quantized [42, 43].

Classically, the motion of a particle of energy E and mass M in a harmonic potential $U(x) = \frac{1}{2}kx^2$ with force constant k must satisfy the classical equation of the conservation of energy,

$$\frac{p^2}{2M} + \frac{1}{2}M\omega^2 x^2 = E, \quad (2.7)$$

where p is the momentum and $\omega = \sqrt{\frac{k}{M}}$ the oscillation frequency.

Hence in quantum mechanics, the Hamiltonian describing the ion motion as a harmonic oscillator in the harmonic potential along the trap axis becomes

$$H_{\text{H.O.}} = \frac{\hat{\mathbf{p}}^2}{2M} + \frac{1}{2}M\omega_z^2 \hat{\mathbf{z}}^2, \quad (2.8)$$

where $\hat{\mathbf{z}}$ is the position operator and $\hat{\mathbf{p}} = -i\hbar \frac{\partial}{\partial x}$ the momentum operator. By introducing the ladder operators a and a^\dagger , given by

$$\begin{aligned} a &= \sqrt{\frac{M\omega_z}{2\hbar}} \left(\hat{\mathbf{z}} + \frac{i}{M\omega_z} \hat{\mathbf{p}} \right) \\ a^\dagger &= \sqrt{\frac{M\omega_z}{2\hbar}} \left(\hat{\mathbf{z}} - \frac{i}{M\omega_z} \hat{\mathbf{p}} \right), \end{aligned} \quad (2.9)$$

the Hamiltonian can be written as

$$H_{\text{H.O.}} = \hbar\omega_z \left(a^\dagger a + \frac{1}{2} \right). \quad (2.10)$$

Applying the ladder operators on an eigenstate $|n\rangle$ results in

$$a^\dagger |n\rangle = \sqrt{n+1} |n+1\rangle \quad (2.11)$$

$$a |n\rangle = \sqrt{n} |n-1\rangle \quad (2.12)$$

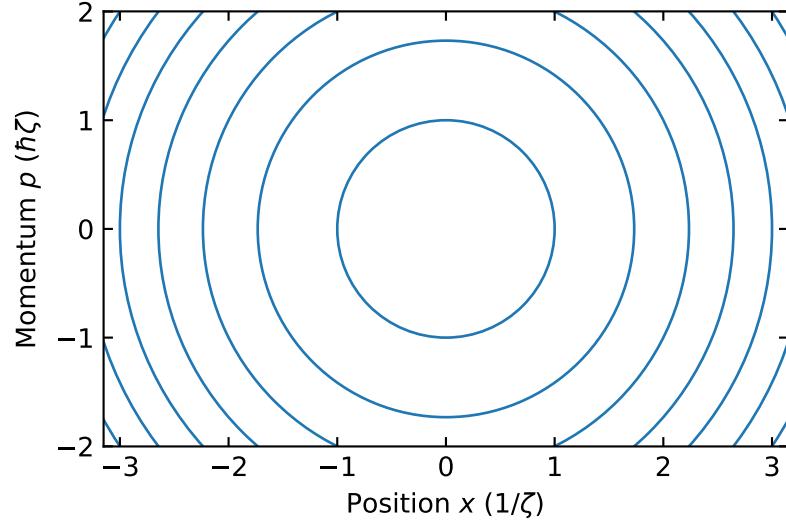


Figure 2.2: Phase space diagram of the lowest energy eigenstates $|n\rangle$, $n \leq 6$. Phase space is spanned by dimensionless parameters ζx and $p/\hbar\zeta$.

and the eigenvalues therefore are

$$E_n = \hbar\omega_z \left(n + \frac{1}{2} \right). \quad (2.13)$$

Fock states These energy eigenstates $|n\rangle$ are also called *Fock states* and a particle in a Fock state has a well-defined number of quanta, in this case phonons. Similar to the classical oscillator, such particle's motion in the harmonic potential is governed by the Schrödinger equation and the Hamiltonian in equation (2.8) but allowed energies are only the eigenvalues E_n . By introducing the dimensionless parameters position ζx and momentum $p/\hbar\zeta$, with $\zeta = \sqrt{M\omega/\hbar}$, this becomes

$$\left(\frac{p}{\hbar\zeta} \right)^2 + (\zeta x)^2 = 2 \left(n + \frac{1}{2} \right). \quad (2.14)$$

In phase space spanned by above dimensionless parameters these phase space trajectories take the form of concentric circles with radii $\sqrt{2(n + \frac{1}{2})}$, which are plotted in figure 2.2 for $n \leq 6$.

Quantum states such as the motional state of a particle in a harmonic potential can also be in superpositions of Fock states. The eigenstates $|\alpha\rangle$ of the annihilation operator a , $a|\alpha\rangle = \alpha|\alpha\rangle$, are states that are most similar to the classical motion of a particle in a harmonic potential.

They are called *coherent states* and in general α is a complex number. In the Fock basis, coherent states can be represented by

$$|\alpha\rangle = e^{-\frac{|\alpha|^2}{2}} \sum_{n=0}^{\infty} \frac{\alpha^n}{\sqrt{n!}} |n\rangle. \quad (2.15)$$

Their energy expectation value is

$$\langle\alpha|H_{\text{H.O.}}|\alpha\rangle = \hbar\omega_z \left(\langle\alpha|a^\dagger a|\alpha\rangle + \frac{1}{2} \right) = \hbar\omega_z \left(|\alpha|^2 + \frac{1}{2} \right), \quad (2.16)$$

which can take any value above $\frac{\hbar\omega_z}{2}$. Coherent states can be created by displacing the ground state $|0\rangle$ by α using the *displacement operator* $\hat{D}(\alpha) = \exp(\alpha a^\dagger - \alpha^* a)$,

$$\hat{D}(\alpha) |0\rangle = |\alpha\rangle. \quad (2.17)$$

In chapter 4 it will be shown that the effect of an ultrashort pulse on a two-ion crystal is that of applying displacement operators to the ion state.

2.1.2 Few ion crystals

Trapping more than one ion in a Paul trap complicates the ions' motion significantly because the ions will interact with each other due to the Coulomb repulsion. Why this is nonetheless desirable and even necessary will be made clear in chapter 3. This summary of the collective ion motion of an N ion crystal follows references [39, 44].

When the linear Paul trap contains more than one ion, the ions will align in a single row along the trap axis (the z axis) if the radial confinement is tight compared to the axial confinement $\omega_z \ll \omega_r$ and the ions' temperatures are cold. Under these conditions and with $z_n(t)$ the position of ion number n along the trap axis, the potential energy of the ion chain can be written as (assuming that $x_n = y_n = 0$) [44]

$$U = \sum_{n=1}^N \frac{1}{2} M \omega_z z_n(t)^2 + \sum_{\substack{n,m=1 \\ m \neq n}}^N \frac{Q^2}{8\pi\epsilon_0} \frac{1}{|z_n(t) - z_m(t)|}, \quad (2.18)$$

with ϵ_0 the permittivity of free space. Since we already assumed the ions are cold, we can write the position of the ions as the sum of the equilibrium position $z_n^{(0)}$ and a small displacement $q_n(t)$:

$$z_n(t) = z_n^{(0)} + q_n(t). \quad (2.19)$$

The $z_n^{(0)}$ are determined by the partial minimum of the potential energy

$$\left[\frac{\partial U}{\partial z_n} \right]_{z_n=z_n^{(0)}} = 0. \quad (2.20)$$

By defining a length scale z_s and the dimensionless equilibrium position u_n by

$$z_s = \sqrt[3]{\frac{Q^2}{4\pi\epsilon_0 M \omega_z^2}} \quad (2.21)$$

$$u_n = z_n^{(0)} / z_s, \quad (2.22)$$

equation (2.20) can be written as a set of coupled equations,

$$u_n = \sum_{m=1}^{n-1} \frac{1}{(u_n - u_m)^2} + \sum_{m=n+1}^N \frac{1}{(u_n - u_m)^2}. \quad (2.23)$$

These can only be solved analytically for $N = 2$ and $N = 3$, for higher values of N they have to be solved numerically. For $N = 2$, the u_n are given by

$$u_1 = -(1/2)^{2/3}, \quad u_2 = (1/2)^{2/3}, \quad (2.24)$$

higher values can be found in reference [44].

The q_n (the ions' displacement from their equilibrium positions along the axial direction) can be approximated using the Lagrangian

$$L = \frac{M}{2} \sum_{n=1}^N (\dot{q}_n)^2 - \frac{1}{2} \sum_{m,n=1}^N q_m q_n \left[\frac{\partial^2 U}{\partial x_m \partial x_n} \right]_{q_m=q_n=0} \quad (2.25)$$

$$= \frac{M}{2} \left[\sum_{n=1}^N (\dot{q}_n)^2 - \omega_z^2 \sum_{m,n=1}^N A_{mn} q_m q_n \right], \quad (2.26)$$

which neglects terms of $\mathcal{O}(q_n^3)$ and with

$$A_{mn} = \begin{cases} 1 + 2 \sum_{\substack{p=1 \\ p \neq n}}^N \frac{1}{|u_n - u_p|^3} & \text{if } m = n \\ \frac{-2}{|u_n - u_m|^3} & \text{if } m \neq n \end{cases} \quad (2.27)$$

The eigenvectors $\mathbf{b}_n^{(p)}$ and eigenvalues μ_p of A_{mn} are defined by

$$\sum_{m=1}^N A_{mn} \mathbf{b}_m^{(p)} = \mu_p \mathbf{b}_n^{(p)}, \quad (p = 1, \dots, N), \quad (2.28)$$

where $\mu_p \geq 0$, since the matrix A_{mn} is real, symmetric and non-negative definite. Assuming the eigenvectors are numbered in order of increasing eigenvalue and they are normalized so that

$$\sum_{p=1}^N \mathbf{b}_m^{(p)} \mathbf{b}_n^{(p)} = \delta_{mn}, \quad \sum_{n=1}^N \mathbf{b}_n^{(p)} \mathbf{b}_n^{(q)} = \delta_{pq}, \quad (2.29)$$

the eigenvectors and eigenvalues for $N = 2$ are given by

$$\begin{aligned} \mathbf{b}^{(1)} &= \frac{1}{\sqrt{2}} \begin{pmatrix} 1 \\ 1 \end{pmatrix}, \quad \mu_1 = 1, \\ \mathbf{b}^{(2)} &= \frac{1}{\sqrt{2}} \begin{pmatrix} -1 \\ 1 \end{pmatrix}, \quad \mu_2 = 3. \end{aligned} \quad (2.30)$$

For higher values of N these can again be found in reference [44].

From these results we can determine the normal modes of ion motion along the axial direction which are defined by

$$Q_p(t) = \sum_{n=1}^N \mathbf{b}_n^{(p)} q_n(t). \quad (2.31)$$

They can be used to rewrite the ion oscillation Lagrangian in equation (2.26):

$$L = \frac{M}{2} \sum_{p=1}^N \left[\dot{Q}_p^2 - \omega_p^2 Q_p^2 \right], \quad (2.32)$$

with ω_p the (angular) oscillation frequency of the p^{th} mode, which is given by

$$\omega_p = \sqrt{\mu_p} \omega_z. \quad (2.33)$$

The first mode $Q_1(t)$ corresponds to the *center-of-mass* mode where all ions oscillate together, without changing the inter-ion spacing, at frequency $\omega_1 = \omega_z$. The second mode $Q_2(t)$ corresponds to the *stretch* or *breathing* mode, where the ions oscillate with an amplitude proportional to their equilibrium distance to the trap center, at frequency $\omega_2 = \sqrt{3} \omega_z$. For $N = 2$ these modes are schematically plotted in figure 2.3.

With the canonical momentum conjugate P_p to Q_p , $P_p = M \dot{Q}_p$, the Hamiltonian can be written as

$$H = \frac{1}{2M} \sum_{p=1}^N P_p^2 + \frac{M}{2} \sum_{p=1}^N \omega_p^2 Q_p^2. \quad (2.34)$$

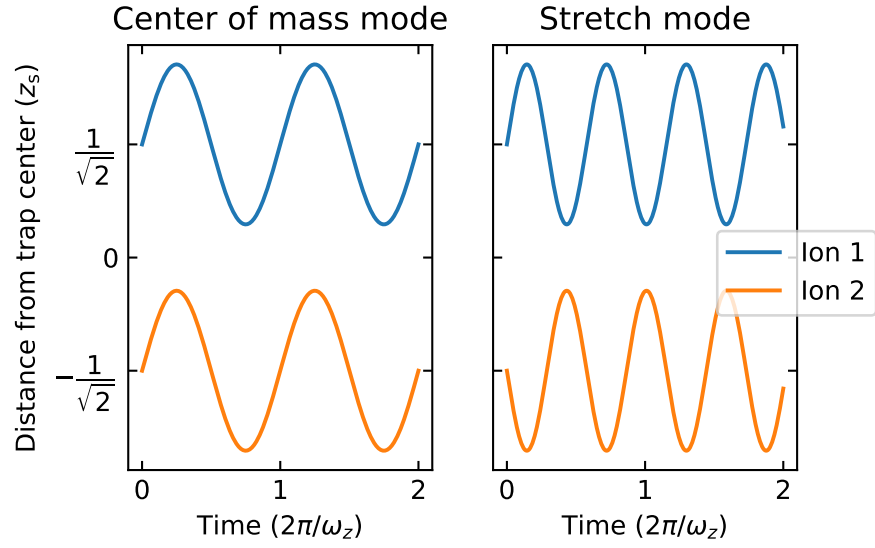


Figure 2.3: Schematic plot of the normal modes $Q_p(t)$ for an $N = 2$ ion crystal. The amplitude of the oscillation is greatly exaggerated to illustrate the differences between the modes. The abscissa is plotted in units of oscillation period $2\pi/\omega_z$, the ordinate in units of the length scale z_s . Note that the center of mass mode oscillates at the same frequency ω_z as a single ion in the same harmonic potential, while the stretch mode oscillates at $\sqrt{3}\omega_z$.

In order to quantize the ion motion, the following operators have to be introduced:

$$\hat{Q}_p = \sqrt{\frac{\hbar}{2M\omega_p}}(a_p^\dagger + a_p), \quad (2.35)$$

$$\hat{P}_p = i\sqrt{\frac{\hbar M\omega_p}{2}}(a_p^\dagger - a_p), \quad (2.36)$$

where a_p , a_p^\dagger are the ladder operators of the p^{th} mode and obey $[a_p, a_q^\dagger] = \delta_{pq}$. This allows writing the interaction picture operator for the displacement of the n^{th} ion as

$$\hat{q}_n(t) = \sum_{p=1}^N \mathbf{b}_n^{(p)} \hat{Q}_p(t). \quad (2.37)$$

2.2 THE $^{40}\text{Ca}^+$ ION

For the experiments of this thesis a singly charged isotope of calcium was used: $^{40}\text{Ca}^+$. Neutral calcium-40 atoms can be ionized to $^{40}\text{Ca}^+$ in an isotope-selective two-step process [45]. With one of its two valence electrons removed, $^{40}\text{Ca}^+$ and other ions of alkaline earth metals have an energy level structure similar to neutral atoms of alkali metals, particularly to the hydrogen atom [46, 47].

The three lowest orbitals that the valence electron of $^{40}\text{Ca}^+$ can populate are the 4S, the 3D and the 4P orbitals. As shown in figure 2.4 these split into the levels $4S_{1/2}$, $3D_{3/2}$, $3D_{5/2}$, $4P_{1/2}$ and $4P_{3/2}$, which in turn split into Zeeman sublevels with the magnetic quantum numbers m_J when exposed to a magnetic field.

Approximating the ion levels by a two-level system is justified if the frequencies of electromagnetic fields coupling the levels are close to only one of the transition frequencies of any two internal levels and if the Rabi frequencies are always much smaller than the detuning of the fields relative to all the other transitions. If the two levels $|g\rangle$ and $|e\rangle$ have the respective energy of $\hbar\omega_g$ and $\hbar\omega_e$, the Hamiltonian describing the two-level system can be written as [53]:

$$H_A = \hbar\omega_g |g\rangle\langle g| + \hbar\omega_e |e\rangle\langle e|. \quad (2.38)$$

Setting the zero energy level to halfway between the two levels and using the energy splitting $\hbar\omega_A = \hbar(\omega_e - \omega_g)$, the Hamiltonian becomes

$$H_A = \hbar \frac{\omega_A}{2} \sigma_z, \quad (2.39)$$

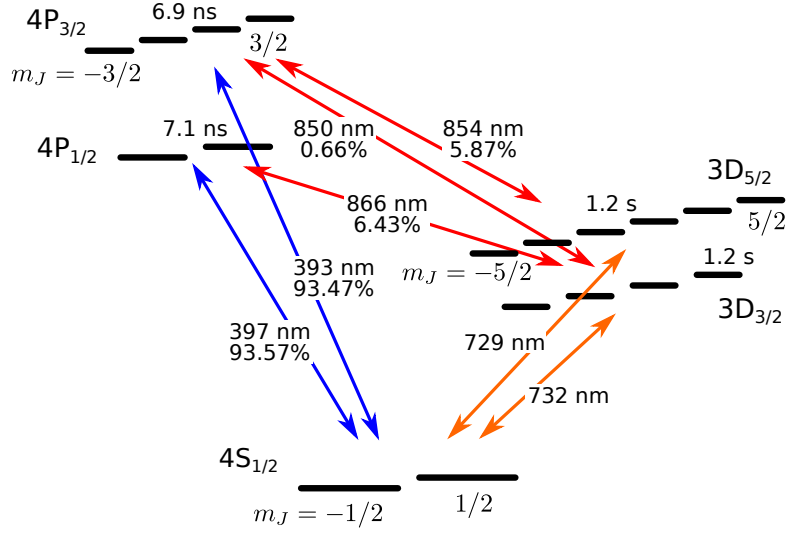


Figure 2.4: Level scheme of $^{40}\text{Ca}^+$ including all Zeeman sublevels of the three lowest orbitals. Possible transitions are shown with their wavelengths and branching ratios [48, 49], excited electronic states with their lifetimes [50–52]. This figure was adapted from [47].

where $\sigma_z = |e\rangle\langle e| - |g\rangle\langle g|$ is the Pauli z matrix.

2.3 ATOM-LIGHT INTERACTION

Given a (laser) light field with the electric field

$$E(t) = \frac{1}{2}E_0 \exp(i(\omega_L t - \phi_L)) + \text{c.c.},$$

amplitude E_0 , frequency ω_L and phase ϕ_L , that couples the states of the two-level system seen in figure 2.5, the interaction is described by the Hamiltonian [53, 55]

$$H_L = \hbar \frac{\Omega}{2} (|g\rangle\langle e| + |e\rangle\langle g|) \cdot [\exp(i(k\hat{z} - \omega_L t + \phi_L)) + \text{c.c.}], \quad (2.40)$$

with $\Omega \propto E_0$ the Rabi frequency and k the wave vector of the light field. Using the Pauli matrices and $|e\rangle\langle g| = \sigma_+ = \frac{1}{2}(\sigma_x + i\sigma_y)$, $|g\rangle\langle e| = \sigma_- = \frac{1}{2}(\sigma_x - i\sigma_y)$ to express the Hamiltonian, it can be written as

$$H_L = \hbar \frac{\Omega}{2} (\sigma_+ + \sigma_-) \cdot [\exp(i(k\hat{z} - \omega_L t + \phi_L)) + \text{c.c.}]. \quad (2.41)$$

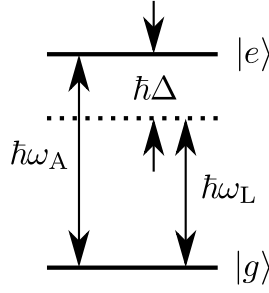


Figure 2.5: Energy level diagram for a two-level system with energy splitting $\hbar\omega_A$ acting with a near resonant classical light field of frequency ω_L . The detuning of the light field frequency with respect to the system's transition frequency is $\Delta = \omega_L - \omega_A$. Figure adopted from [54].

Drawing together the results of the previous sections – namely equations (2.10), (2.39) and (2.41) – the total Hamiltonian of the system is

$$H = H_{\text{H.O.}} + H_A + H_L. \quad (2.42)$$

The dynamics can be simplified by first transforming H_L into the interaction picture with respect to H_A . Using $U_A = \exp(-i/\hbar H_A t)$, the interaction Hamiltonian is

$$H_{\text{int}} = U_A^\dagger H_L U_A. \quad (2.43)$$

After applying the rotating wave approximation and simplifying the expression (for details see reference [56]) the Hamiltonian becomes

$$H_{\text{int}} = \hbar \frac{\Omega}{2} [\sigma_+ \exp(i(k\hat{z} - \Delta t + \phi_L)) + \sigma_- \exp(-i(k\hat{z} - \Delta t + \phi_L))], \quad (2.44)$$

with $\Delta = \omega_L - \omega_A$ the laser detuning from the atomic transition frequency. If only a single ion is considered, \hat{z} can be replaced by the single normal mode operator \hat{Q}_1 from equation (2.35),

$$H_{\text{int}} = \hbar \frac{\Omega}{2} \left[\sigma_+ \exp\left(i(\eta(a + a^\dagger) - \Delta t + \phi_L)\right) + \sigma_- \exp\left(-i(\eta(a + a^\dagger) - \Delta t + \phi_L)\right) \right], \quad (2.45)$$

with η the Lamb-Dicke parameter, given by

$$\eta = k\sqrt{\frac{\hbar}{2M\omega_z}}. \quad (2.46)$$

If the ion trapped in the harmonic potential is occupying motional states of sufficiently small phonon number n such that

$$\eta^2(2n+1) \ll 1, \quad (2.47)$$

Lamb Dicke regime the exponent in equation (2.45) can be expanded to the first order of η . This regime is called the *Lamb Dicke regime* and in the interaction picture with respect to $H_{\text{H.O.}}$, the Hamiltonian can be written

$$\begin{aligned} H_{\text{LD}}(t) = & \hbar \frac{\Omega}{2} \sigma_+ \left(1 + i\eta (ae^{(-i\omega_z t)} + a^\dagger e^{(i\omega_z t)}) \right) \\ & \times \exp(i(\phi_L - \Delta t)) \\ & + \text{H.c.} \end{aligned} \quad (2.48)$$

This contains three terms and under a second application of the rotating wave approximation each of the terms becomes resonant (i. e. time independent) at a different detuning Δ . The first term is resonant for $\Delta = 0$ and is called the *carrier resonance*. It takes the form

$$H_{\text{car}} = \hbar \frac{\Omega}{2} (\sigma_+ \exp(i\phi_L) + \sigma_- \exp(-i\phi_L)) \quad (2.49)$$

and is responsible for $|n, g\rangle \leftrightarrow |n, e\rangle$ transitions that leave the motional state unchanged. The term that is resonant for $\Delta = -\omega_z$ is called the *(first) red sideband* and is responsible for $|n, g\rangle \leftrightarrow |n-1, e\rangle$ transitions that entangle the motional state with the internal state of the ion. It can be written

$$H_{\text{rsb}} = \hbar \frac{\Omega}{2} \eta \left(a\sigma_+ \exp(i\phi_L) + a^\dagger \sigma_- \exp(-i\phi_L) \right). \quad (2.50)$$

Finally, the third term is resonant for $\Delta = +\omega_z$ and is called the *(first) blue sideband*. It is responsible for $|n, g\rangle \leftrightarrow |n+1, e\rangle$ transitions and takes the form

$$H_{\text{bsb}} = \hbar \frac{\Omega}{2} \eta \left(a^\dagger \sigma_+ \exp(i\phi_L) + a\sigma_- \exp(-i\phi_L) \right). \quad (2.51)$$

Unlike the idealized, single-frequency laser, the light of a pulsed laser has a time-varying electric field $E(t)$ and therefore a finite spectral width γ . Hence, the Rabi frequency $\Omega(t) = \mu E(t)/\hbar$, where μ is

the dipole moment, also becomes time-dependent. If the pulse is sufficiently weak such that its maximum Rabi frequency is small with respect to the trap frequency, $\Omega \ll \omega_z$, the previous assumptions are still valid and the atom-light interaction can be described as above. However, if the pulses are strong such that $\Omega \gg \omega_z$, this is not the case anymore. In this so-called *strong-excitation regime* [57], the second rotating wave approximation made above for calculating the terms in equations (2.49), (2.50) and (2.51) is no longer valid.

2.4 ELECTRIC FIELD OF A LASER PULSE

Modern pulsed lasers emit pulses with a pulse length τ on the order of nanoseconds and shorter. This is much shorter than the ion's motional period, $\tau \ll 2\pi/\omega_z$, and the ion's position can be considered constant on the length scale of the laser light's wavelength during the duration of such pulse. Therefore, the motional parts of the Hamiltonian in equation (2.44) can also be considered constant on that timescale and can be regarded as part of a global phase, and the Hamiltonian can be rewritten as

$$H_{\text{int}}(t) = \hbar \frac{\Omega(t)}{2} \sigma_+ \exp(i(\phi_L - \Delta t)) + \text{H.c.} \quad (2.52)$$

$$= c(t) \sigma_+ + \text{H.c.} \quad , \quad (2.53)$$

with the complex, time-dependent coefficient

$$c(t) = \hbar \frac{\Omega(t)}{2} e^{i\phi(t)}. \quad (2.54)$$

The coefficient's phase $\phi(t)$ depends on the detuning between the atomic transition and the laser field, and for a pulsed laser field also on the variation of the instantaneous frequency $\omega \propto \frac{d}{dt}\phi(t)$ during the pulse, which is also known as *chirp* [58]. In this thesis, it is assumed the frequency changes linearly with time, $\omega \propto t$, which is called a linear chirp, and requires $\phi(t) \propto t^2$. To describe such a pulsed laser field, $c(t)$ can be defined either temporally in the time domain or spectrally in the frequency domain (also compare with figure 5.2 on page 51).

2.4.1 Temporally defined pulses

One way to define the time-dependent coefficient $c(t)$ is by assuming e.g. a Gaussian shape for the electric field $E(t)$ of a single pulse, following references [58, 59], to get

$$E(t) = E_0 \exp\left(-\frac{t^2}{2\tau^2} + i\omega_L t - i\phi(t)\right), \quad (2.55)$$

with E_0 the peak amplitude, $\tau\sqrt{\ln 16}$ the full width at half maximum (FWHM) pulse length¹, ω_L the center frequency and $\phi(t)$ the temporal phase. Assuming a linear chirp, the phase can be written

$$\phi(t) = \alpha \frac{t^2}{2}, \quad (2.56)$$

with α the linear temporal chirp. The FWHM bandwidth of such defined pulse is $\gamma\sqrt{\ln 16}$ with

$$\gamma^2 = \frac{1}{\tau^2}(1 + \alpha^2\tau^4). \quad (2.57)$$

An N -pulse pulse train can then be described by the sum over N pulses separated by τ_{pulse} which results in the coefficient

$$c(t) = \sum_n^N \left[\hbar \frac{\Omega_0}{2} \exp\left(-\frac{(t - n\tau_{\text{pulse}})^2}{2\tau^2}\right) \times \exp\left(i(\omega_L - \omega_A)(t - n\tau_{\text{pulse}}) - i\alpha \frac{(t - n\tau_{\text{pulse}})^2}{2} + i\Delta \frac{n}{f_{\text{rep}}}\right) \right], \quad (2.58)$$

with $\Omega_0 = \mu E_0$.

2.4.2 Spectrally defined pulses

Alternatively, $c(t)$ can be defined by taking the sum over the electrical fields of the spectral modes of the laser light. The spectrum of a long train of pulses consists of field modes which are separated by the

¹ Scaling the bandwidth and pulse length with the numerical factor $\sqrt{\ln(16)}$ results in $\tau \cdot \gamma = 1$ for an unchirped ($\alpha' = 0$) pulse. Using instead the FWHM values and converting γ from angular frequency to ordinary frequency to calculate the time-bandwidth product gives $\tau\sqrt{\ln(16)} \cdot (\gamma\sqrt{\ln(16)}/2\pi) = \ln(16)/2\pi \approx 0.44$ which is the lower limit of the time-bandwidth product for Gaussian shaped pulses.

repetition rate f_{rep} from each other and offset by the carrier envelope offset (CEO) frequency f_{CEO} . The frequency f_n of each mode can be calculated according to

$$f_n = f_{\text{CEO}} + n \cdot f_{\text{rep}}, \quad (2.59)$$

for more details see section 5.1. If one mode with (angular) frequency ω_0 is detuned by $\Delta_0 = \omega_0 - \omega_A$ from the atomic transition frequency ω_A , all the other modes are then detuned by

$$\Delta_m = \Delta + m \cdot 2\pi f_{\text{rep}}. \quad (2.60)$$

Assuming the spectral envelope of the modes has a Gaussian shape and a FWHM bandwidth of $\gamma\sqrt{\ln 16}$, every mode can be assigned an electric field strength E'_m and corresponding Rabi frequency $\Omega'_m = \mu E'_m / \hbar$ according to their location within the spectral envelope:

$$\Omega'_m = \Omega'_0 \exp\left(-\frac{(\Delta_m - (\omega_L - \omega_A))^2}{2\gamma^2}\right), \quad (2.61)$$

with Ω'_0 the peak Rabi frequency. This can be put together to result in the time-dependent coefficient

$$c(t) = \sum_m \hbar \frac{\Omega'_m}{2} \exp(i\Delta_m \cdot t). \quad (2.62)$$

A linear spectral chirp α' , which is related to α by the equations

$$\alpha' = \alpha \frac{\tau^4}{1 + \alpha^2 \tau^4} \quad \text{and} \quad (2.63)$$

$$\alpha = \alpha' \frac{\gamma^4}{1 + \alpha'^2 \gamma^4}, \quad (2.64)$$

can be added to the light field to yield [58, 59]

$$c(t) = \sum_m \hbar \frac{\Omega'_m}{2} \exp\left(i\Delta_m \cdot t + i\alpha' \frac{\Delta_m^2}{2}\right). \quad (2.65)$$

The FWHM pulse length of such defined pulse is $\tau\sqrt{\ln 16}$ with

$$\tau^2 = \frac{1}{\gamma^2} (1 + \alpha'^2 \gamma^4), \quad (2.66)$$

which directly shows that τ increases when a pulse is chirped. In order to conserve pulse energy $P_0 = E_0^2 \tau$, the Rabi frequency in equation (2.58) has to be scaled with the chirp as well,

$$\Omega_0 = \frac{\Omega_0^{\alpha'=0}}{\sqrt[4]{1 + \alpha'^2 \gamma^4}} = \frac{\Omega_0^{\alpha'=0}}{\sqrt[4]{1 + \alpha^2 \tau^4}}. \quad (2.67)$$

QUANTUM INFORMATION PROCESSING WITH TRAPPED IONS

Quantum mechanics is one of those fields of physics that has gained a lot of attention among the general public and it has indeed revolutionized the way we think about physics and how to interpret theoretical predictions and experimental results. In the early 1980s scientists began to realize that the effects of quantum mechanics could be applied to solving problems a classical computer can not solve efficiently, such as using a well-controlled quantum system to simulate another quantum system, over which the experimenter has little or no control [4]. This and the first proposals to use quantum systems as a basis for a novel quantum computer [3, 60] initiated a strong research effort in this domain [12]. The promise of unfathomable speed-up of certain classes of calculations has further spurred the development and realization of systems usable for quantum computations [16, 22, 53]. Apparently, quantum mechanics has lived up to the hype with useful quantum computers seemingly right around the corner.

This chapter summarizes the basic building blocks of a quantum computer along reference [61], focusing on the implementation of trapped $^{40}\text{Ca}^+$ ions as qubits.

3.1 QUANTUM INFORMATION, GENERAL

In classical computer science, the *bit* is the fundamental unit of information. It can exist in either one of two states, usually called 0 and 1. Any physical system that can exist in discernible states can in principle be used to implement one or more bits, in practice a bit is encoded e.g. in well-defined charge levels of a capacitance or the direction of a magnetic field. In contrast, quantum information correspondingly uses a quantum system that can coexist in two states, namely $|0\rangle$ and $|1\rangle$. Such “quantum bit” is called a *qubit* [61]. What distinguishes a qubit from a classical bit is that the qubit can be in

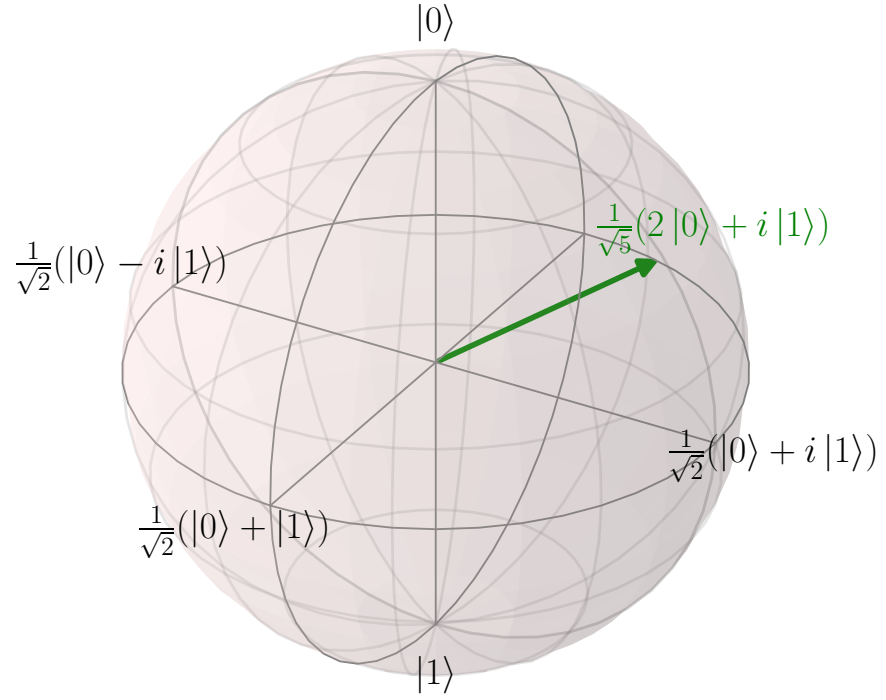


Figure 3.1: Bloch sphere representation of a qubit. The green arrow is a Bloch vector $\vec{r} = (0, 0.8, 0.6)^T$ representing the state $|\psi\rangle = \frac{1}{\sqrt{5}}(2|0\rangle + i|1\rangle) = \cos\left(\frac{\theta}{2}\right)|0\rangle + e^{i\phi}\sin\left(\frac{\theta}{2}\right)|1\rangle$, with $\theta \approx 0.3\pi$ and $\phi = \pi/2$.

a linear superposition of both states. A single, isolated qubit can be represented by the vector $|\psi\rangle$ such that

$$|\psi\rangle = \alpha |0\rangle + \beta |1\rangle = \begin{pmatrix} \alpha \\ \beta \end{pmatrix}, \quad \alpha, \beta \in \mathbb{C}, \quad |\alpha|^2 + |\beta|^2 = 1. \quad (3.1)$$

This can be rewritten as

$$|\psi\rangle = \cos\left(\frac{\theta}{2}\right) |0\rangle + e^{i\phi} \sin\left(\frac{\theta}{2}\right) |1\rangle, \quad (3.2)$$

with the real numbers θ and ϕ . They define a point on a unit sphere, allowing one to conveniently visualize any such quantum state $|\psi\rangle$ as a point on the surface of the *Bloch sphere* as shown in figure 3.1. Such a system whose state is known exactly is called a *pure state*.

Another way to represent a quantum system is to describe it by the *density matrix* operator ρ . If a system can only be in the states $|\psi_i\rangle$ and the corresponding state probabilities p_i are known, the system can be represented by

$$\rho = \sum_i p_i |\psi_i\rangle\langle\psi_i|. \quad (3.3)$$

A system with one $p_i = 1$ satisfies $\text{tr}(\rho^2) = 1$ and hence is still a pure state. A general state of a quantum system with all $p_i < 1$ and whose state therefore can not be known exactly is called a *mixed state* and $\text{tr}(\rho^2) < 1$ ¹. Alternatively, both pure and mixed quantum states can be described by a real, three-dimensional vector \vec{r} using the Pauli matrices,

$$\begin{aligned} \sigma_0 \equiv I &= \begin{pmatrix} 1 & 0 \\ 0 & 1 \end{pmatrix} & \sigma_1 \equiv \sigma_x &= \begin{pmatrix} 0 & 1 \\ 1 & 0 \end{pmatrix} \\ \sigma_2 \equiv \sigma_y &= \begin{pmatrix} 0 & -i \\ i & 0 \end{pmatrix} & \sigma_3 \equiv \sigma_z &= \begin{pmatrix} 1 & 0 \\ 0 & -1 \end{pmatrix} \end{aligned} \quad (3.4)$$

and

$$\rho = \frac{I + \vec{r} \cdot \vec{\sigma}}{2}, \quad \vec{\sigma} = \begin{pmatrix} \sigma_x \\ \sigma_y \\ \sigma_z \end{pmatrix}, \quad (3.5)$$

¹ This statement holds for a system of arbitrary size, not just for a single qubit.

with $|\vec{r}| \leq 1$. The vector \vec{r} is called the *Bloch vector* and can point anywhere on the surface of the Bloch sphere (describing a pure state) or inside the Bloch sphere (mixed state).

Not only are density operators able to describe both pure and mixed states, they also allow one to easily calculate the expectation value for any observable A using

$$\langle A \rangle = \text{tr}(A\rho). \quad (3.6)$$

In order to describe more than one qubit, one can still either use a density matrix or for pure states also a state vector. The state vector for a general two-qubit state is

$$|\psi\rangle = \alpha_{00}|00\rangle + \alpha_{01}|01\rangle + \alpha_{10}|10\rangle + \alpha_{11}|11\rangle = \begin{pmatrix} \alpha_{00} \\ \alpha_{01} \\ \alpha_{10} \\ \alpha_{11} \end{pmatrix}, \quad (3.7)$$

where the α_{ij} again have to be normalized, such that $\sum_{ij} |\alpha_{ij}|^2 = 1$ and $|ij\rangle$ means that the first qubit is in state i and the second in state j . While certain states can be described by the tensor product of two individual qubits, e. g.

$$\begin{aligned} |\psi\rangle &= |\psi_1\rangle \otimes |\psi_2\rangle \\ &= (\alpha_1|0\rangle + \beta_1|1\rangle) \otimes (\alpha_2|0\rangle + \beta_2|1\rangle) \\ &= \alpha_1\alpha_2|00\rangle + \alpha_1\beta_2|01\rangle + \beta_1\alpha_2|10\rangle + \beta_1\beta_2|11\rangle \end{aligned} \quad (3.8)$$

other states can not be separated into individual states, that is, they can not be written as a product of those states, e. g.

$$|\psi\rangle = \frac{|00\rangle + |11\rangle}{\sqrt{2}}. \quad (3.9)$$

entangled states

These states are called *entangled states*, and they can be considered a physical resource of quantum mechanics and quantum information that has no classical equivalent [61]. How entangled states can be created will be explained in the next section.

3.2 QUANTUM COMPUTATION

A classical computer uses the bits it has stored as input to its logic gates. These can manipulate the input bits and return output bits according to the gate operation's truth table. The NOT gate for example,

takes one input bit and outputs the opposite. Analogous to the classical computer a *quantum computer* uses elementary qubit operations to manipulate its qubits. These *quantum gate operations* can be represented by unitary matrices \mathcal{U} , that act on the qubits' state vectors:

$$|\psi_{\text{output}}\rangle = \mathcal{U} |\psi_{\text{input}}\rangle \quad (3.10)$$

Some of the most important single qubit operations are the Pauli $\{X, Y, Z\}$ -gates, the Hadamard gate H and the phase gate S , listed below are their quantum circuit symbols and their unitaries:

$$\begin{array}{ll} \text{---} \boxed{X} \text{---} & X = \sigma_x \equiv \begin{pmatrix} 0 & 1 \\ 1 & 0 \end{pmatrix} \\ \text{---} \boxed{Y} \text{---} & Y = \sigma_y \equiv \begin{pmatrix} 0 & -i \\ i & 0 \end{pmatrix} \\ \text{---} \boxed{Z} \text{---} & Z = \sigma_z \equiv \begin{pmatrix} 1 & 0 \\ 0 & -1 \end{pmatrix} \\ \text{---} \boxed{H} \text{---} & H = \frac{1}{\sqrt{2}} \begin{pmatrix} 1 & 1 \\ 1 & -1 \end{pmatrix} \\ \text{---} \boxed{S} \text{---} & S = \begin{pmatrix} 1 & 0 \\ 0 & i \end{pmatrix} \end{array}$$

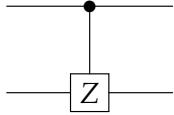
Qubit operations can also act on more than one qubit, an important class of these are the controlled qubit operations. In general, they apply a unitary operator to the target qubit(s) only, if the control qubit(s) are in state $|1\rangle$. For one target and control qubit each, this is represented by

$$\begin{array}{c} \text{---} \bullet \text{---} \\ | \\ \text{---} \boxed{\mathcal{U}} \text{---} \end{array} \quad \mathcal{C}_{\mathcal{U}} = \begin{pmatrix} 1 & 0 & 0 & 0 \\ 0 & 1 & 0 & 0 \\ 0 & 0 & & \mathcal{U} \\ 0 & 0 & & \end{pmatrix}. \quad (3.11)$$

Two important two-qubit operations are the controlled NOT (**CNOT**) operation (constructed from the Pauli X-gate),

$$\begin{array}{c} \text{---} \bullet \text{---} \\ | \\ \text{---} \oplus \text{---} \end{array} \quad \mathcal{C}_X = \begin{pmatrix} 1 & 0 & 0 & 0 \\ 0 & 1 & 0 & 0 \\ 0 & 0 & 0 & 1 \\ 0 & 0 & 1 & 0 \end{pmatrix} \quad (3.12)$$

and the controlled-Z gate, also called a π -phase gate:

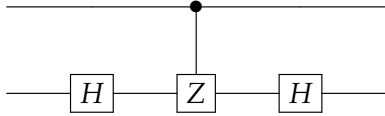


$$C_Z = \begin{pmatrix} 1 & 0 & 0 & 0 \\ 0 & 1 & 0 & 0 \\ 0 & 0 & 1 & 0 \\ 0 & 0 & 0 & -1 \end{pmatrix} \quad (3.13)$$

A significant realization is that all quantum gates can be constructed from other quantum gates. For example, any single qubit operation \mathcal{U} can be written as

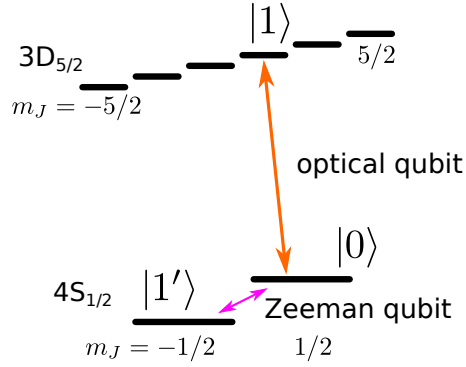
$$\mathcal{U} = e^{i\alpha} R_z(\beta) R_y(\gamma) R_z(\delta), \quad (3.14)$$

with α, β, γ and δ real numbers, and the rotation operators about the \hat{y} (\hat{z}) axis $R_y(\theta) = e^{-i\theta Y/2}$ ($R_z(\theta) = e^{-i\theta Z/2}$). Similarly, the CNOT gate can be constructed from the controlled-Z gate and two Hadamard gates:



$$\begin{pmatrix} H & 0 & 0 \\ 0 & 0 & H \\ 0 & 0 & 0 \end{pmatrix} \begin{pmatrix} 1 & 0 & 0 & 0 \\ 0 & 1 & 0 & 0 \\ 0 & 0 & 1 & 0 \\ 0 & 0 & 0 & -1 \end{pmatrix} \begin{pmatrix} H & 0 & 0 \\ 0 & 0 & H \\ 0 & 0 & 0 \end{pmatrix} = \begin{pmatrix} 1 & 0 & 0 & 0 \\ 0 & 1 & 0 & 0 \\ 0 & 0 & 0 & 1 \\ 0 & 0 & 1 & 0 \end{pmatrix} \quad (3.15)$$

This is important, because in a physical realization of a quantum computer some quantum operations can be implemented easier than others [39], while some can not be implemented (directly) at all. Since a quantum computer has to be able to carry out arbitrary unitary operations, it must at least have access to a set of quantum gates that allow any other quantum operation to be at least approximated with arbitrary precision. Every such *universal set of quantum gates* must contain both single qubit and multi qubit operations [62]. More precisely, it must contain an *entangling gate*, i. e. a gate that is able to

Figure 3.2: Possible qubit states in $^{40}\text{Ca}^+$.

create entanglement between the input qubits. Almost any controlled qubit operation is an entangling gate, including but not limited to the [CNOT](#), controlled-Z and the controlled- \mathcal{U} operations, with \mathcal{U} any of the already introduced single qubit operations.

3.3 QUANTUM COMPUTATION WITH TRAPPED IONS

In $^{40}\text{Ca}^+$, a qubit can be encoded either between two optically separated states of the $4S_{1/2}$ and $3D_{5/2}$ manifolds – e. g. $|4S_{1/2}, m_J = 1/2\rangle$ and $|3D_{5/2}, m_J = 1/2\rangle$ – or between the two Zeeman substates of the $4S_{1/2}$ ground state – i. e. $|4S_{1/2}, m_J = 1/2\rangle$ and $|4S_{1/2}, m_J = -1/2\rangle$ – as seen in figure 3.2. This thesis always uses the former way to encode a qubit.

In a string of two or more trapped ions, another qubit can be encoded in the collective motion of the ions [39]. This additional qubit can be used as a “bus” that mediates interactions between the individual ion qubits. Coupling the ion qubits via their collective motion has led to the realization of both the [CNOT](#) gate [17] and the π -phase gate [18] in the form of the unitary

$$\begin{pmatrix} 1 & 0 & 0 & 0 \\ 0 & i & 0 & 0 \\ 0 & 0 & i & 0 \\ 0 & 0 & 0 & 1 \end{pmatrix}, \quad (3.16)$$

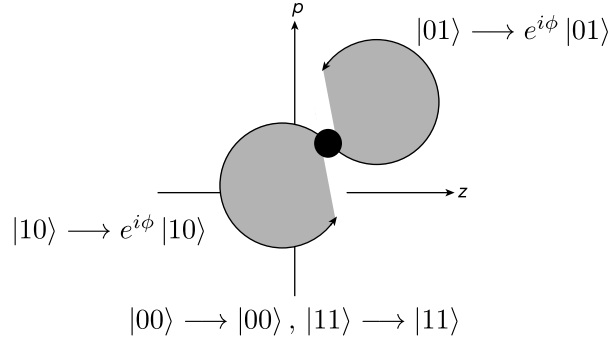
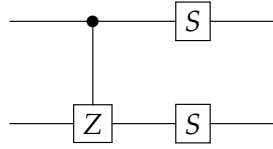


Figure 3.3: Phase space representation of the stretch-mode amplitude of two trapped ions. Image adapted from [18, figure 1].

which can be constructed from the (two qubit) π -phase gate and the (single qubit) phase gate S , applying it once to each qubit:



The π -phase gate was implemented by applying a coherent, state-dependent force to a pair of beryllium ion-qubits. The force acts on the stretch-mode of motion and displaces the states $|01\rangle$ and $|10\rangle$ along a circular path in phase space as shown in figure 3.3. Once the path is closed, the acquired geometric phase $\phi = A/\hbar$ is equal to the phase space area A enclosed by the trajectory. The π -phase gate requires $\phi = \pi/2$ which can be achieved by tuning the intensity of the laser beams that drive the state-dependent force.

Every quantum gate scheme that uses the additional bus qubit has to spectroscopically resolve the motional sidebands (see equations (2.50) and (2.51)). This requirement limits the intensity of the exciting laser and therefore the gate time to more than the motional period of the ions in the trap [24]. Hence, in order to minimize the effects of decoherence on the gate and to be able to execute more computational steps within the coherence time of the qubit it is desirable to reduce the gate time to below this limit.

Fast entangling phase gates have been proposed by García-Ripoll, Zoller, and Cirac (GZC) in 2003 [24, 26]. Unlike essentially all other entangling gate schemes suggested until then, the GZC scheme's duration is not limited by the trap period, and can be orders of magnitude faster than previous schemes. The original proposal [24] has spawned both theoretical efforts to improve on and analyze the gate scheme [25, 27–29, 63] and experimental efforts to implement it in various ion species [30–32, 35].

This chapter summarizes the work on the GZC and derived gate schemes. In section 4.1, the GZC gate scheme itself is introduced and the particularities of an implementation in $^{40}\text{Ca}^+$ are highlighted along references [24, 28]. Alternative gate schemes are outlined in section 4.2. Section 4.3 derives the requirements of a laser system suitable to implement the gate scheme in $^{40}\text{Ca}^+$ ions.

4.1 THE GZC PHASE GATE SCHEME

The idea behind reference [24] is to force the motional modes of an ion crystal onto ion-state-dependent trajectories through phase space, similar to [18] which was outlined in section 3.3. In both cases, the acquired geometric phase (difference) $(\Delta)\phi = (\Delta)A/\hbar$ is equal to the (difference of) phase space area(s) enclosed by the trajectory(-ies). For a clarifying picture see figure 4.1 and also compare to figure 3.3. However, instead of using continuous wave (CW) laser fields, GZC propose to use counter-propagating laser pulse pairs for applying a state dependent, stimulated force [64], i. e. to transfer momentum to the ion within a time $t \ll 2\pi/\omega$, with ω the trap frequency. Alternating between such kicks and times of free evolution in the trap potential then causes the motional modes to follow a state-dependent trajectory in phase space. GZC show that by carefully choosing the durations of free evolution the motional state is restored and therefore the phase space trajectory is closed, independent of the initial motional state and hence without temperature requirements.

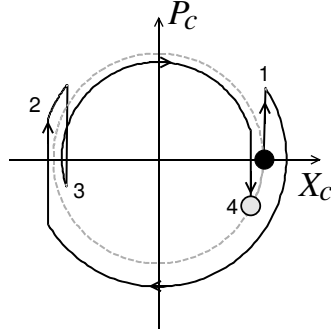


Figure 4.1: Trajectories of the center-of-mass state (X_c, P_c) in phase space. Unperturbed, the state will describe circles along the dashed circle. Applying state-dependent kicks, the state follows the solid line that connects the initial state (black circle) to the final state (gray circle). Vertical sections of the solid line are the effects of the kicks, arcs are times of free evolution. Image source: [24, figure 1]

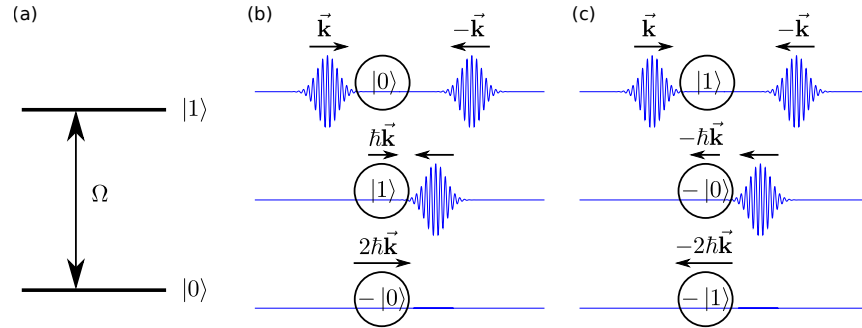


Figure 4.2: Effect of counter-propagating pulse pairs, resonant to the transition of the two-level system shown in (a). Every pulse acts as a π -pulse on this transition, the pulse pair transfers a momentum of $\vec{p} = 2 \langle \sigma_z \rangle \hbar \vec{k}$, where \vec{p} is parallel [anti-parallel] to \vec{k} if the ion is initially in state $|0\rangle$ (b) $|1\rangle$ (c).

Originally, GZC considered a two-ion crystal in a one-dimensional harmonic trapping potential. The two ions are assumed to be two-level systems with the pulsed laser field coupling the levels of both ions with the same Rabi frequency $\Omega(t)$, as seen in figure 4.2a. The laser pulses are assumed to be short, with a pulse length $\delta t \rightarrow 0$, but with $\Omega\delta t = \pi$. Therefore, Ω can become very large, in particular $\Omega \gg \omega_z$, which places the interaction in the strong-excitation regime.

To calculate the new interaction Hamiltonian, \hat{H} in equation (2.44) has to be replaced by the two-ion motional mode expansion from equation (2.37), and the new interaction Hamiltonian becomes

$$H'_{\text{int}} = \hbar \frac{\Omega(t)}{2} \sigma_1^+ e^{i/\sqrt{2}\eta_c(a^\dagger+a)+i/\sqrt{2}\eta_r(b^\dagger+b)} + \hbar \frac{\Omega(t)}{2} \sigma_2^+ e^{i/\sqrt{2}\eta_c(a^\dagger+a)-i/\sqrt{2}\eta_r(b^\dagger+b)} + \text{H.c.} \quad , \quad (4.1)$$

with $\eta_c = \eta$, $\eta_r = \eta/\sqrt[4]{3}$ ¹ and η the Lamb-Dicke parameter, see equation (2.46).

The full Hamiltonian can then be written as $H = H_{\text{H.O.}} + H'_{\text{int}}$ where $H_{\text{H.O.}} = \hbar\omega_c a^\dagger a + \hbar\omega_r b^\dagger b$ describes the motion in the harmonic potential, similar to equation (2.10), $\omega_c = \omega_z$ and $\omega_r = \sqrt{3}\omega_z$ are the frequencies of the center-of-mass and stretch mode, respectively, given by equation (2.33), and the a, a^\dagger and b, b^\dagger are the ladder operators of these modes, see equation (2.9).

Since the laser pulses satisfy $\Omega\delta t = \pi$, every laser pulse acts as a π -pulse and completely exchanges the populations of the coupled states. A counter-propagating pair of such pulses will therefore restore the initial internal state except for a phase factor of -1 and transfer a momentum of $\vec{p} = 2\langle\sigma_z\rangle\hbar\vec{k}$ to the ion, with \vec{k} the wave vector of the first pulse and $\langle\sigma_z\rangle = 1$ (-1) if the ion is initially in the $|0\rangle$ ($|1\rangle$) state. For a graphical explanation see figure 4.2b and 4.2c.

A sequence of laser pulses consists of N groups of pulse pairs. The groups are interspersed by times of free evolution of the motional modes. Group k is applied at time t_k and consists of z_k pulse pairs. The sign of z_k indicates which pulse of every pair of this group reaches the ion first. Changing the sign of z_k therefore changes the sign of the transferred momentum. The z_k pulse pairs evolve the state of the system according to

$$\mathcal{U}_{\text{kick}} = e^{-2iz_k k(x_1\sigma_1^z + x_2\sigma_2^z)}, \quad (4.2)$$

¹ These definitions for η_c and η_r are the same as in [28], but differ from those in [24] by a factor of $1/\sqrt{2}$ and $\sqrt{2}$, respectively.

where $k = |\vec{k}|$ and x_1, x_2 are the position of the ions [28]. Using equations (2.30), (2.35), (2.37) and (2.46), the unitary can be written as

$$\mathcal{U}_{\text{kick}} = e^{-\sqrt{2}iz_k\eta_c(a+a^\dagger)(\sigma_1^z+\sigma_2^z)}e^{\sqrt{2}iz_k\eta_r(b+b^\dagger)(\sigma_1^z-\sigma_2^z)} \quad (4.3)$$

$$= \hat{D}_c(-\sqrt{2}iz_k\eta_c(\sigma_1^z+\sigma_2^z)) \cdot \hat{D}_r(\sqrt{2}iz_k\eta_r(\sigma_1^z-\sigma_2^z)), \quad (4.4)$$

with the displacement operators $\hat{D}_c(\alpha) = \exp(\alpha a^\dagger - \alpha^* a)$ and $\hat{D}_r(\alpha) = \exp(\alpha b^\dagger - \alpha^* b)$ acting on their respective modes.

Adding the operator for free motional evolution,

$$\mathcal{U}_{\text{mot}} = e^{-i\omega_c\Delta t_k a^\dagger a} e^{-i\omega_r\Delta t_k b^\dagger b}, \quad (4.5)$$

with $\Delta t_k = t_{k+1} - t_k$, the total gate evolution can be written as

$$\mathcal{U}_{\text{gate}} = \prod_{k=1}^N \hat{D}_c(-ic_{ck})e^{-i\omega_c\Delta t_k a^\dagger a} \hat{D}_r(-ic_{rk})e^{-i\omega_r\Delta t_k b^\dagger b} \quad (4.6)$$

$$c_{(c,r)k} \equiv \pm\sqrt{2}z_k\eta_{(c,r)}(\sigma_1^z \pm \sigma_2^z), \quad (4.7)$$

where the plus (minus) sign is used for mode c (r).

For the two modes c and r , the effect of $\mathcal{U}_{\text{gate}}$ acting on a coherent state $|\alpha\rangle$ is

$$\mathcal{U}_{(c,r)}|\alpha\rangle = e^{i\tilde{\xi}_{(c,r)}}|\tilde{\alpha}_{(c,r)}\rangle, \quad (4.8)$$

where

$$\tilde{\alpha}_{(c,r)} = \alpha e^{-i\omega_{(c,r)}T_G} - i \sum_{k=1}^N c_{(c,r)k} e^{i\omega_{(c,r)}(t_k - T_G)} \quad (4.9)$$

$$\begin{aligned} \tilde{\xi}_{(c,r)} = \sum_{m=2}^N \sum_{k=1}^{m-1} \left[c_{(c,r)m} c_{(c,r)k} \sin(\omega_{(c,r)}(t_m - t_k)) \right] - \\ \text{Re} \left(\alpha \sum_{k=1}^N c_{(c,r)k} e^{-i\omega_{(c,r)}t_k} \right) \end{aligned} \quad (4.10)$$

and $T_G = t_N - t_1$ is the total time of the gate operation. The total displacement due to the gate operation is the second part of equation (4.9), namely

$$C_{(c,r)} = -i \sum_{k=1}^N c_{(c,r)k} e^{i\omega_{(c,r)}t_k}. \quad (4.11)$$

Since this quantity is state dependent and the motional state has to be restored at the end of the gate, it is required that $C_{(c,r)} = 0$ and these commensurability conditions can be written as

$$\begin{aligned} \sum_{k=1}^N z_k e^{-i\omega_c t_k} &= 0 \quad \text{and} \\ \sum_{k=1}^N z_k e^{-i\omega_r t_k} &= 0. \end{aligned} \quad (4.12)$$

If they are satisfied, the evolution operator \mathcal{U} is given by

$$\mathcal{U}(\Theta) = e^{i\Theta\sigma_1^z\sigma_2^z} e^{-i\omega_c T_G a^\dagger a} e^{-i\omega_r T_G b^\dagger b}, \quad (4.13)$$

where

$$\Theta = 4\eta^2 \sum_{m=2}^N \sum_{k=1}^{m-1} z_k z_m \left(\frac{\sin(\sqrt{3}\omega\Delta t_{km})}{\sqrt{3}} - \sin(\omega\Delta t_{km}) \right), \quad (4.14)$$

with $\Delta t_{km} = t_k - t_m$. If equations (4.12) are fulfilled and $\Theta = \pi/4$, the pulse sequence will act as a controlled-phase gate in the form of the unitary

$$\mathcal{U}(\pi/4) = \begin{pmatrix} 1 & 0 & 0 & 0 \\ 0 & -i & 0 & 0 \\ 0 & 0 & -i & 0 \\ 0 & 0 & 0 & 1 \end{pmatrix}, \quad (4.15)$$

disregarding the motional part of equation (4.13) and a global phase factor. Comparing equations (3.16) and (4.15) it is easy to see that the unitaries of these phase gates are equivalent.

The example sequence applies pulses to the ions at $N = 4$ different times. Its effect on the center-of-mass mode is plotted in figure 4.1 and a graphical representation of the pulse timing in figure 4.3. The sequence is defined as $(z_k, t_k) = (1, -\tau_1), (1, -\tau_2), (-1, \tau_2), (-1, \tau_1)$, with $\tau_1 = 0.54(2\pi/\omega) > \tau_2 > 0$ and therefore takes just over one trap period to complete, $T_G = 2\tau_1 = 1.08(2\pi/\omega)$ [24].

The following sections present a number of fast pulse sequences that take less than one trap period to complete, $T_G < (2\pi/\omega)$ and explore how the gate scheme can be implemented in $^{40}\text{Ca}^+$.

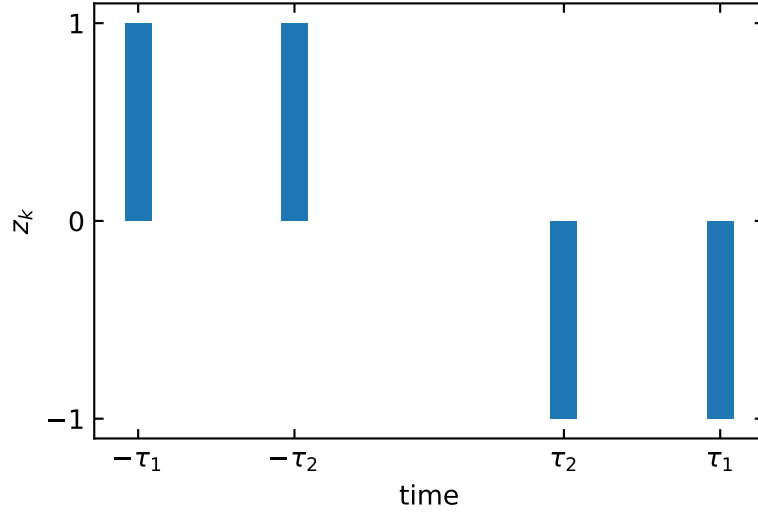


Figure 4.3: Timing of the simple GZC pulse scheme

4.2 PULSE SEQUENCES FOR FAST PHASE GATES

The authors of [28] have analyzed three pulse sequences, which enable fast phase gate operations in less than one trap period. One sequence was proposed by García-Ripoll, Zoller, and Cirac themselves, one by Duan and one by Bentley et al. Their findings are reproduced here.

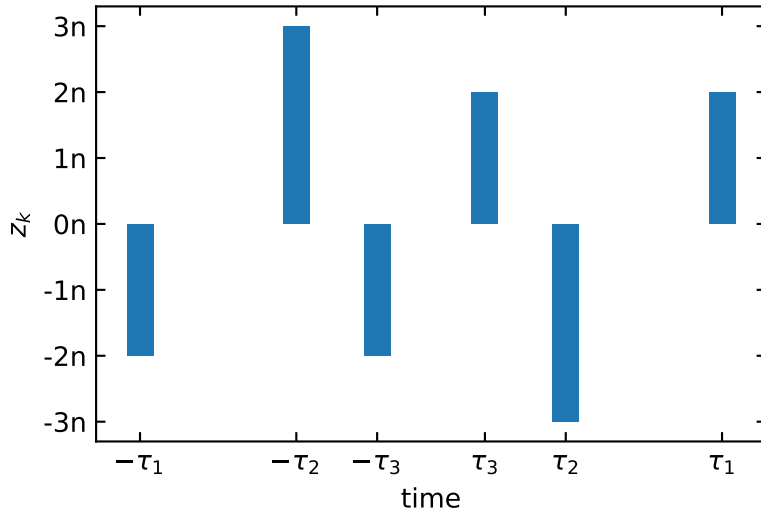
4.2.1 Fast GZC gate scheme

GZC proposed a second pulse sequence [24], defined by

$$(z_k, t_k) = \{(-2n, -\tau_1), (3n, -\tau_2), (-2n, -\tau_3), (2n, \tau_3), (-3n, \tau_2), (2n, \tau_1)\}. \quad (4.16)$$

For a graphical representation of the pulse timing see figure 4.4. The sequence consists of $N_p = \sum_k |z_k| = 14n$ pulse pairs and requires the time $T = 2\tau_1$ to complete. T scales with N_p as $T \propto N_p^{-2/3}$ and can be arbitrarily short, given the laser system is able to apply the required number of pulse pairs.

Bentley, Carvalho, and Hope have analyzed the effect of the pulse sequence on a two-ion crystal with $n = 10$ and $T = 222$ ns, both for an idealized laser source, which can apply all $|z_k|$ pulse pairs instantaneously, and for a more realistic laser, where two pulse pairs

Figure 4.4: Timing of the fast *GZC* pulse scheme

are separated by a pulse period of 200 ps, which corresponds to a laser repetition rate $f_{\text{rep}} = 5$ GHz. Their plots of the phase-space diagrams of both the center-of-mass mode and the stretch mode is reproduced in figure 4.5. They find that the idealized laser exactly solves the commensurability conditions in equations (4.12) and $\Theta = \pi/4$, and show that a laser with a 5 GHz repetition rate can complete a gate operation using this sequence in ~ 200 ns with error (1-fidelity) below 10^{-8} .

4.2.2 Duan gate scheme

The Duan pulse sequence [25] can be simplified to

$$(z_k, t_k) = (n, 0), (-2n, \tau_1), (n, 3\tau_1), \quad (4.17)$$

with the restriction, that there are no times of free evolution other than during the pulse period, i. e. $\tau_1 = n/f_{\text{rep}}$. A graphical representation of the pulse timing is plotted in figure 4.6. For a given repetition rate and trap frequency, the integer n has therefore to be chosen such to satisfy the phase equation (4.14). According to [28], this leads to an error in restoring the initial motional state, which can be seen in figure 4.7. Although the sequence can be repeated one or more times in order to increase the motional stability, the scheme is not an exact solution to

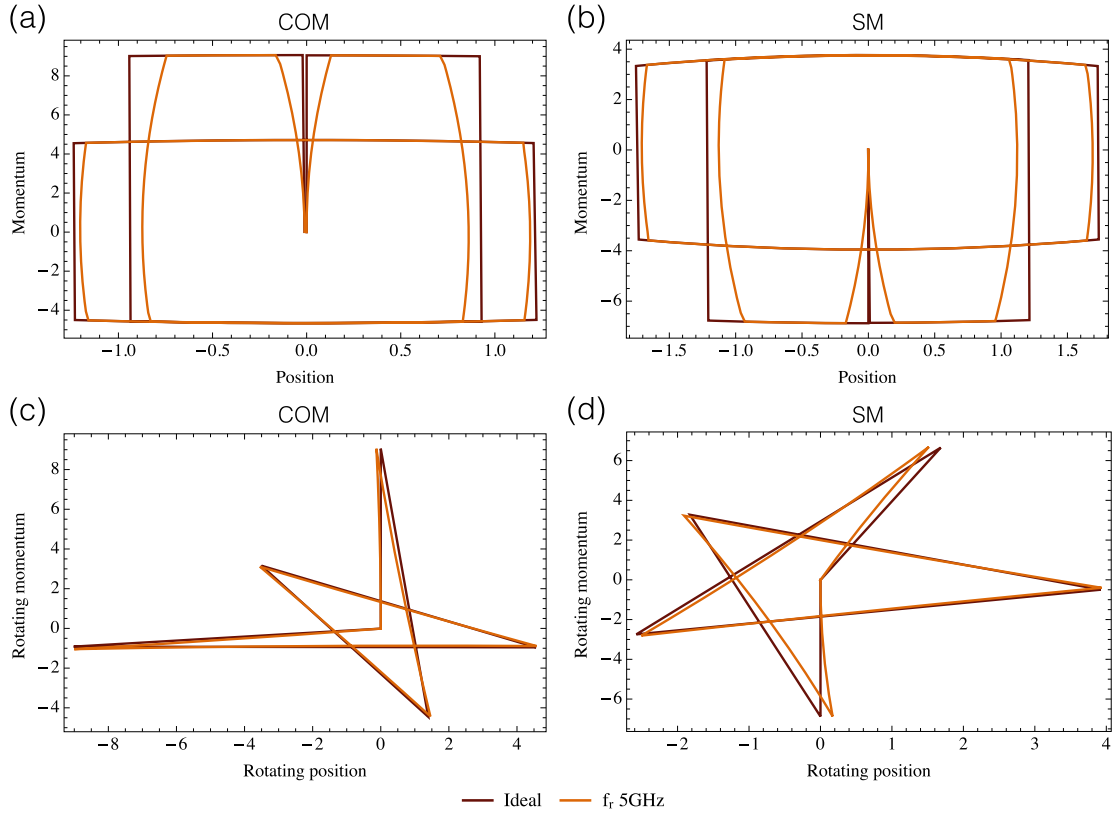


Figure 4.5: Fast [GZC](#) pulse scheme in non-rotating (a), (b) and rotating (c), (d) phase space with $n = 10$ for both the center-of-mass (COM) and stretch (SM) motional modes of a two ion crystal. The phase-space trajectory is plotted for an idealized laser source with infinite repetition rate (brown) and a laser with a repetition rate of 5 GHz (orange). Image source: [\[28, figure 1\]](#)

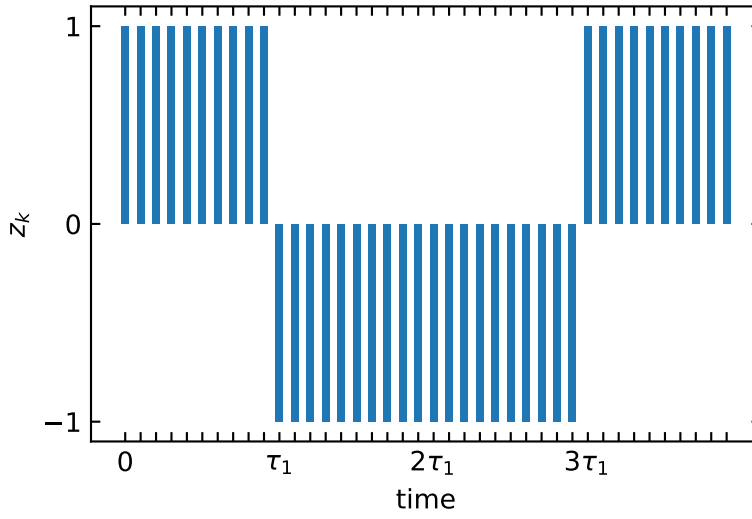


Figure 4.6: Timing of the Duan pulse scheme for $n = 10$

the commensurability conditions in equation (4.12) and repeating the sequence comes at the cost of increasing the gate time.

4.2.3 FRAG gate scheme

The fast robust antisymmetric gate (FRAG) pulse sequence, proposed in [27], is defined by [28]

$$(z_k, t_k) = (-n, -\tau_1), (2n, -\tau_2), (-2n, -\tau_3), (2n, \tau_3), (-2n, \tau_2), (n, \tau_1). \quad (4.18)$$

Figure 4.8 shows the graphical representation of the pulse timing. The sequence is the result of a search for a gate scheme that uses large-area pulses and splits them into several (here: $20n$) pulses of area π , that is experimentally implementable and that is optimal in the sense that it both minimizes the gate duration and maximizes its fidelity. Like the GZC pulse sequences, the FRAG sequence solves both commensurability conditions in equation (4.12) and satisfies $\Theta = \pi/4$ in equation (4.14).

The plots in figure 4.9 show that the phase-space trajectories of the FRAG scheme are similar to those of the GZC scheme (compare with figure 4.5).

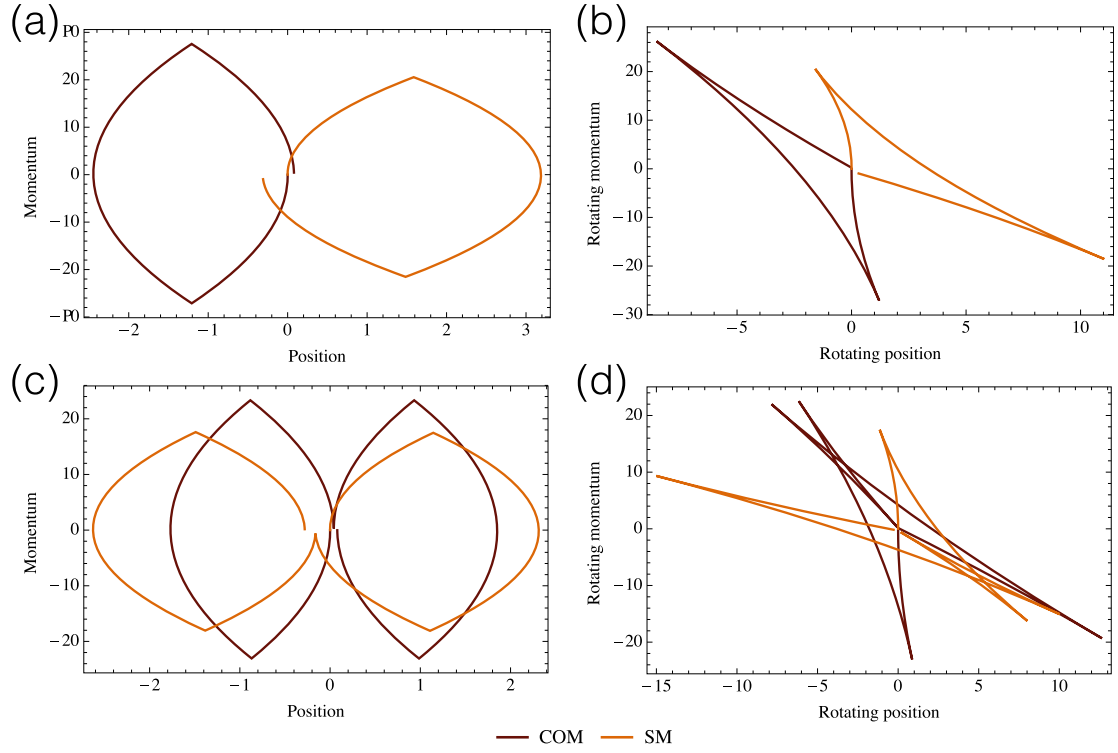


Figure 4.7: Duan pulse scheme in non-rotating (a), (c) and rotating (b), (d) phase space with $n = 10$ for a single-cycle (a), (b) and double-cycle (c), (d) scheme. The phase-space trajectory is plotted for both the center-of-mass (COM, brown) and stretch (SM, orange) motional modes of a two ion crystal. The laser is assumed to have a repetition rate of 5 GHz. The rotating phase-space plots show clearly, that the motional modes are not restored to the initial motional state. Image source: [28, figure 3]

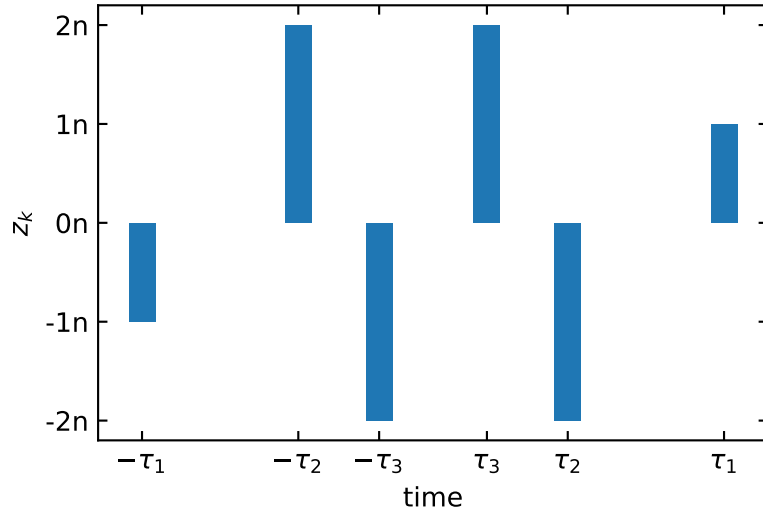


Figure 4.8: Timing of the FRAG pulse scheme

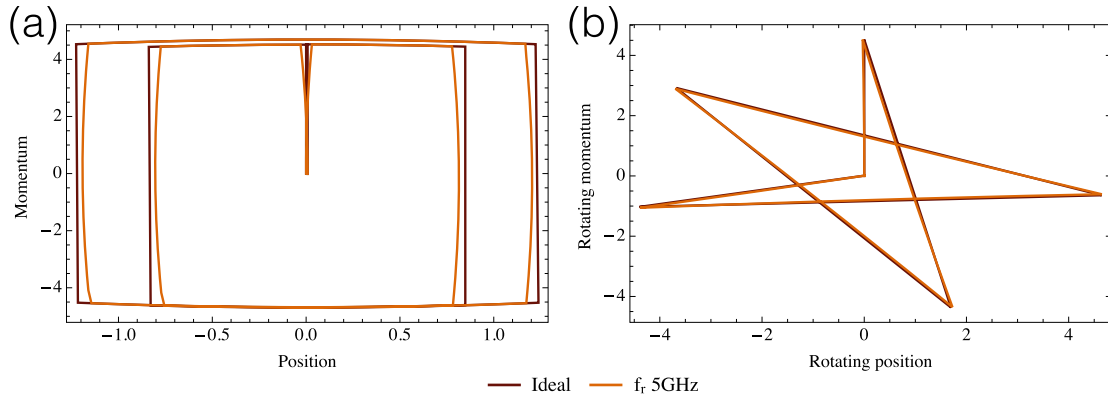


Figure 4.9: FRAG pulse scheme in non-rotating (a) and rotating (b) phase space with $n = 10$ for the center-of-mass (COM) motional mode of a two ion crystal. The phase-space trajectory is plotted for an idealized laser source with infinite repetition rate (brown) and a laser with a repetition rate of 5 GHz (orange). Image source: [28, figure 2]

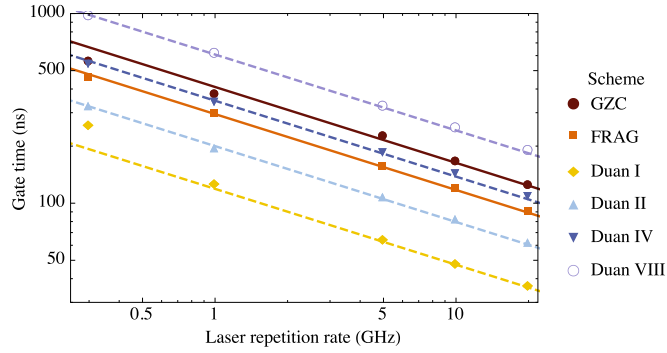


Figure 4.10: Gate time as a function of repetition rate for the presented schemes. The fits show the optimal scaling of gate time with pulse number. Solid lines are fit to the high-fidelity FRAG and GZC gates with error (1-fidelity) below 10^{-8} . Dashed lines are fit to the Duan scheme, which has much lower fidelity. The Roman numerals enumerate the number of repetitions of the Duan scheme. Source: [28, figure 4]

4.2.4 Comparison of fast gate schemes

Of the three schemes presented here, both the fast GZC scheme and the FRAG scheme seem to be suitable for implementation. Their realization would require technically equal amounts of time and effort, and they also are quite similar in terms of speed and fidelity as is shown in figure 4.10 and table 4.1.

The Duan scheme on the other hand is potentially very fast but with a fidelity of only 0.65. The fidelity can be improved to 0.97 but at the cost of speed and it remains poor compared to the other schemes. Furthermore, its experimental realization is complicated by the requirement to switch the pulses' momentum transfer from one direction to the other within the time between two consecutive pulses, i. e. 200 ps in this case. Since it is planned to switch the momentum transfer direction using a Pockels cell with a rise time of 5 ns (see section 5.3), the Duan scheme appears to be unsuitable for implementation in this thesis' experimental setup.

SCHEME	T_G (ns)	1 - FIDELITY	PROS & CONS
Fast GZC	220	$<10^{-8}$	fast and high fidelity
Duan I	65	0.35	very fast but low fidelity, difficult to implement
Duan IV	330	0.03	relatively slow with medium fidelity, difficult to implement
FRAG	170	$<10^{-8}$	fast and high fidelity

Table 4.1: Comparison of fast gate schemes, assuming a laser repetition rate of 5 GHz.

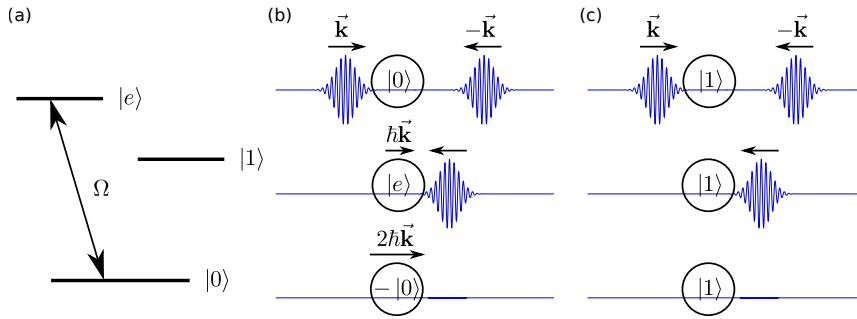


Figure 4.11: Effect of counter-propagating pulse pairs, resonant to the auxiliary transition $|0\rangle \leftrightarrow |e\rangle$ of the three-level system shown in (a). Every pulse acts as a π -pulse on this transition, the pulse pair transfers a momentum of $\vec{p} = 2 \langle i|\zeta^z|i\rangle \hbar \vec{k}$, with $\langle i|\zeta^z|i\rangle = 1 - i$.

4.3 REQUIREMENTS FOR AN EXPERIMENTAL REALIZATION

4.3.1 GZC scheme in $^{40}\text{Ca}^+$

In order to implement the fast phase gate operation in $^{40}\text{Ca}^+$, one can use the $4S_{1/2} \leftrightarrow 4P_{3/2}$ transition to transfer momentum to the ions [28]. In contrast to the previous assumptions of a two-level system where both qubit states are effected by the laser pulses, these only couple to the $|0\rangle$ state in this case, while the $|1\rangle$ state, which is encoded in the $3D_{5/2}$ manifold, is left untouched. This situation is depicted in figure 4.11 (also compare to figure 4.2). Furthermore, the pulse lengths can no longer be assumed to be infinitesimally short, but need to be

much longer than the atomic transition periods of $\mathcal{O}(10^{-15} \text{ s})$ in order to satisfy the rotating wave approximation.

Since only one of the qubit states is affected by the momentum kicks, the unitary from equation (4.2) becomes

$$\mathcal{U}_{\text{kick}} = e^{-2iz_k k(x_1 \zeta_1^z + x_2 \zeta_2^z)}, \quad (4.19)$$

where ζ^z is the Pauli z matrix acting only on the $|0\rangle$ and $|e\rangle$ levels, not on $|1\rangle$: $\zeta^z |0\rangle = |0\rangle$, $\zeta^z |e\rangle = -|e\rangle$ and $\zeta^z |1\rangle = 0$. This leads then to the asymmetric phase condition equation

$$\Theta = \eta^2 \sum_{m=2}^N \sum_{k=1}^{m-1} z_k z_m \left(\frac{\sin(\sqrt{3}\omega \Delta t_{km})}{\sqrt{3}} - \sin(\omega \Delta t_{km}) \right), \quad (4.20)$$

which differs from the symmetric case – shown in equation (4.14) – only in the missing factor of 4 on the right-hand side.

4.3.2 Requirements on a laser system for a fast phase gate operation

Five key requirements on a laser system, able to implement a fast phase gate operation, can be identified:

1. The system needs to provide pulsed laser light with a repetition rate much larger than the trap frequency of $\sim 1 \text{ MHz}$, in order to provide for fine-grained control over the timing of pulse sequences.
2. The pulse length δt has to be much shorter than the $^{40}\text{Ca}^+ 4\text{P}_{3/2}$ state's lifetime $\tau_P = 6.9 \text{ ns}$ [50] to avoid or at least minimize spontaneous decay, and much longer than the atomic transition period $\tau_A = \lambda/c = 1.3 \text{ fs}$ of the $4\text{S}_{1/2} \leftrightarrow 4\text{P}_{3/2}$ transition, with $\lambda = 393 \text{ nm}$ and c the speed of light in vacuum:

$$\tau_A \ll \delta t \ll \tau_P$$

3. The center frequency of the laser light has to be resonant with the $4\text{S}_{1/2} \leftrightarrow 4\text{P}_{3/2}$ transition at 393.366 nm .
 - b) Alternatively, non-resonant pulses can be used to apply state-dependent momentum kicks [33]. In order to realize this alternative, the laser system's center frequency needs to be tuned in-between the two fine structure components

$4S_{1/2} \leftrightarrow 4P_{1/2}$ and $4S_{1/2} \leftrightarrow 4P_{3/2}$ such that Stark shifts cancel, while limiting overlap of the laser with the $4P_{1/2} / 4P_{3/2}$ gap.

4. The laser intensity needs to be high enough to achieve a complete population transfer between the two levels by a single laser pulse.
5. There needs to be a way to control the direction of the state-dependent momentum kick, i.e. to control which pulse of a pulse pair reaches the ions first.

Part II

THE LASER, EXPERIMENTAL SETUP AND RESULTS

A PULSED LASER SYSTEM FOR AN ULTRAFAST PHASE GATE OPERATION

For the proposed fast phase gate operation in $^{40}\text{Ca}^+$, a picosecond laser system with a repetition rate on the order of GHz and a center wavelength of 393.366 nm can be constructed by frequency-quadrupling the light generated by commercial lasers operating in the L-band of optical fiber communication (1565 nm to 1625 nm). An overview of the optical setup is provided in figure 5.1.

The system is seeded by an optical frequency comb (panel A). Filter cavities serve to multiply the laser's repetition rate. Subsequently, the desired laser wavelength range is selected by spectral filters and the laser output is amplified (panel B). Fast and slow pulse picking elements enable the selection of arbitrary pulse sequences (panel C). Finally, the laser frequency is quadrupled by two single-pass second harmonic generation (SHG) stages (panel D).

Parts of this chapter have been published before – though in less detail – in reference [65].

5.1 SEED LASER: AN OPTICAL FREQUENCY COMB

An idealized frequency comb consists of a cavity of length L in which a single laser pulse circulates. It emits copies of that pulse which are separated by the cavity's round-trip time $T = 2L/v_g$, where v_g is the mean group velocity. The rate at which pulses are emitted is called the repetition rate $f_{\text{rep}} = 1/T$. The pulse copies are identical except for the phase between the carrier wave and the intensity envelope: it changes from pulse to pulse by the carrier envelope offset (CEO) phase $\Delta\phi_{\text{CEO}}$ as is illustrated in figure 5.2. The spectrum of an infinitely long train of pulses consists of equidistant modes, separated by f_{rep} and limited by a spectral envelope. These modes are offset by the CEO frequency $f_{\text{CEO}} = \frac{1}{2\pi}\Delta\phi_{\text{CEO}} \cdot f_{\text{rep}}$ and the frequency of the mode with mode number n is

$$f_n = f_{\text{CEO}} + n \cdot f_{\text{rep}}. \quad (5.1)$$

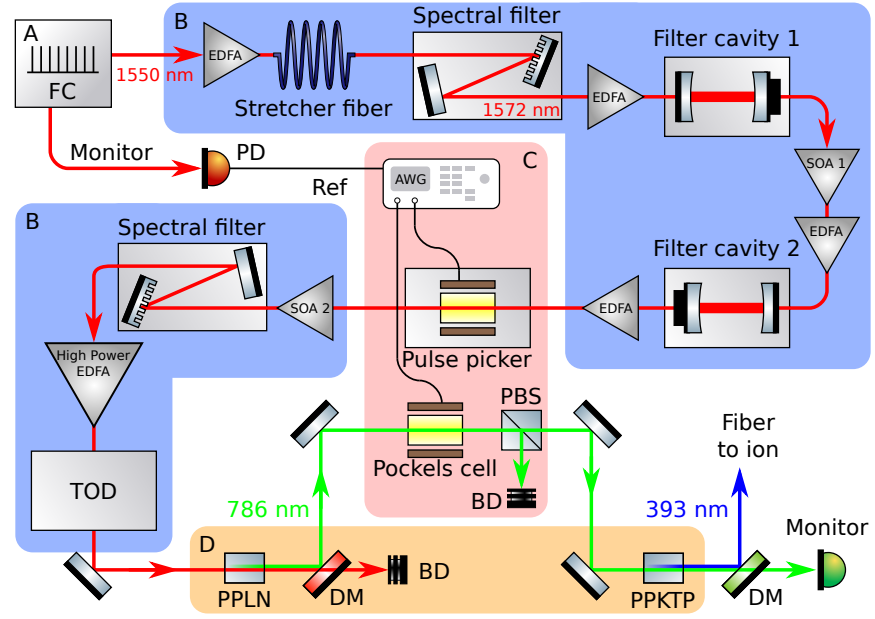


Figure 5.1: Schematic setup of our laser system. The lettered panels are described in detail in the following sections: Panel A: Section 5.1, panel B: Section 5.2, panel C: Section 5.3, panel D: Section 5.4. AWG: arbitrary waveform generator, BD: beam dump, DM: dichroic mirror, EDFA: erbium-doped fiber amplifier, FC: optical frequency comb, PBS: polarizing beam splitter, PD: photo detector, PPLN: periodically poled lithium niobate, PPKTP: periodically poled potassium titanyl phosphate, SOA: semiconductor optical amplifier, TOD: third order dispersion compressor. This figure was taken from [65].

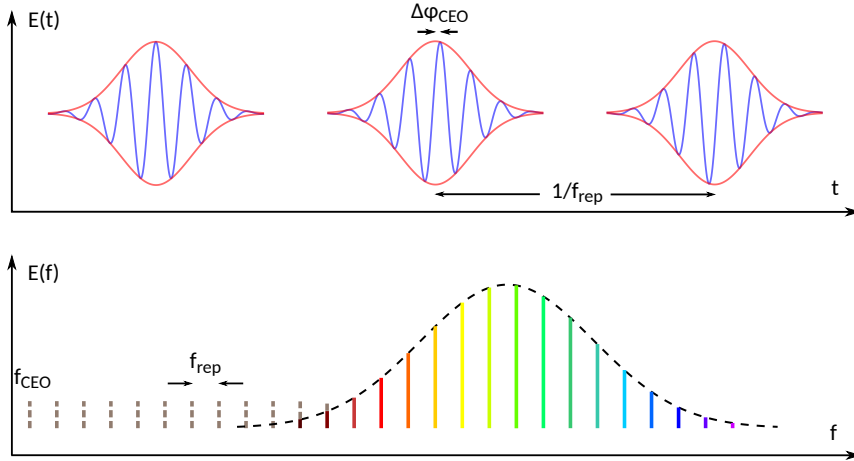


Figure 5.2: Schematic pulse train in time and frequency domain.
Adapted from [40].

In this work, a fiber-based optical frequency comb¹ with $f_{\text{rep}} = 250$ MHz and $f_{\text{CEO}} = 20$ MHz was used to seed the laser system (panel A in figure 5.1). Figure 5.3 gives an overview of the comb and its stabilization electronics. The laser consists of a fiber ring and free-space optics (panel A). The active part of the fiber ring is doped with erbium ions and pumped by an external diode laser. Four waveplates – two at each end of the fiber – control the laser’s mode of operation, passively mode-locked or continuous wave (CW). The laser operates in a mode-locked state if the waveplates compensate the non-linear (i. e. intensity-dependent) polarization rotation of the fiber ring such that the losses at the out-coupling polarizing beam splitter (PBS) are minimal for the maximum optical intensity. The mode-locked laser creates short pulses of 74 fs pulse width with a center wavelength of 1570 nm and a spectral bandwidth of 45 nm. The length of the fiber ring, and therefore the repetition rate, can be controlled by a piezo-mounted back-reflecting mirror and an intracavity electro-optic modulator (EOM). The CEO frequency can be coarsely adjusted in steps of ~ 1 MHz by a wedge that is pushed in or pulled out of the beam path by a stepper motor. Modulating the current of the pump diode also allows one to control f_{CEO} .

¹ Menlo Systems FC1500-250-WG

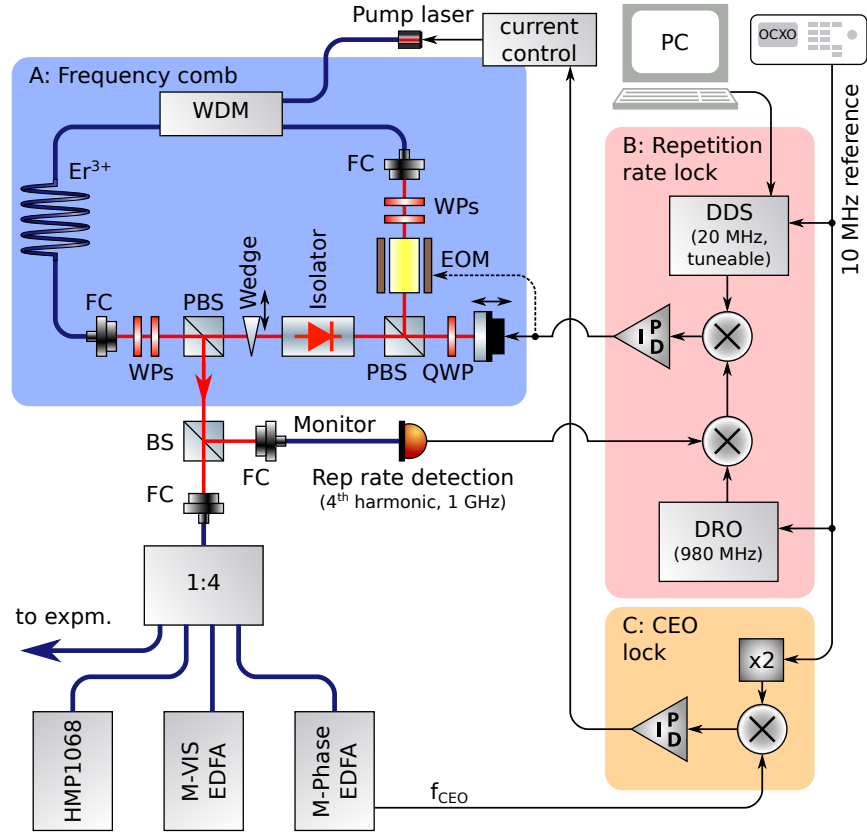


Figure 5.3: Schematic overview of the optical frequency comb and lock electronics. (P)BS: (polarizing) beam splitter, CEO: carrier-envelope offset, EDFA: erbium doped fiber amplifier, EOM: electro-optic modulator, DDS: direct digital synthesizer, DRO: dielectric resonator oscillator, FC: fiber coupler, OCXO: oven-controlled crystal oscillator, PID: proportional-integral-derivative controller, QWP: quarter-wave plate, WDM: wavelength division multiplexer, WP: waveplate.

Both f_{CEO} and f_{rep} are locked to a frequency reference provided by a GPS-disciplined oven-controlled crystal oscillator² with a fractional frequency instability of $\sim 2 \times 10^{-13}$. In order to measure and stabilize f_{CEO} , light from the comb is amplified and spectrally broadened to an octave spanning spectrum. Frequency doubled light from the red end of the spectrum at frequency $2 \cdot f_n = 2 \cdot (f_{\text{CEO}} + n \cdot f_{\text{rep}})$ is beat with light from the blue end of the spectrum at frequency $f_{2n} = f_{\text{CEO}} + 2n \cdot f_{\text{rep}}$ to create the frequency difference at $f_{\text{beat}} = 2 \cdot f_n - f_{2n} = f_{\text{CEO}}$. As seen in panel C of figure 5.3, the f_{CEO} signal is then stabilized in a phase-locked loop (PLL) by feeding back on the current of the comb's pump diodes.

The f_{rep} signal can be measured directly by detecting it with a fast photo diode. In order to increase sensitivity the fourth harmonic at 1 GHz is detected. After mixing it down to 20 MHz by a fixed frequency signal at 980 MHz, a PLL stabilizes f_{rep} to a variable direct digital synthesizer (DDS) frequency around 20 MHz by feeding back on a piezo controlling the length of the comb's fiber ring (panel B). Alternatively, f_{rep} can be stabilized by using an optical beat between the comb and another stable (CW) laser and additionally feeding back to an intracavity EOM.

In addition to measuring and stabilizing the CEO frequency and to seeding the laser system described in this chapter, the comb's output is also used for determining the frequency of CW lasers of wavelengths from 729 nm to 866 nm and around 1068 nm. The light for measuring the former wavelength range is created by first amplifying and frequency doubling the comb's output light. Then, the light is coupled into a nonlinear photonic-crystal fiber (PCF) which broadens the light's spectrum to the aforementioned range. The light for measuring lasers around 1068 nm is created by also first amplifying and then frequency-shifting the comb's output light to that wavelength. For a more detailed description see section 4.2.4 of reference [40].

5.2 PULSE AMPLIFICATION AND FILTERING

In order to meet all four pulse criteria described earlier, a number of pulse characteristics need to be manipulated:

- The pulses should be amplified to cancel the insertion loss of the optical elements (typically on the order of a few dB each) and be able to act as a π -pulse after frequency doubling.

² Menlo Systems GPS 6-12

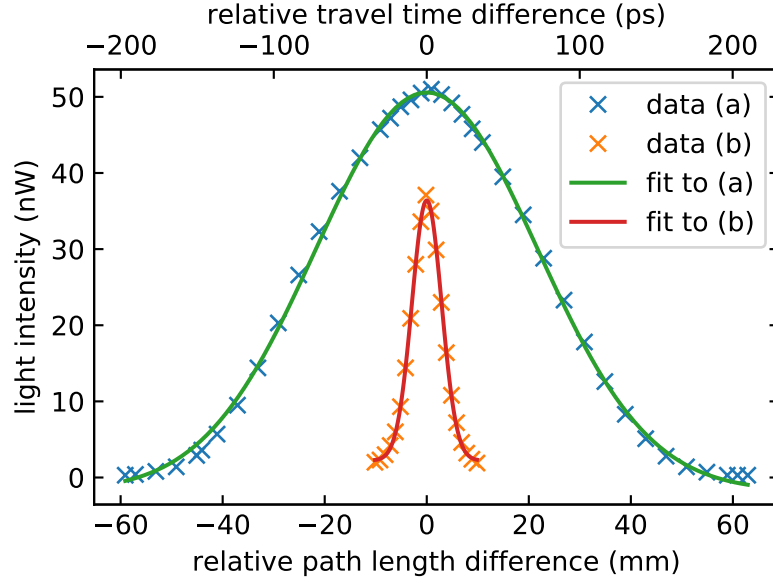


Figure 5.4: Intensity autocorrelation of chirped pulses, measured (a) at the output of the stretcher fiber and (b) at the output of the high power EDFA (compare with figure 5.1). The solid lines are Gaussian bell curves, fit to the data. From the fit FWHM of (a) 51.2(5) mm, the pulse width τ can be calculated: $\tau_{(a)} = 51.2(5) \text{ mm} / (\sqrt{2}c) = 120.8(13) \text{ ps}$, $\tau_{(b)} = 6.83(5) \text{ mm} / (\sqrt{2}c) = 16.1(1) \text{ ps}$.

- The spectral bandwidth should be limited to about 1 THz ($\hat{=}$ 0.5 nm at 393 nm) to avoid residual off-resonant excitation of the $4S_{1/2} \leftrightarrow 4P_{1/2}$ transition.
- The center wavelength should be resonant to the $4S_{1/2} \leftrightarrow 4P_{3/2}$ transition.
- In order to have a higher resolution of the pulse timings, the repetition rate is additionally multiplied by a factor of 20.

Erbium doped fiber (pre-)amplifiers (EDFAs) and semiconductor optical amplifiers (SOAs) are used to compensate insertion loss at various stages in the set-up (panels B in figure 5.1). After the first pre-amplifier, the pulse train travels through a stretcher fiber³ which adds normal dispersion and stretches the pulses from 74 fs to 120.8(13) ps for chirped pulse amplification [66]. Part (a) of figure 5.4 shows the autocorrelation

³ ~40 m OFS UltraWave Ocean Fiber IDF

LOCATION	P (mW)	λ_C (nm)	$\Delta\lambda$ (nm)
after stretcher fiber	210	1570	45
after 1st spectral filter	4.7	1572.9	8.7
after cavity 1	1.9	1570.6	8.5
after cavity 2	3.1	1572.8	10.9
before pulse picker	12.7	1573.1	9.7
after pulse picker	2.6	1573.0	9.3
after SOA 2	38.5	1577.1	6.2
after 2nd spectral filter	14.8	1577.2	6.1
after 1st stage of HP EDFA	240	1575.3	6.1
after TOD	variable	1573.4	7.4

Table 5.1: Overview of important light parameters within the laser system. P : light power, λ_C : center wavelength, $\Delta\lambda$: bandwidth

spectral filter is used to compensate amplifier-induced frequency shifts [67] of up to 4 nm and further to limit the bandwidth to 6.4 nm. Next, a high power EDFA amplifies the pulse train from 15 mW to a maximum average power of 7 W. At this point, the pulses have been shortened to 16.1(1) ps as shown in figure 5.4b. The shortening of the pulse is dominated by the spectral filtering but also due to anomalous dispersion in the silica fibers of the system. Finally, a free-space third-order dispersion (TOD) compressor reduces the pulse width to 680 fs (time bandwidth product 0.53) which is close to the transform limited pulse width of 560 fs for a Gaussian-shaped pulse of the given bandwidth.

5.3 PULSE PICKING

In order to select the pulse sequences described in section 4.1 out of the 5 GHz pulse train, an optical element is needed that is able to select pulses at this rate and to withstand up to 2.8 W of laser power after the high power EDFA. To satisfy both requirements, a twofold approach was chosen, using a fast switching element before the high power EDFA (where the average laser power can be limited to 10 mW) and a slow element after the amplifier to create the desired pulse

sequences. A schematic of the setup is shown in panel C in figure 5.1 (page 50).

The fast element is a pulse picker⁴ which contains a Mach-Zehnder interferometer with an EOM of 7 GHz bandwidth. It also features a DC bias input and appropriate control electronics which are needed to correct for (thermal) drift of the interferometer and to optimize the pulse picker's extinction ratio. The voltage to be applied to the DC bias input depends on the duty cycle of the EOM input signal because the EOM input is capacitively coupled (AC coupled). A description of how to determine the DC bias voltage can be found in appendix A.

Since the pulse picker's maximum optical input power is on the order of a few mW, it is installed before the high power EDFA where the light intensity is sufficiently low. Considering the amplifier's need to be seeded continuously with a maximally allowed dark time on the order of 20 ns, an additional switching element is needed after the amplifier with a high damage threshold and a switching time of less than 20 ns. For this, a barium borate (BBO) Pockels cell⁵ is used, with a driver⁶ that enables switching of the cell with a rise/fall time of 7 ns at a maximum repetition rate of 10 MHz and a measured optical extinction ratio of 30 dB. Its specified half-wave voltage is 4.16 kV at 790 nm.

Both the pulse picker and the Pockels cell are controlled by an AWG⁷ with a sample rate of 25 GS/s. Figure 5.6 shows a detailed schematic setup of the AWG. It is synchronized with the frequency comb by a 250 MHz radio frequency (RF) signal derived directly from the laser's pulse train. Channel 1 of the AWG is amplified and fed into the pulse pickers EOM, channel 2 is used to create a 156 MHz clock signal for a delay generator⁸ that turns a single transistor-transistor logic (TTL) trigger from the AWG into the start and stop signals for the Pockels cell.

The delay generator controls the BBO Pockels cell via a splitter box⁹ as shown in figure 5.7. The splitter box only allows switching the Pockels cell every 35 ns ($\hat{=}$ 14 MHz maximum repetition rate) to prevent damage to the Pockels cell driver. Figure 5.8 shows a schematic switching sequence indicating this limitation. The second Pockels cell

⁴ custom-made Modbox by Photline, now iXblue

⁵ Leysop BBO-3-25-AR790

⁶ Bergmann Meßgeräte Entwicklung PCD_bpp

⁷ Tektronix AWG 70002A

⁸ 2x Bergmann Meßgeräte Entwicklung BME_SGo8p

⁹ Bergmann Meßgeräte Entwicklung BME_GSo1

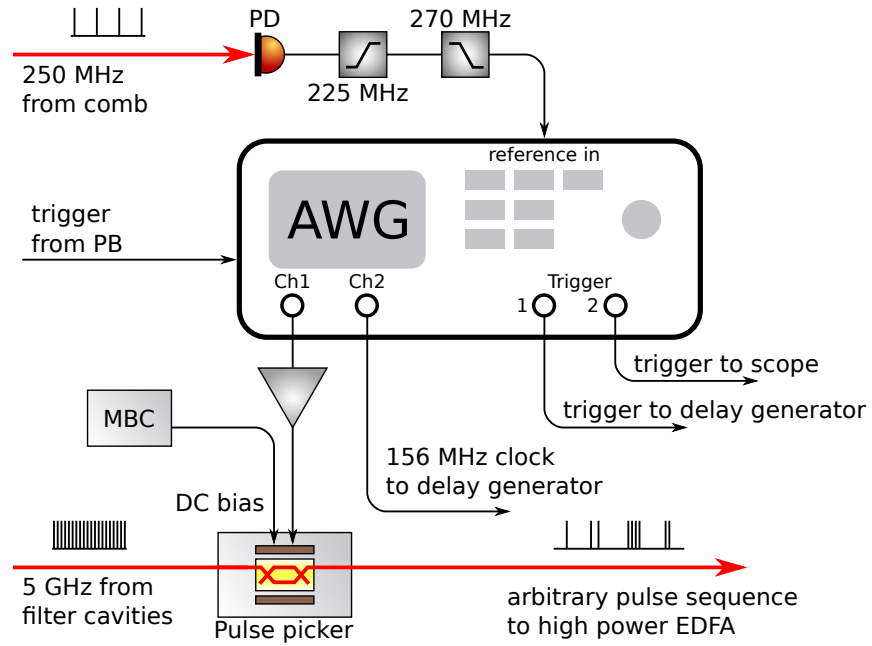


Figure 5.6: Schematic overview of the AWG and pulse picker setup. The AWG outputs a pre-programmed bit-pattern on channel 1. This signal is amplified and sent to the pulse picker, which blocks or transmits the optical pulses according to the bit-pattern. The 250 MHz comb signal references both the AWG and the 5 GHz pulse train to ensure synchronism. AWG: arbitrary waveform generator, EDFA: erbium doped fiber amplifier, MBC: modulator bias controller, PB: pulse box, PD: photo detector.

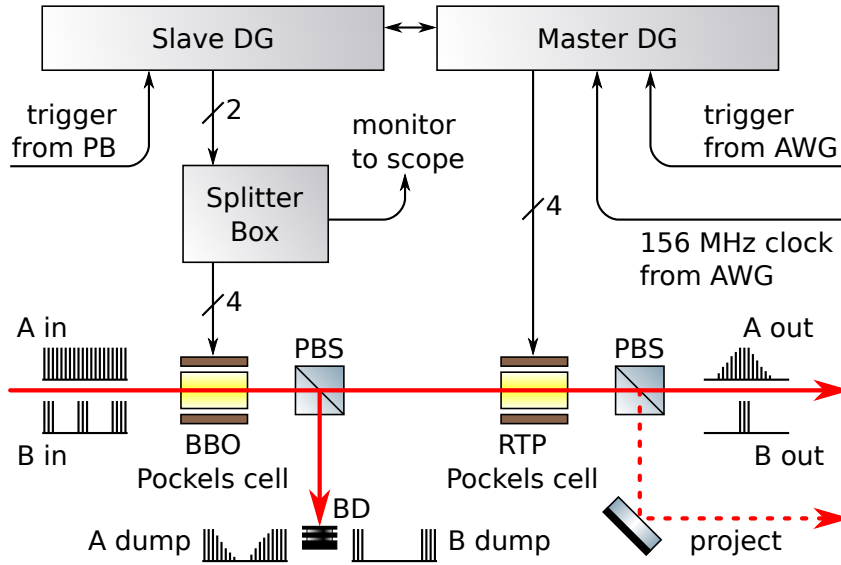


Figure 5.7: Schematic overview of the delay generator and Pockels cell setup. The delay generators are triggered either by the [AWG](#) or the pulse box. After a predefined delay of $\mathcal{O}(\text{ns})$, the Pockels cells are first switched on and after another delay switched off. Depending on the input signal (A in or B in) the rise and fall times of the Pockels cell will be visible (A out) or suppressed (B out). AWG: arbitrary waveform generator, BBO: barium borate, BD: beam dump, DG: delay generator, PB: pulse box, PBS: polarizing beam splitter, RTP: rubidium titanyl phosphate.

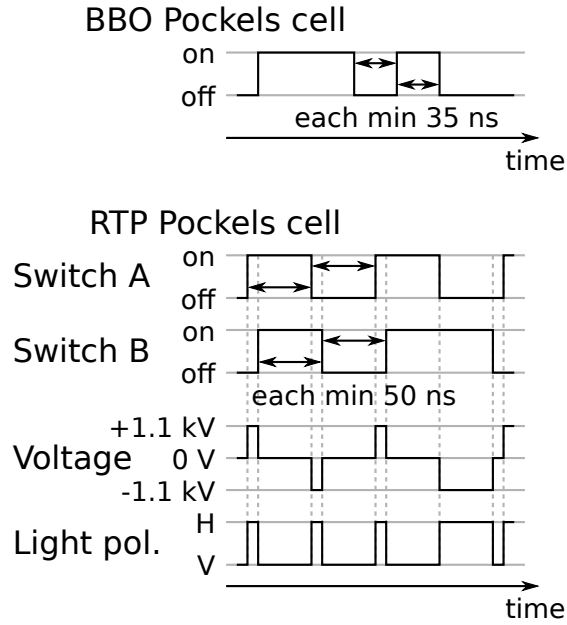


Figure 5.8: Schematic switching sequence of BBO and RTP Pockels cells.

shown in figure 5.7 is made from rubidium titanyl phosphate (RTP)¹⁰ and uses a driver¹¹ that enables switching of the cell with a rise/fall time of 5 ns at a maximum repetition rate of 20 MHz. Due to its specified half-wave voltage of 1.1 kV at 790 nm – which is much less than the 4.16 kV of the BBO Pockels cell – it is possible to switch the RTP Pockels cell at this higher rate. Both Pockels cells have four TTL inputs, two “on” and two “off” inputs (“A on”, “A off”, “B on”, “B off”). In the case of the BBO Pockels cell, both on (off) inputs have to be triggered simultaneously. After switching the cell on (off), the waiting time of 35 ns has to be strictly observed before switching it off (on) again. In the case of the RTP Pockels cell, the two input groups (A and B) can be switched independently, but the waiting time between switching the same input group is 50 ns as indicated in figure 5.8.

At the time of this writing the RTP Pockels cell is already installed in the beam path but is not in use. Its purpose will be to switch the pulses between two different beam paths (see figure 9.1 on page 130) and thus enable one to choose which pulse of each counter-propa-

¹⁰ Leysop RTP-4-20-AR650-1000

¹¹ Bergmann Meßgeräte Entwicklung PCD_dpp

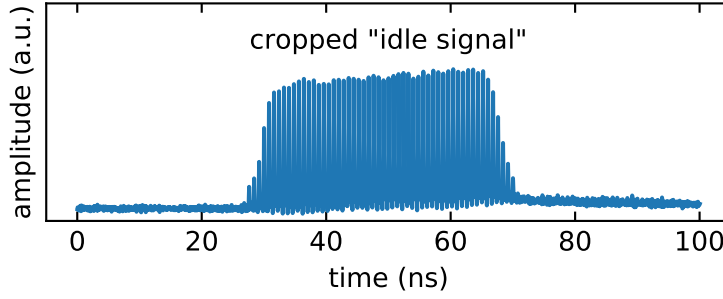


Figure 5.9: Pulse train mode: The [AWG](#) outputs the idle signal (here at 1.25 GHz) which is turned into an optical signal by the pulse picker. The optical signal is cropped by the Pockels cell. Figure adapted from [65].

gating pulse pair reaches the ion first (for an explanation why this is necessary see section 4.1).

5.3.1 Modes of operation

The [AWG](#) and delay generator are set up to work in two different modes of operation. In the first mode, the [AWG](#) continuously outputs a periodic signal and only the [BBO](#) Pockels cell switches the pulse train on and off from the ion's point of view. This mode is therefore called the *pulse train mode*. In the second mode of operation both [AWG](#) and [BBO](#) Pockels cell are used to send an arbitrary number of pulses to the ion. This mode is called the *single pulses mode*.

5.3.1.1 Pulse train mode

In this mode the [AWG](#) outputs a signal such that the pulse picker picks only every n^{th} pulse, and outputs a pulse train with a repetition rate of $5/n$ GHz, typically $n \in [1, 2, 3, 4]$. This signal is called the *idle signal* and can be seen in figure 5.9. Further down in the beam path the [BBO](#) Pockels cell and a [PBS](#) are used to either direct the pulses into a beam dump (Pockels cell off) or towards the ion (Pockels cell on). Triggering the delay generator with a [TTL](#) signal – which usually is generated by the pulse box (see section 7.3.1) – turns on the [BBO](#) Pockels cell for as long as the [TTL](#) signal is in the logical high level. This mode therefore allows sending pulse trains of 30 ns and longer (up to continuously) to the ion because the Pockels cell driver can not be switched faster.

idle signal

Since the Pockels cell's rise and fall times of 7 ns are much longer than typical pulse periods of the idle signal of $n \cdot 200$ ps this causes the pulses during the rise and fall times to be attenuated with respect to other pulses. Nevertheless, due to the long pulse trains of typically $\gtrsim 1 \mu\text{s}$ effects of these attenuated pulses can be neglected.

5.3.1.2 Single pulses mode

payload signal

In contrast to the pulse train mode, the single pulses mode allows one to send from 0 to an arbitrary number of pulses and also arbitrary pulse sequences to the ion – limited only by the [AWG](#)'s memory of 2 GS. This pulse sequence is called the *payload signal* or just *payload* and is shown in figure 5.10. As long as no pulses should reach the ion the [AWG](#) outputs the idle signal to keep the high power [EDFA](#) seeded, while the [BBO](#) Pockels cell remains switched off. When the payload should be sent to the ion, the [AWG](#) triggers the delay generator to switch on the [BBO](#) Pockels cell, while simultaneously switching off the pulse picker for at least 12 ns before sending the payload. This ensures the Pockels cell has completely turned on before sending the pulses of the payload. After the payload signal has been sent, the [AWG](#) again switches off the pulse picker so the Pockels cell has time to switch off as well. Finally, the [AWG](#) starts playing the idle signal again to seed the high power [EDFA](#). The inset in figure 5.10b shows that there are intensity fluctuations: If there is even just a single pulse blocked by the fast pulse picker before a given pulse, that pulse creates a larger peak voltage in the photodiode than pulses that follow an unblocked pulse. This issue will be addressed and investigated further in section 6.3.

5.4 FREQUENCY UPCONVERSION

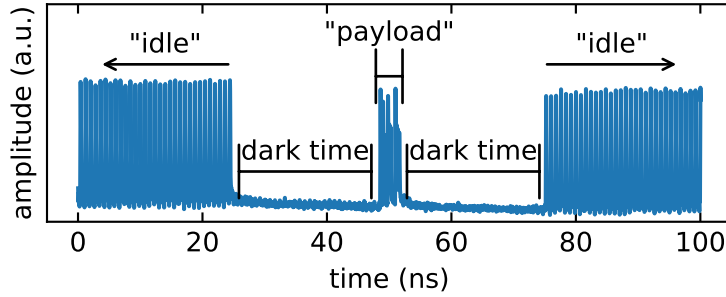
The fundamental 1572 nm light is converted to 393 nm by frequency doubling the light twice in two separate nonlinear crystals (panel D in figure 5.1, page 50). The first one is an MgO doped periodically-poled lithium niobate ([PPLN](#)) crystal¹², that is temperature stabilized at typically 83.7 °C by a temperature controller¹³. The second crystal is a 5 mm long periodically-poled potassium titanyl phosphate ([PPKTP](#)) crystal¹⁴ which is also mounted in an oven¹⁵ and temperature stabi-

¹² Covision MSHG1550-0.5-5

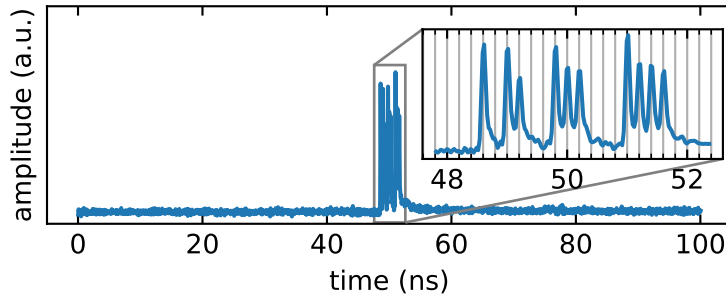
¹³ Thorlabs TC200

¹⁴ custom-made by Raicol Crystals Ltd.

¹⁵ Covision PV10



- (a) The [AWG](#) concatenates the idle signal, the payload and again the idle signal, separated by dark times. The idle signals are required to seed the high-power [EDFA](#). The length of the dark times is determined by two factors: The rise and fall times of the Pockels cell of 7 ns and the minimum allowed time of 35 ns between switching the cell on and off – i.e. between the start of the rise time and the start of the fall time. The pulse picker turns the [AWG](#) output into the optical signal that is shown here.



- (b) The optical signal from panel (a) is cropped by the Pockels cell. Only the payload remains and is directed to the ion. The inset shows the zoomed-in payload signal. Every grid line corresponds to the location of a pulse in the original 5 GHz pulse train. It shows that the pulse picker can switch individual pulses in arbitrary sequences. For the reason for the different pulse heights see section [6.3](#).

Figure 5.10: Single pulses mode. Figures adapted from [\[65\]](#).

lized at typically 48 °C by a temperature controller¹⁶. Since the doubling efficiency of the crystals scales with the square of the peak power, the measured extinction ratio of the BBO Pockels cell/PPKTP crystal system is 56 dB, i. e. almost the square of the Pockels cell extinction ratio.

At the current maximum average 1572 nm light power of about 2.8 W and at a repetition rate of 5 GHz (1.25 GHz, and therefore four times higher peak power) the crystals can output 0.77 W (1.18 W) of 786 nm light, which corresponds to a conversion efficiency of 28 % (42 %), and 25 mW (110 mW) of 393 nm light, which corresponds to a conversion efficiency of the second frequency doubling step of 3.2 % (9.3 %). The maximum total conversion efficiency (from 1572 nm to 393 nm) is 0.9 % (3.9 %). Measurements of the 786 nm and 393 nm light power and conversion efficiencies for four different repetition rates are presented in figure 5.11. The inset in panel (e) of that figure is a log-log graph of the same data. The graph, together with the line $y \propto x^4$ visualizes the expected fourth-power dependency of the 393 nm light power on the 1572 nm light power.

After the first SHG stage the remaining fundamental 1572 nm light is split off by a dichroic mirror and directed either into a beam dump or towards a frequency-resolved optical gating (FROG) setup in order to measure pulse characteristics like pulse width and bandwidth (see section 6.2). After the second SHG stage the remaining fundamental 786 nm light is also split off by a dichroic mirror and directed towards a 7 GHz photo detector¹⁷ in order to monitor the picked pulse sequences. Any remaining fundamental light in the doubled 393 nm beam path is further attenuated by a shortpass filter¹⁸ as seen in figure 5.12. Next, the light is coupled into a polarization-maintaining single-mode fiber¹⁹ and sent to the ion trap. After the 5 m long fiber, the pulse width is measured to be 2 ps. Finally, a collimator²⁰ equipped with a 250 mm lens²¹ focuses the laser beam on the ion. The collimator is mounted on a piezo-driven mirror mount²² which allows one to overlap the beam waist with the ion's wave packet. The mount's angular resolution is 0.7 μ rad, the optical path length between the mount and the ion is

¹⁶ Covention OC2

¹⁷ Alphas UPD-50-UP

¹⁸ Thorlabs FESH0700

¹⁹ Schäfter+Kirchhoff PMC-E-400Si-3.5-NA009-3-APC.EC-500-P

²⁰ Schäfter+Kirchhoff 60FC-L-4-M60-33

²¹ Schäfter+Kirchhoff 13M-S250-33-S

²² New Focus 8821-L

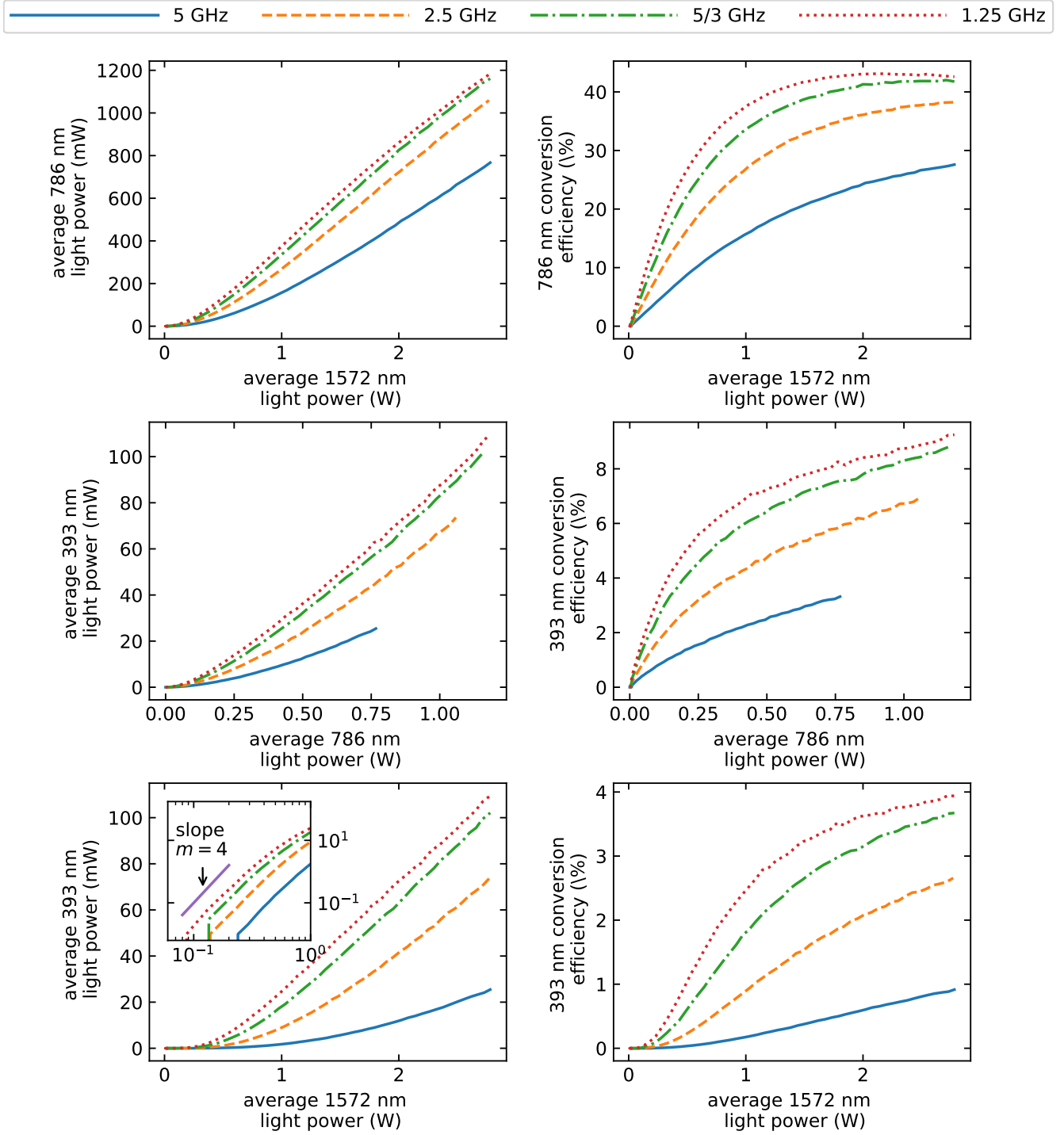


Figure 5.11: Measurement of 786 nm and 393 nm light power and conversion efficiencies of four different repetition rates as a function of fundamental 1572 nm and 786 nm light power. Parts of this figure were taken from [68].

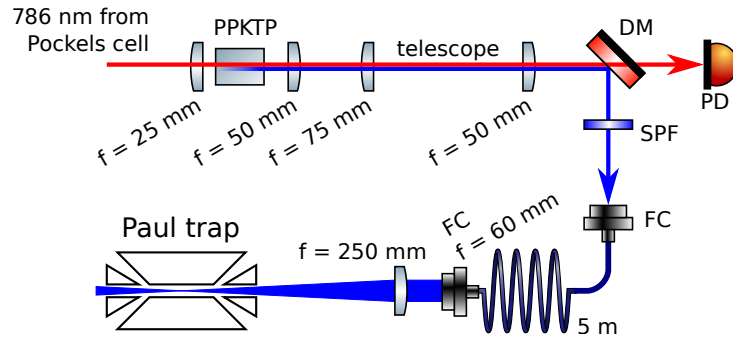


Figure 5.12: Schematic overview of the 393 nm optical setup. DM: dichroic mirror, FC: fiber coupler, PD: photo detector, PPKTP: periodically poled potassium titanyl phosphate, SPF: short pass filter (cut-off 700 nm).

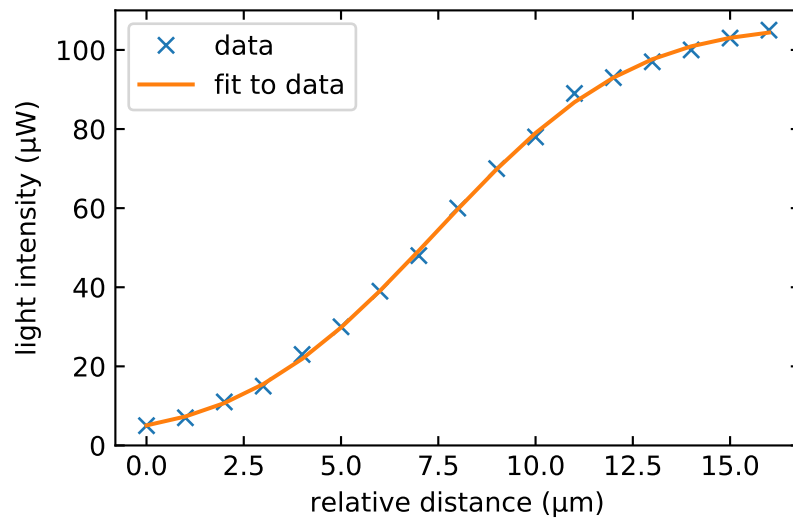


Figure 5.13: Knife edge measurement of the 393 nm beam waist at the location of the $^{40}\text{Ca}^+$ ion.

~ 30 cm, which allows one to position the beam waist with a radial resolution of $\sim 0.2\text{ }\mu\text{m}$. A knife-edge measurement determined the laser beam's waist to be $w_0 = 11.8(3)\text{ }\mu\text{m}$. Its data and a fit to that data are shown in figure 5.13.

LASER CHARACTERIZATION

Even though the laser system has been carefully designed to output pulses with the required properties derived in section 4.3.2, it has to be confirmed that these requirements are indeed fulfilled. Furthermore, the light may have additional properties that could affect the interaction with the $^{40}\text{Ca}^+$ ions and change the outcome of measurements. Characterizing the pulses before sending them on an ion will help to understand the results of any measurement taken.

This chapter studies pulse characteristics both averaged over several seconds long pulse trains and of individual pulses. Measurements include pulse width, spectral bandwidth and phase relations between pulses. Pulse trains are examined using optical spectrum analyzers (OSAs) in section 6.1 and a technique called frequency-resolved optical gating (FROG) in section 6.2. Section 6.3 measures the phase difference between consecutive pulses with a Michelson interferometer and looks into phase and intensity fluctuations due to pulse picking. Parts of section 6.3 have been published before in reference [65].

6.1 LIGHT SPECTRA

A number of different OSAs are available to measure the spectra of the laser pulses: The first OSA¹ can measure infrared (1572 nm) and red (786 nm) light, the second² can measure blue (393 nm) light. In principle, two additional OSAs are available to measure red³ and green⁴ (532 nm) but they are currently installed in the FROG setups. Figure 6.1 shows the spectrum of the fundamental infrared pulses, measured after the TOD compressor (see figure 5.1 on page 50). The measured center wavelength λ_c^{IR} is equal to the quadruple of the $4S_{1/2} \leftrightarrow 4P_{3/2}$ transition wavelength within the OSA's set resolution of 0.1 nm:

$$\lambda_c^{\text{IR}} = 1573.425 \text{ nm} \approx 1573.464 \text{ nm} = 4 \cdot 393.366 \text{ nm}.$$

The measured FWHM bandwidth of the spectrum is $\Delta\lambda^{\text{IR}} = 7.362 \text{ nm}$.

¹ Anritsu MS9740A, 0.6 μm to 1.75 μm

² Ocean Optics HR2000+, 350 nm to 483 nm

³ Ocean Optics HR2000+, 699 nm to 879 nm

⁴ Ocean Optics HR2000+, 464 nm to 585 nm

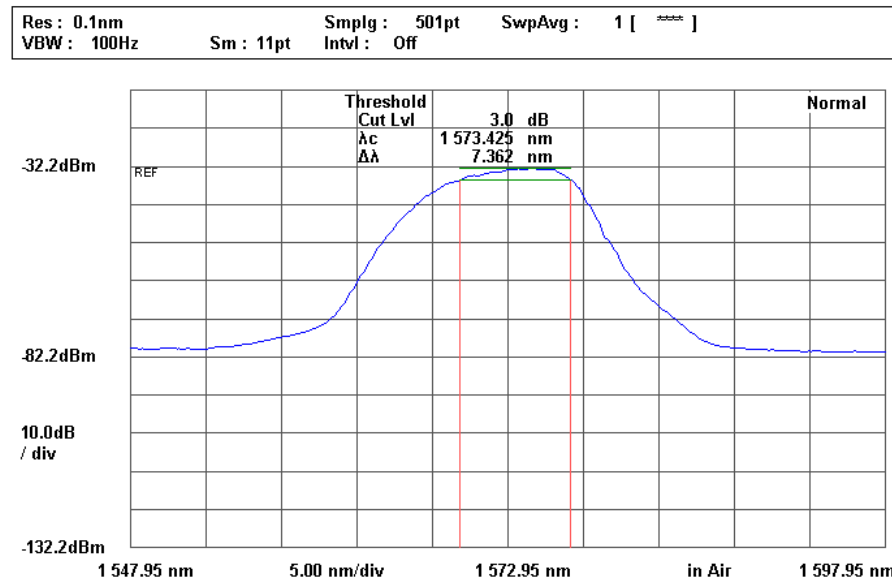


Figure 6.1: Optical spectrum of the high power **EDFA** output, measured after the **TOD** compressor. Instrument settings: resolution 0.1 nm, 501 samples, no averaging over multiple sweeps, video bandwidth 100 Hz, smoothing (i. e. averaging over neighboring samples) 11 points.

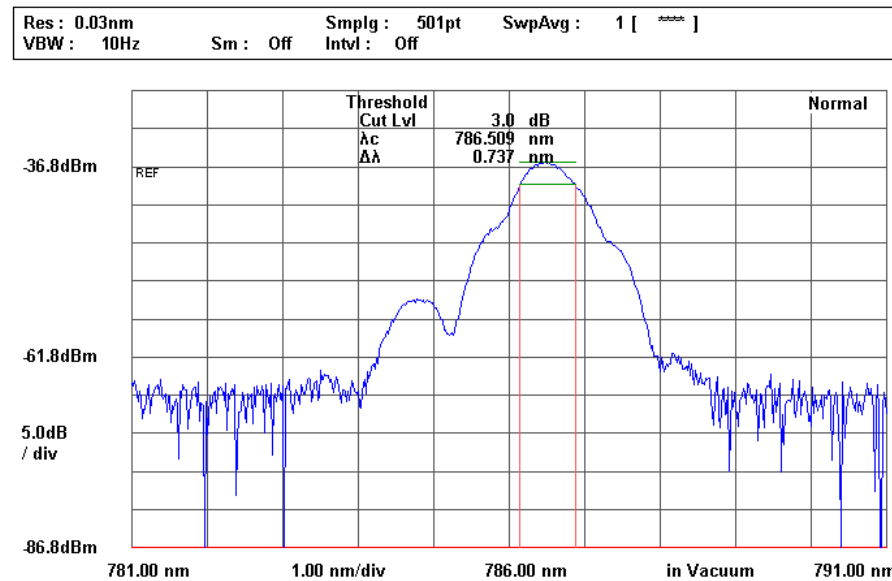


Figure 6.2: Optical spectrum of the 786 nm light, measured after the **BBO** Pockels cell. Instrument settings: resolution 0.03 nm, 501 samples, no averaging over multiple sweeps, video bandwidth 10 Hz, no smoothing.

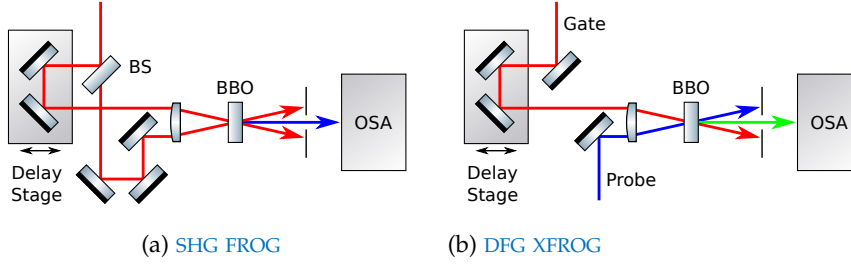


Figure 6.3: Schematic **FROG** and **XFROG** setups. BBO: barium borate crystal, BS: beam splitter, DFG: difference-frequency generation, OSA: optical spectrum analyzer, SHG: second harmonic generation.

Figure 6.2 shows the spectrum of the red 786 nm pulses, measured after the **BBO** Pockels cell. For the measurement of this spectrum, the **OSA** was accidentally configured to output wavelengths in vacuum. The center wavelength in air is therefore $786.509 \text{ nm} / 1.00028 = 786.293 \text{ nm}$, which is not within the **OSA**'s set resolution of 0.03 nm of the double of the $4S_{1/2} \leftrightarrow 4P_{3/2}$ transition wavelength, but still within 0.5 nm:

$$\lambda_c^{\text{red}} = 786.293 \text{ nm} \approx 786.732 \text{ nm} = 2 \cdot 393.366 \text{ nm}.$$

The measured **FWHM** bandwidth of the spectrum is $\Delta\lambda^{\text{red}} = 0.737 \text{ nm}$. The reason for the offset of the center wavelength is unclear. It could be either a calibration offset of the **OSA** or caused by the frequency doubling crystal. Its phase-matching bandwidth is a function of crystal temperature and can be adjusted by a few nm by tuning the temperature by several Kelvin.

6.2 FROG MEASUREMENTS

The **FROG** technique [58, 69, 70] is used for characterizing femtosecond pulses and can determine the pulses' full time- and wavelength-dependent intensity and phase. This information can be used to determine and monitor the pulse width and chirp, and minimize both by adjusting the **TOD** compressor. A **FROG** device measures the spectrum of a signal pulse as a function of the delay between a probe and a gate pulse. The signal pulse is generated by letting the probe and gate pulse interact using an instantaneous nonlinear-optical effect [69]. Most commonly, the pulses are overlapped in a nonlinear crystal using **SHG** [71] and probe and gate pulses origin from the same input

pulse as shown in figure 6.3a. Alternatively, a fully characterized reference pulse can be used as gate pulse to characterize an unknown probe pulse [72], which is shown in figure 6.3b. This is known as cross-correlation FROG (XFROG) and also allows characterizing pulses unsuitable for SHG by using e.g. DFG instead [73].

In this thesis, two devices – one for FROG⁵ and one for XFROG⁶ – were used to characterize pulses at 1572 nm, 786 nm and 393 nm. Both devices use a BBO crystal for the nonlinear-optical effect – the FROG device for SHG, the XFROG device for DFG using infrared (1572 nm) pulses as gate pulses and blue (393 nm) pulses as probe. For measuring infrared pulses, fundamental light not converted in the first SHG stage is coupled into the FROG device. In order to measure red (786 nm) pulses, one must exchange the installed OSA for the one sensitive to blue light, align the red pulses with the device and adjust the tilt of the crystal. Blue pulses can be characterized by sending those as well as the remaining infrared fundamental light to the XFROG device.

Aligning the devices requires overlapping the gate and probe pulses both spatially and temporally within the BBO crystal. The signal pulse then has to be coupled into the OSA. For the FROG device, temporal alignment was done by the manufacturer and spatial alignment is assisted by two iris diaphragms separated by ~ 40 cm. If spatial alignment fails despite using the diaphragms, the BBO crystal can be replaced by pinholes of decreasing diameter (e.g. 150 μm , 100 μm , 50 μm) and coupling both probe and gate beams through the pinholes' apertures. Aligning the XFROG device is much more complicated: Both temporal and spatial alignment have to be done manually and simultaneously before a signal pulse can be detected. To get at least some spatial overlap the pinhole technique above can be used as well. For temporal alignment either one of the input pulses has to be passed through a manual delay stage, in this case the blue probe pulses were chosen. Working with a repetition rate of 5 GHz is both a blessing and a curse: On the one hand the high repetition rate causes two consecutive pulses to be $c/5 \text{ GHz} \approx 6$ cm apart (with c the speed of light). This distance can be completely covered by manual delay stages, ensuring temporal overlap at least somewhere between the ends of such translation stage. On the other hand the high repetition rate causes the pulses' peak powers to be lower than for lower repetition rates, which decreases the efficiency of the nonlinear process. In the

⁵ MesaPhotonics FROG Scan Ultra

⁶ MesaPhotonics X-FROG Scan

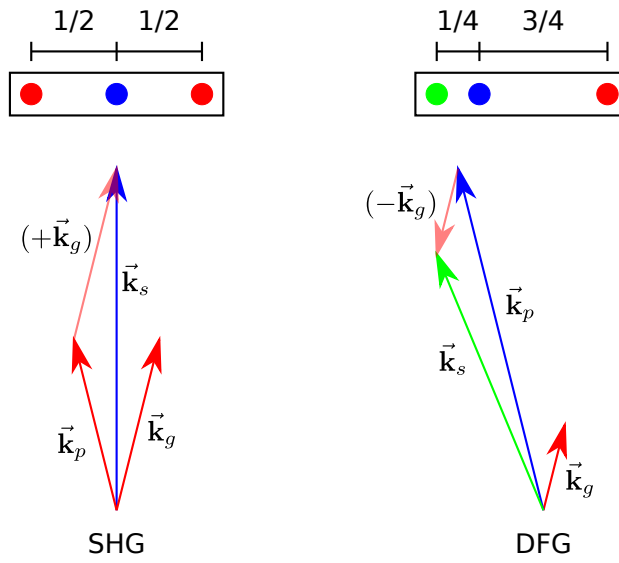


Figure 6.4: Wave vector diagrams of non-collinear **SHG** (left) and **DFG** (right).

For the case relevant to this thesis, i. e. $|\vec{k}_p| = 4 \cdot |\vec{k}_g|$, the three beams would have a relative spatial distribution as indicated in the frames above if viewed on e. g. a piece of paper. \vec{k}_g : wave vector of the gate pulse, \vec{k}_p : wave vector of the probe pulse, \vec{k}_s : wave vector of the signal pulse.

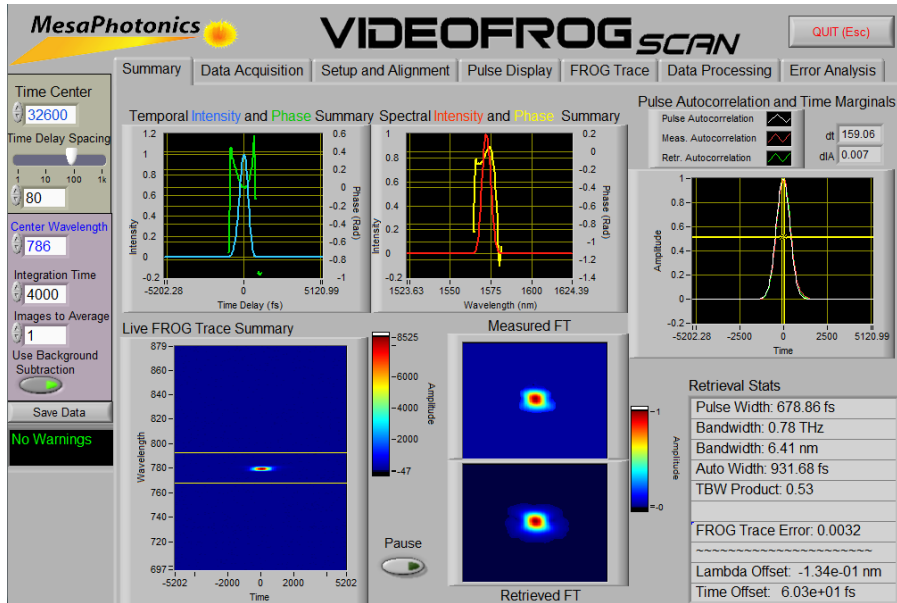
laboratory, it was necessary to use a lock-in amplifier⁷ to detect the first trace of a signal. A photodiode sensitive to light at 532 nm is placed where the signal pulses are expected to be (see figure 6.4) and connected to the lock-in amplifiers input. Its output is configured to output a 20 Hz AC voltage of 2 V_{pp} amplitude and connected to the XFROG device's servo motor, which then moves the delay stage mirror back and forth. Since temporal overlap can occur both on the way back and forth, and therefore twice per AC period, the amplifier has to be set up to detect a signal at the second harmonic frequency of the output signal. This process eventually leads to a detectable signal that can then be maximized by adjusting both the temporal and spatial overlap.

The FROG measurement of infrared pulses presented in figure 6.5a shows that the pulses have a pulse width of 679 fs and a bandwidth of 0.78 THz $\hat{=}$ 6.41 nm, which is roughly in agreement with the value measured with the OSA in section 6.1. The pulses' time-bandwidth product of 0.53 is only 20 % larger than the theoretical limit for Gaussian-shaped pulses of ≈ 0.44 [74]. The temporal (spectral) phase (see equation (2.56)) stays within 0.4 rad (0.2 rad) of the reference phase at the intensity maximum. The deviations larger than these limits at both ends of the phase plots can be disregarded as these stem from measurement errors due to the low intensities at the ends. Both phases can therefore be considered constant which is a property of unchirped pulses [58]. The shown measured and retrieved FROG traces are respectively the input and output of the FROG retrieval algorithm. Their similarity shows that the algorithm has successfully inverted the measured trace and extracted the pulses' intensity and phase [75]. The measurement and algorithm run sufficiently fast – the “Retrieval Stats” update several times per second – to allow one to manually adjust the TOD compressor (see section 5.3 on page 56) in order to minimize the pulse width, which ensures maximum efficiency in the SHG stages.

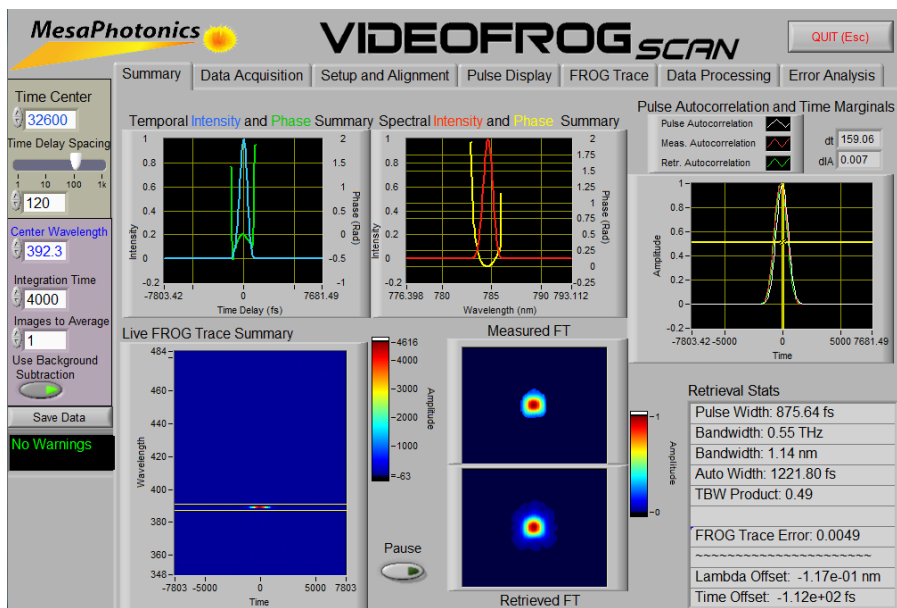
The characterization of red pulses shown in figure 6.5b yields a very similar result: Measured and retrieved FROG traces are close to identical, temporal and spectral phases are within 0.5 rad and 0.3 rad of the reference phase, the pulse width is 876 fs, the bandwidth 0.55 THz $\hat{=}$ 1.14 nm and the time-bandwidth product of 0.49 is 11 % larger than the theoretical limit.

In contrast to the infrared and red pulses, the characterization of blue pulses paints a different picture: It can be seen in figure 6.5c that,

⁷ SRS SR830

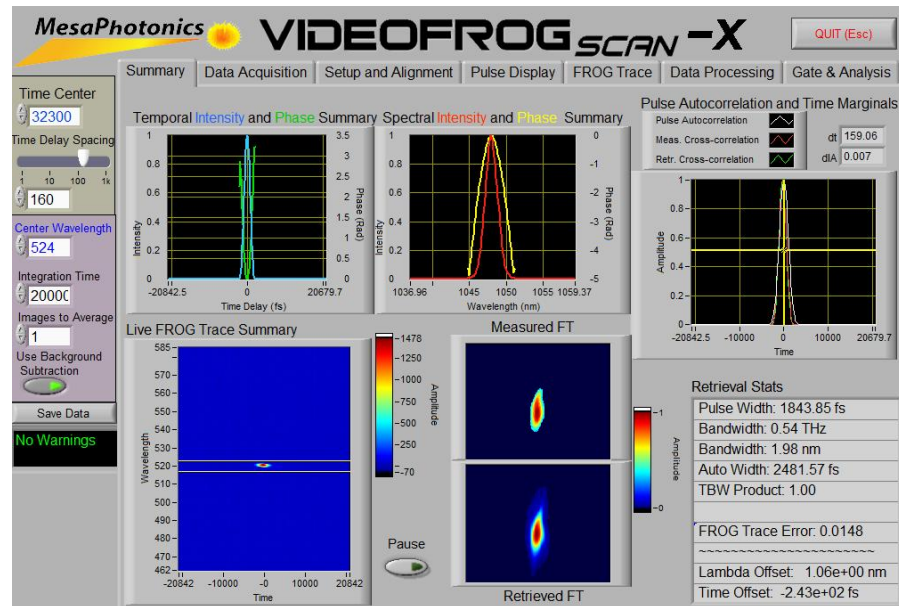


(a) Screenshot of an IR (1572 nm) pulse FROG measurement



(b) Screenshot of a red (786 nm) pulse FROG measurement

Figure 6.5: Part I, screenshots of FROG measurements of pulses of different wavelengths, continued on the next page.



(c) Screenshot of a blue (393 nm) pulse XFROG measurement. The tick labels of the wavelength axis of the “Spectral Intensity and Phase Summary” plot are incorrect due to a programming error. The intensity peak should be centered around 393 nm instead of 1048 nm and the bandwidth should read 0.28 nm. According to the manufacturer all other values are calculated in differential frequency space and this has no effect on the results.

Figure 6.5: Part II, screenshots of FROG measurements of pulses of different wavelengths. The controls on the left edge of the screenshots allow the user to change measurement parameter. The first two plots in the screenshots give an overview of the pulse intensity and phase as a function of time and wavelength, respectively. Below that, the *Live FROG Trace Summary* shows a 2D plot of the latest intensity measurement as a function of both time and wavelength. The yellow lines mark the region of interest of the pulse retrieval algorithm. To its right, the region of interest is repeated in a larger scale. The 2D plot labeled *Measured FT* shows the input of the retrieval algorithm, the one labeled *Retrieved FT* its output. The similarity of the measured and the retrieved FT is a sign that the retrieval algorithm has succeeded. In the lower right corner of the screenshots, the *Retrieval Stats* summarize important pulse properties such as pulse width and bandwidth. FT: FROG trace, TBW: time-bandwidth.

while the algorithm is still able to invert the measured FROG trace as is evident by the similarity in measured and retrieved traces, the pulse width of 1.84 ps with a bandwidth of 0.54 THz $\hat{=}$ 0.28 nm result in a time-bandwidth product of 1.00. This means the pulses are now chirped. Also, both temporal and spectral phase have now taken a quadratic form which is associated with a linear chirp [58].

6.3 PULSE SWITCHING CHARACTERISTICS

Our pulse picking scheme – described in detail in section 5.3 – involves blocking the pulses with the fast pulse picker during the rise and fall time of the Pockels cell for typically 25 ns. This results in an equally long dark time of the subsequent amplifiers, which can potentially influence the gain of the amplifiers: During the dark time, the energy input into the gain medium does not change, but no energy is taken out of it. This in turn can change pulse characteristics such as pulse intensity, which has already been shown in the inset of figure 5.10b (page 63). Since the fast phase gate scheme assumes that every optical pulse acts as a perfect π -pulse, intensity fluctuations could decrease the gates' fidelity. In order to check the performance of the pulse picking equipment and examine the influence of a dark time on the pulses during the first nanoseconds after such dark time, pulse intensities were measured directly using a fast photodiode and relative phases were measured interferometrically, and the results described in this section.

Phase shifts of the pulses were characterized by interfering the pulses in a Michelson interferometer (see figure 6.6a). At the beam splitter the input pulse train is split into two copies, one of which is temporally delayed by one pulse period τ_{pulse} with respect to the other before being recombined. In this way, every pulse i interferes with its successive pulse $i + 1$ and the total phase difference $\Delta\Phi_i$ of the two pulses at the output of the interferometer is a function of the phase difference $\Delta\phi_i$ of pulses i and $i + 1$, and the path length difference $\Delta x = 2x_2 - 2x_1 \approx c \cdot \tau_{\text{pulse}}$:

$$\Delta\Phi_i = \Delta\phi_i + k \cdot \Delta x, \quad (6.1)$$

with x_1 (x_2) the length of interferometer arm 1 (2), c the speed of light and k the length of the wave vector. The interference pulses are detected on a fast photodiode and their pulse intensity areas, which are functions of $\Delta\Phi_i$, are extracted by integrating the photodiode's signal over the pulse length.

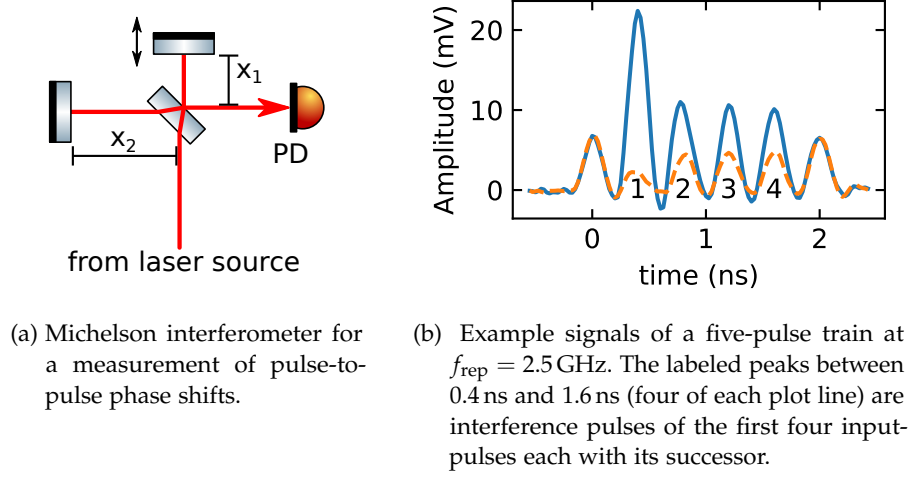


Figure 6.6: Image adapted from [68]

Δx can be tuned manually by moving one of the retro-reflecting mirrors that is fixed on a manual translation stage, but Δx can not be changed deterministically on a sub-wavelength scale which would have allowed to keep track of the changes in $\Delta\Phi_i$ due to changes in Δx . Nevertheless, its fluctuations were found to be much smaller than the light's wavelength and Δx can be considered constant on time scales of the measurements of about 100 ms. For each measurement, Δx is therefore randomly chosen and the measurement repeated for different Δx . Accordingly, the interference-pulse intensity areas of each measurement are both random but also correlated in size since Δx is random but equal for all pulses in a given measurement, and if the pulse intensity areas of two interference pulses i and j are different, there is also a change $\delta\phi_{i,j} = \Delta\phi_i - \Delta\phi_j$ in their phase differences.

In order to determine $\delta\phi_{i,j}$ a five-pulse pulse train is repeatedly sent into the interferometer at a rate of 1 kHz and averaged over 100 consecutive trains. The interference-pulse intensity areas are measured for different and random Δx by moving the translation stage back and forth on the order of $5 \mu\text{m}$ between two 100 pulse trains-long measurements. Figure 6.6b shows two example interference signals, taken at 2.5 GHz. For every measurement at different Δx the pulse intensity areas of two interference pulses are plotted against each other and the data is presented in figure 6.7. Every abscissa is the intensity area of interference pulse 4; the ordinates are the intensity areas of interference pulses 1 through 3, respectively.

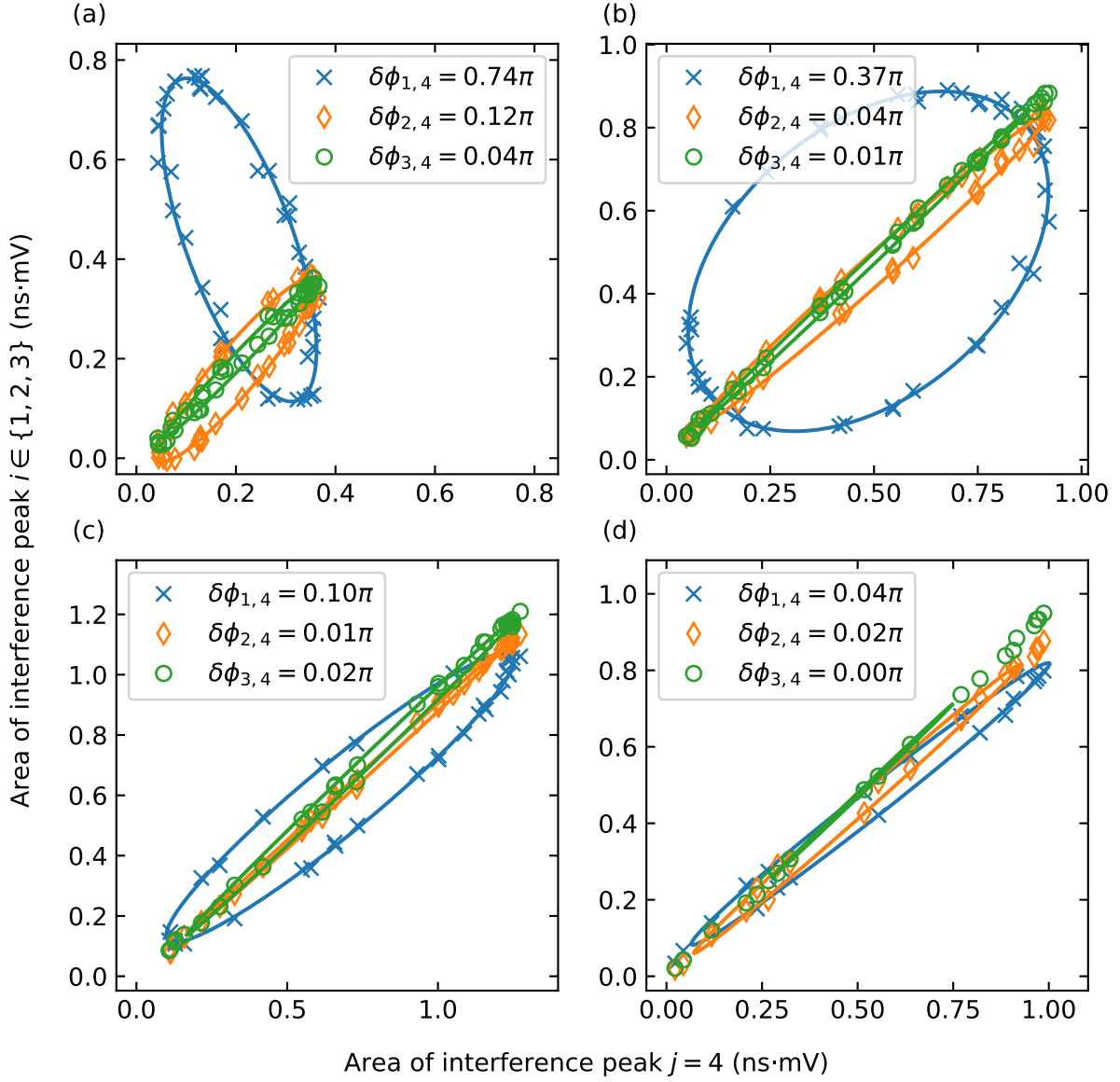


Figure 6.7: Interferometric phase measurements: Intensity areas of the first (blue crosses), second (yellow diamonds) and third (green circles) interference peak plotted against the intensity area of the fourth interference peak. The solid curves are a fit of the ellipse $x(\Delta\phi) = c * \sin(\Delta\phi) + x_0$, $y(\Delta\phi) = c * \sin(\Delta\phi + \delta\phi_{i,j}) + y_0$ to the data, which allows us to extract $\delta\phi_{i,j}$ up to a sign, since for $\delta\phi_{i,j} = \Phi$ and $\delta\phi_{i,j} = -\Phi$ the ellipses are congruent. The repetition rate is 5 GHz (a), 2.5 GHz (b), 5/3 GHz (c) and 1.25 GHz (d), respectively. For higher repetition rates, the phase difference between the first and second pulses is larger than the phase difference between later pulses. At lower repetition rates, the phase difference between any two consecutive pulses is equal within 1 % of 2π . Image adapted from [68].

The data points fall on a straight line at a 45° angle, if $\delta\phi_{i,j}$ between the two interference pulses is zero or an integer multiple of 2π , and at a -45° angle if $\delta\phi_{i,j} = (2n + 1)\pi, n \in \mathbb{Z}$. In general, for any other value of $\delta\phi_{i,j}$ the data points are located on an ellipse. This allows us to extract $\delta\phi_{i,j}$ by fitting an ellipse to the data.

A dependence of $\delta\phi_{i,j}$ on the length of the pulse period $\tau_{\text{pulse}} = 1/f_{\text{rep}}$ can be seen if there was a long (here: 12 ns) dark time before the first pulse: For the maximum repetition rate of $f_{\text{rep}} = 5$ GHz one finds that between the first (second) and fourth interference peak (pulses 1&2 (2&3) and 4&5, respectively) $\delta\phi_{1,4} = 0.74$ rad ($\delta\phi_{2,4} = 0.12$ rad). For later interference peaks ($i \geq 3$) $\delta\phi_{i,4}$ is vanishingly small. As a trend one can observe that for larger τ_{pulse} , $\delta\phi_{i,j}$ becomes smaller and is vanishing for $\tau_{\text{pulse}} \geq 800$ ps = $1/1.25$ GHz.

In addition to the phase shift, repetition rate-dependent deviations of the pulse intensity of the first pulses after the dark time were observed. Figure 6.8 shows the pulse intensity areas of the pulses during the first 2 ns after the dark time. In the case of 5 GHz repetition rate it can be observed that all pulses from the second onward are weaker by a factor of about 3 with respect to the first pulse. At 2.5 GHz repetition rate, the intensity of the second pulse decreases by about 10 % with respect to the first. At the other repetition rates this effect can not be observed. For all repetition rates an increase in pulse intensity of about 10 % is observed for the shown time of 2 ns of pulses after the possible initial decrease.

Both the phase shift and the change in pulse intensity area will be problematic for experiments using coherent manipulations of the qubit. Since for the two-ion phase gate every pulse needs to act as a π -pulse, the pulse intensity area needs to be constant, but due to the way it is planned to create the counter-propagating pulse pairs, the phase shift does not: It is intended to generate the two pulses of every required π -pulse pair by splitting a larger-area pulse. Therefore, every pulse pair will consist of identical copies and as long as the intensity is stable and has the right magnitude, the two pulses will add up to a 2π -rotation of the Bloch vector around the same axis regardless of phase difference with respect to other pulse pairs. For this reason only the intensity changes should pose an issue for the phase gate, the phase shifts should not.

By the time of this writing it was confirmed that both effects are caused by a semiconductor optical amplifier (SOA2 in figure 5.1 on page 50) which serves as a preamplifier to the high power EDFA and

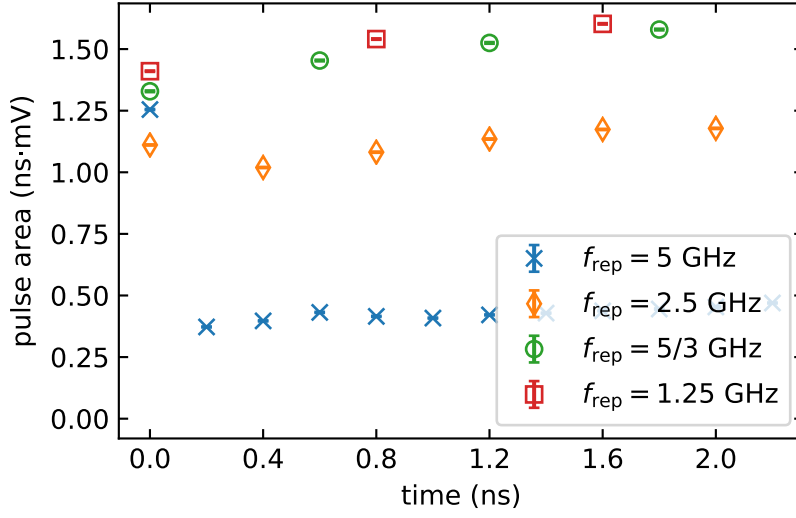


Figure 6.8: Pulse intensity areas of pulses during the first 2 ns after a 12 ns dark time at repetition rates from 1.25 GHz to 5 GHz. Time axis relative to first pulse. Data points are the average of 1000 measurements, error bars are smaller than data point symbols. Average high power EDFA output power for this measurement was $\approx 1.6 \text{ W}$. This figure was taken from [68].

are due to the finite carrier lifetime of the SOA of 500 ps. This causes the dynamical behavior of the SOA to depend on the input signal of the past $\sim 500 \text{ ps}$ [76] and is known as the “pattern effect” [77]. Currently, the SOA is being replaced by another fiber-based preamplifier.

After the description of the experimental setup in the next chapter, the results of this section will be confirmed by measurements with a $^{40}\text{Ca}^+$ ion in chapter 8.

EXPERIMENTAL SETUP

The experiments of this thesis were conducted in a new trap assembly which was set up in laboratory 2 of the Institute for Quantum Optics and Quantum Information (IQOQI). Two projects were hosted in this laboratory which shared the ion trap, the experiment control electronics and software, the CW lasers for ion manipulation as well as the frequency comb. These items have been described in detail in the thesis of Michael Guggemos [40]. Therefore, this chapter will summarize the description of these shared elements and add details where necessary or relevant to this thesis.

7.1 THE ION TRAP

The ion trap used for confining ions is a linear Paul trap [78]. The pseudo-potential confining the ion in the radial direction is created by four blade-shaped electrodes positioned symmetrically around the trapping site at an angle of 45° from the vertical as can be seen in figure 7.1. The ion-blade electrode distance is about $555\text{ }\mu\text{m}$. A radio frequency signal of 32 MHz is applied to one pair of opposite blades while the other blade pair is kept at a voltage of 1.5 V above ground by a battery, in order to lift the degeneracy of the radial frequencies. Two more electrodes are located on each side of the trapping site in the axial direction. These *endcap electrodes* are kept at a voltage of typically $\sim 500\text{ V}$ to confine the ion axially. They are separated by 4.5 mm and feature holes of 0.5 mm diameter in order to allow for optical access along the trap axis. Another two pairs of electrodes are used to compensate electric stray fields in order to keep the ion crystal in the center of the RF field. One pair of these *compensation electrodes* is located directly above the trapping site, the other at 90° to the side.

The geometry of the new ion trap is the same as in previous trap assemblies of the group which are described e.g. in [45, 79]. The measured axial oscillation frequency of the ion crystal is 819 kHz at an endcap electrode voltage of 400 V.

Two ablation targets for loading ions are mounted above the trap. One is an alloy containing calcium, the other is made from aluminum

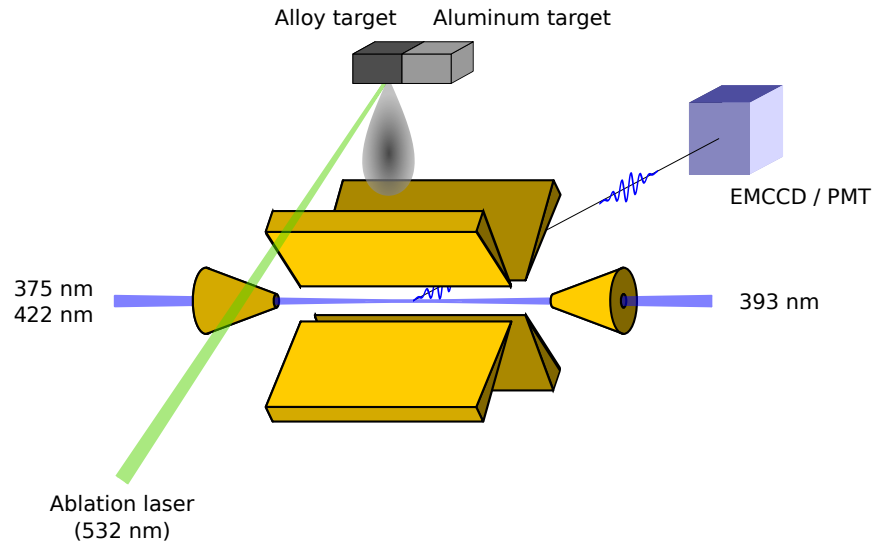


Figure 7.1: Schematic view of the Paul trap. PMT: photomultiplier tube, EMCCD: electron-multiplying charge-coupled device. This figure was taken from [41].

and is used in the second project in this laboratory for loading $^{27}\text{Al}^+$ for quantum logic spectroscopy. An ablation laser (see section 7.2) then allows for convenient loading of calcium and aluminum ions by photoionization of ablated atoms.

Magnetic field coils attached to the outside of the vacuum chamber create a magnetic quantization field of 4 G at the trap site. The magnetic field vector at this point is chosen to be parallel to the trap axis.

Optical access to the trap site is provided along three axes shown in figure 7.2: One axis lies in the horizontal plane and is orthogonal to the trap axis. It is used to detect fluorescence and to image the ion crystal, and to send light at 729 nm to it. The second axis is parallel to the trap axis – and therefore also to the quantization field – and leads through the holes in the endcap electrodes. It is used to send the photo ionization lasers or the 393 nm pulses to the trapping site / ion crystal. The last axis lies in a plane spanned by the trap axis and the vertical at an angle of 45° to the trap axis. Four different lasers of the wavelengths 397 nm, 729 nm, 854 nm and 866 nm are sent to the crystal along this axis.

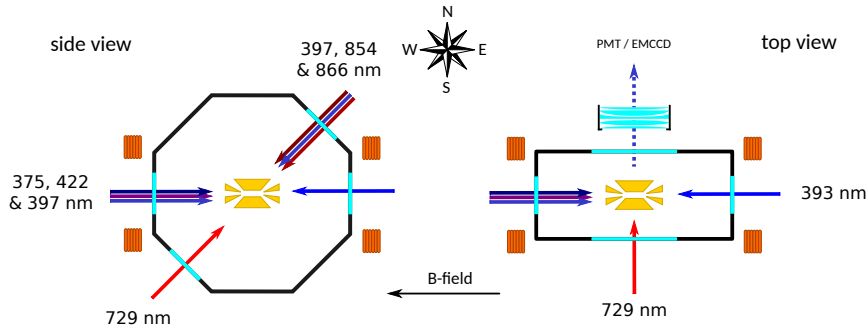


Figure 7.2: Schematic top and side view of optical access to the ion crystal. Laser beam directions are shown as arrows and given with their wavelengths. Magnetic field coils, which create the quantization field, are indicated in orange. The compass rose indicates the orientation of the setup in the laboratory. Image modified from [40].

Fluorescence from the ion crystal is collected by a 5-lens objective¹ with an effective focal length of 66.8 mm and a pupil diameter of 34 mm [45]. It is then guided through a variable slit² to block stray light and through a band pass filter³ which only allows light from 381 nm to 399 nm to pass. The fluorescence is then split up and detected by both a photomultiplier tube (PMT)⁴ and an electron-multiplying charge-coupled device (EMCCD)⁵.

7.2 LASER SYSTEMS AND OPTICAL SETUP

Lasers operating at different wavelengths are needed in order to ablate neutral calcium atoms, ionize them to $^{40}\text{Ca}^+$ ions, cool the trapped ions and ion crystal, and initialize, manipulate and read out the ion qubits. Table 7.1 gives an overview of the present laser wavelengths and purposes. All external cavity diode lasers (ECDLs) – which are described in the following paragraphs – are locked to a wavelength meter (WLM)⁶ with a feedback bandwidth of ~ 40 Hz. The WLM successively measures each laser's frequency with a precision

¹ custom made by Silloptics

² Owis Spalt 40

³ Semrock SEM-FF01-390/18-25

⁴ Sens-Tech P25PC

⁵ Andor iXon DV885JCs-VP

⁶ HighFinesse WS U/2

λ (nm)	POL.	ANGLE TO TRAP AXIS ($^\circ$)	PURPOSE
375	lin.	0	photo ionization
393	circ.	0	fast phase gate
397	lin.	45	Doppler cooling & state detection
397	circ.	0	optical pumping (state initialization)
422	lin.	0	photo ionization
532	lin.		laser ablation
729	lin.	0, 45, 90	spectroscopy
854	lin.	45	repumping $3D_{5/2}$ state
866	lin.	45	repumping $3D_{3/2}$ state

Table 7.1: Overview of the employed laser wavelengths and their purposes.
 λ : wavelength.

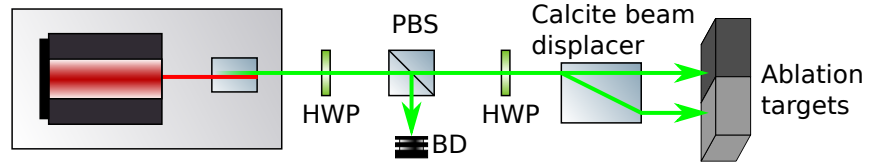


Figure 7.3: Schematic setup of the ablation laser. BD: beam dump, HWP: half-wave plate, PBS: polarizing beam splitter.

of 2 MHz and feeds back a voltage between -10 V to 10 V which is added to the drive voltage of a piezo controlling the length of the laser's external cavity. The setpoint of each laser's control loop can be adjusted either manually or by the experiment control software (see section 7.3.2). The WLM is automatically calibrated every 5 min with light from a 729 nm laser whose absolute frequency is known with a precision of about 1 Hz.

The following paragraphs describe the lasers needed to create and trap $^{40}\text{Ca}^+$ ions, to cool and prepare them in an initial state, and to manipulate the internal and external degrees of freedom.

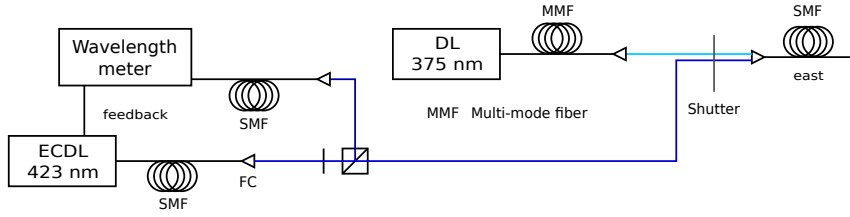


Figure 7.4: Schematic setup of the photo ionization lasers. Image source: [40]

ABLATION LASER The ablation laser⁷ is a frequency-doubled, pulsed laser operating at a fundamental wavelength of 1064 nm. Its maximum repetition rate is 100 Hz but a single pulse is usually triggered manually via a TTL signal about once every minute during the ion loading process. The emitted pulses have a pulse energy of up to 400 μ J and a pulse width of 2 ns. A schematic of the beam path is shown in figure 7.3. The first of two half-wave plates allows for attenuating the ablation pulses via a PBS and a beam dump. The second half-wave plate allows for selecting from which target to ablate from by switching between two polarization-dependent paths through a calcite beam displacer⁸.

PHOTOIONIZATION LASERS The photoionization scheme employed in this experiment is a two-step process [45] requiring two lasers. In the first step an ECDL⁹ emitting light of a wavelength of 422 nm excites neutral calcium atoms to the first excited level. Next, a free-running diode laser¹⁰ at 375 nm excites it further into the continuum, photoionizing the atom. The two laser beams are overlapped on a dichroic mirror and can be blocked by a TTL-controlled shutter as shown in figure 7.4. The beams are then coupled into a single-mode (SM)-fiber and sent to the trap.

COOLING AND DETECTION LASER A 397 nm laser redshifted from the $4S_{1/2} \leftrightarrow 4P_{1/2}$ transition by a few MHz is used for both Doppler cooling and state detection. It is a frequency-doubled ECDL¹¹ with a fundamental wavelength of 794 nm. Part of the fundamental light is sent to the WLM while the rest is first amplified in a tapered amplifier

⁷ Coherent Flare 532

⁸ Thorlabs BD40

⁹ Toptica DL pro

¹⁰ Toptica iBeam smart

¹¹ Toptica TA-SHG pro

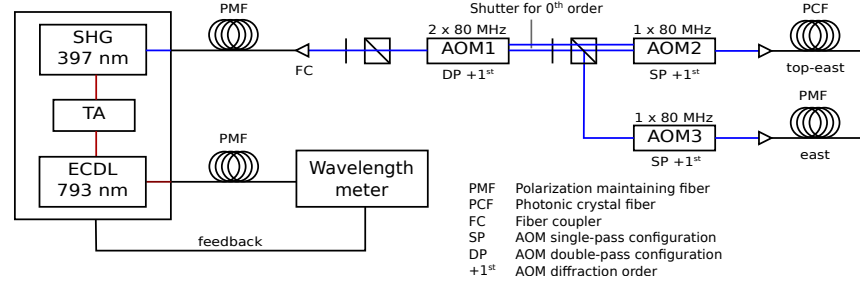


Figure 7.5: Schematic setup of the 397 nm laser Image source: [40]

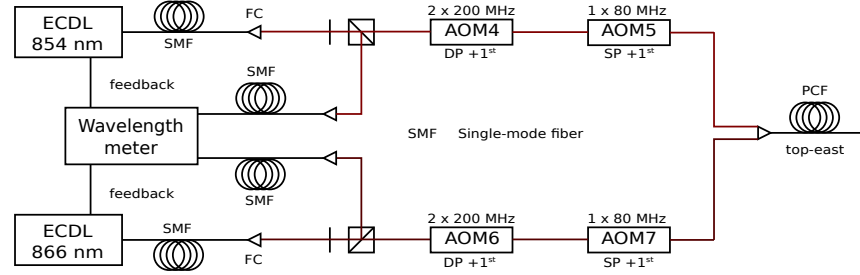


Figure 7.6: Schematic setup of the repumping lasers. Image source: [40]

(TA) and then frequency doubled by a nonlinear crystal located in a resonant cavity in bow-tie configuration. Figure 7.5 shows a scheme of the doubled light's beam path. An acousto-optic modulator (AOM) in double-pass configuration adds 160 MHz to the light in the 1st order diffraction. A second AOM shifts the light by another 80 MHz, it is used to further suppress unwanted light when the AOMs are switched off. Finally, a dichroic mirror overlaps the light with 854 nm and 866 nm light (see next paragraph) and coupled together into a photonic-crystal fiber (PCF) which directs the light to the ion trap. Unshifted (0th order) light from the double-pass AOM is also coupled into the fiber but can be blocked by a mechanical shutter. This allows one to illuminate the ions with 160 MHz red detuned light which enhances (re)crystallization of a (molten) ion crystal.

PUMPING LASERS Two lasers resonant with the $3D_{3/2} \leftrightarrow 4P_{1/2}$ transition (866 nm) and the $3D_{5/2} \leftrightarrow 4P_{3/2}$ transition (854 nm), respectively, are used to pump out the two D states. The 854 nm laser is used primarily to initialize the ion in the $4S_{1/2}$ state, while the 866 nm laser is also needed during Doppler cooling and state detection.

Both lasers are ECDLs¹² and their light is controlled in identically set up beam paths shown in figure 7.6. One AOM in double-pass configuration and another in single-pass configuration shift the light by 400 MHz + 80 MHz in order to suppress unwanted light when the AOMs are switched off. Next, both light beams are first overlapped in a PBS and then overlapped with the 397 nm light by the dichroic mirror.

LASER FOR QUBIT MANIPULATION A 729 nm laser resonant to the $4S_{1/2} \leftrightarrow 3D_{5/2}$ quadrupole transition is used to coherently manipulate the involved ion states. The laser is located in laboratory 1 of the IQOQI and the laser itself as well as the stabilization technique is described in detail in references [45, 80]. In lab 1, about 20 mW of light is coupled into a polarization maintaining (PM)-fiber and guided to our laboratory. Here, an AOM used for fiber noise cancellation shifts the light by 80 MHz as indicated in figure 7.7. After the AOM, a wedge reflects 4% of the light back into the fiber. This part is used in lab 1 to create the signal needed for fiber noise cancellation. The remaining light is used to seed a TA¹³ which outputs about 600 mW of light. A second AOM then shifts the light back by -80 MHz. It can optionally be used for light intensity stabilization. At this point a few μ W are split off and sent to the WLM. The main part of the light is again frequency shifted between 190 MHz to 270 MHz by an AOM in double-pass configuration. Finally, the light is shifted by 80 MHz by either one of two AOMs and coupled into two fibers. The AOMs are set up such that the 0th order of diffraction of the first AOM is coupled into the second, and at any given time only one of them is active. In this way, the light reaches the ion via one of the two fibers and therefore from one of two directions.

7.3 EXPERIMENTAL CONTROL

Controlling a quantum optics experiment on time scales of typically tens of nanoseconds – in case of this thesis' project even tens of picoseconds – requires dedicated and specialized hardware and automation software. Anything operating on the latter timescale is controlled by the AWG and delay generator described in section 5.3. Devices that need to be controlled on the former timescale are governed by home-made electronics described in the next subsection. The software used

¹² 2x Toptica DL pro

¹³ Toptica TA 100

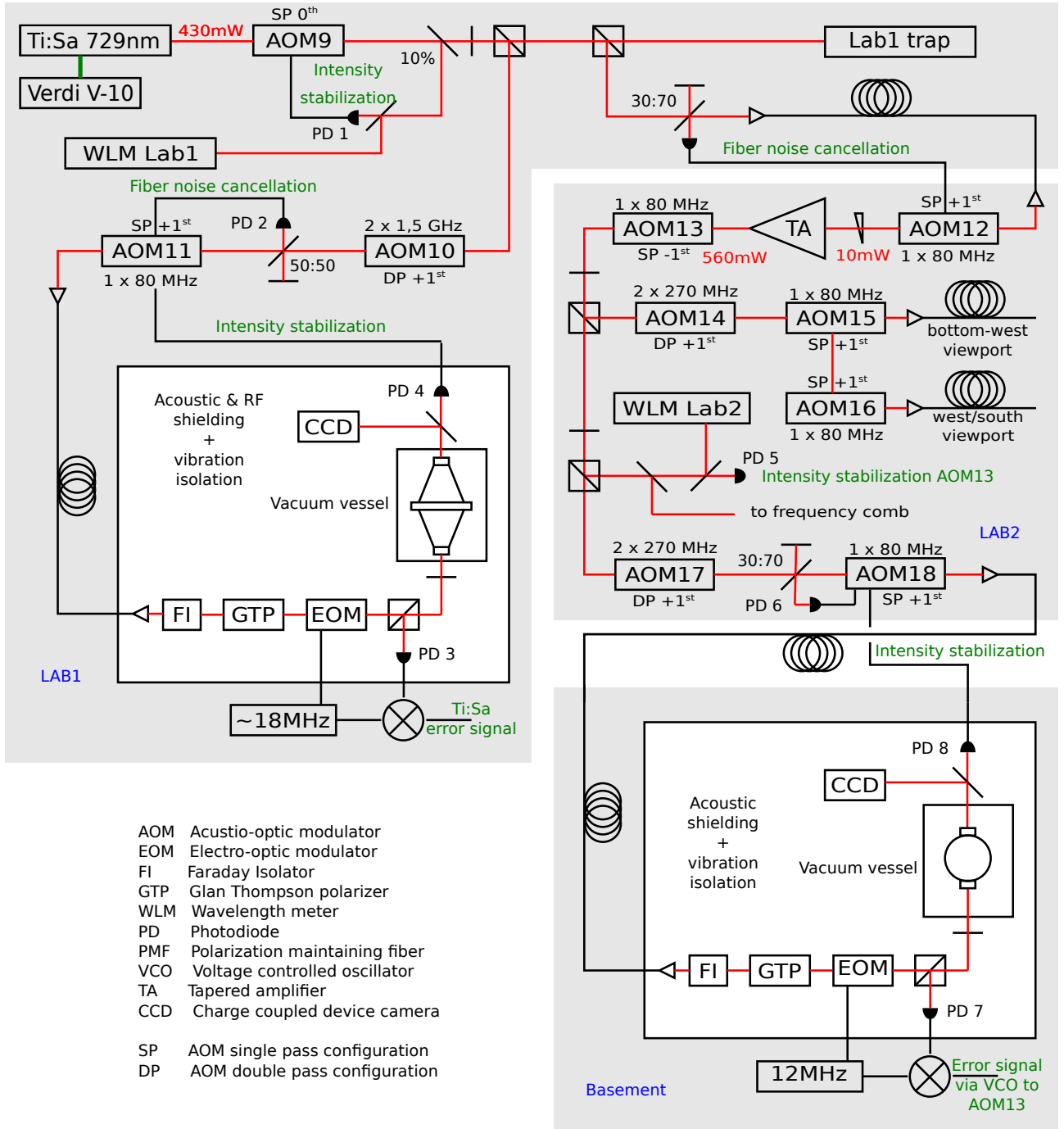


Figure 7.7: Schematic setup of the 729 nm laser. Image source: [40]

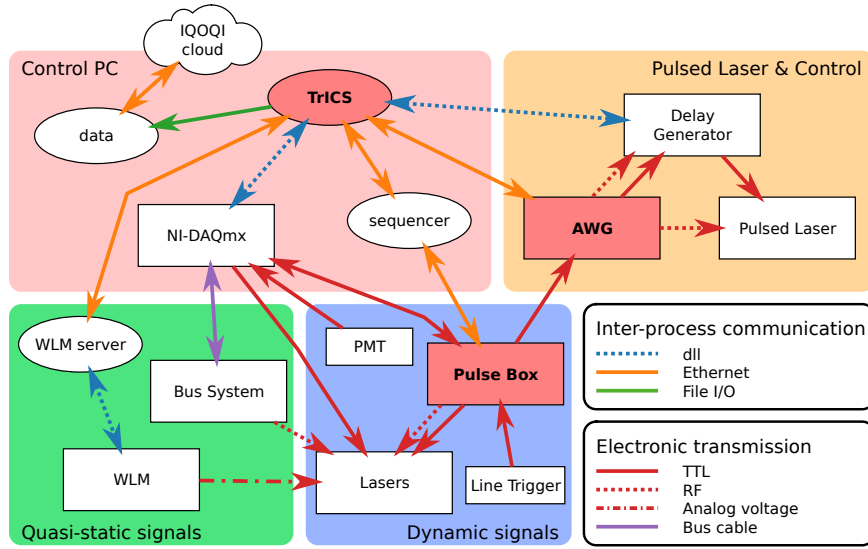


Figure 7.8: Schematic overview of the experiment control electronics and software. Software programs are represented by ellipses, hardware devices by rectangles. The highlighted shapes filled red indicate the entity (hardware or software) which is coordinating and controlling the other entities in their respective panel. Arrows indicate a form of communication between two entities, with the arrow head pointing in the direction of communication, and color and shape of the arrow line indicating the form of communication (see legend). The entities are grouped in four panels which are described in sections 5.3 (yellow panel), 7.3.1 (green and blue panels), and 7.3.2 (red panel).

to interact with the control electronics and manage the experiment was also programmed in-house and is called Trapped Ion Control Software (**TrICS**). It is installed on a standard PC, which serves as the “command center” of the laboratory and is called the *experiment control computer*. **TrICS** will be described in appendix B, other important software in section 7.3.2. An overview of the control system is provided in figure 7.8.

7.3.1 Electronics

The control signals of a quantum optics experiment and the electronics generating them can be divided into two groups [81]:

DYNAMIC SIGNALS These are signals that need to change during a single experiment cycle such as the intensity of the laser beams (on/off in the most trivial case) and the frequency of the 729 nm laser beam, which needs to be tuned in resonance with any of the $|4S_{1/2}, m_J = \pm 1/2\rangle \leftrightarrow |3D_{5/2}, m_J = -5/2, -3/2, \dots, 5/2\rangle$ transitions and their respective sidebands.

QUASI-STATIC SIGNALS Quasi-static signals do not need to change during an experiment cycle but only between two experiments, e. g. the frequency of all other laser beams, such as the cooling and pumping lasers, and both the AC and DC signals creating the trapping potential. PLLs and Pound-Drever-Hall (PDH) locks also fall in this category.

pulse box The heart of all experiments involving dynamic signals is a field-programmable gate array (FPGA)-based device called *pulse box* which is described in detail in the diploma thesis of Philipp Schindler [82]. It is the only device that can create dynamic signals (compare with the blue panel in figure 7.8). The pulse box used in this laboratory features 32 TTL outputs, eight TTL inputs and is equipped with eight DDS¹⁴, only one of which is used in this project. This DDS drives the AOM in double-pass configuration in the 729 nm laser's beam path and allows one to frequency-shift the light into resonance with any transition between the Zeeman split $4S_{1/2}$ and $3D_{5/2}$ states. The TTL outputs are connected to all devices that need to be triggered (e. g. the AWG) or switched on or off (e. g. RF switches and thus laser beams – see below) during a given experiment. The TTL inputs are used to start the experiment and to optionally synchronize it with an external clock, usually a signal derived from the 50 Hz cycle of the power grid. The FPGA is clocked with a 100 MHz signal, the DDSs are referenced with an 800 MHz signal, both derived from the 10 MHz lab reference. Therefore, the pulse box can toggle the TTL outputs with a resolution of 10 ns and the DDSs can synthesize frequencies $\lesssim 400$ MHz. It is connected to the experiment control computer via Ethernet and TTL channels.

The device that enables the experiment control computer to communicate via TTL signals is a PCI expansion card¹⁵ which features eight analog output channels, eight digital I/O channels and two counters. The only dynamic signals associated with the card are the TTL signals

¹⁴ AD9910

¹⁵ National Instruments PCI-6733

emitted by the [PMT](#) and detected by one of the counters and a [TTL](#) signal serving as a gate of the counter. All other channels emit or receive quasi-static signals: Two analog outputs are used to enable the ablation laser by supplying an interlock signal and two digital channels control the shutters that block the photoionization lasers and the red-shifted light in the 397 nm beam path, respectively.

The (quasi-static) [RF](#) frequencies needed for driving the [AOMs](#) described in the previous section are generated by 10 different [DDSs](#)¹⁶. These are controlled via what is called the *bus system* [[81](#), [83](#)] (also see the green panel in figure [7.8](#)). It is governed by a second PCI expansion card¹⁷ built in to the experiment control computer and which has 32 digital I/O channels. The bus system allows the user to control the output frequency and power of each [DDS](#) individually. The output signals are then fed into [RF](#) switches¹⁸ which transform the quasi-static [RF](#) signals into dynamic signals by turning them on or off based on a [TTL](#) signal from the pulse box. The [RF](#) signals are then amplified and fed into the corresponding [AOM](#).

bus system

A computer-controlled high voltage source¹⁹ is used to supply the voltages for the two endcap electrodes and the two compensation electrodes. One endcap is usually held at 432 V, the other one at 368 V, the compensation electrode above the trap at 83.0 V and the compensation electrode to the side of the trap at 55.2 V.

7.3.2 Software

[ThICS](#) is the computer software that coordinates and controls the experiments (see the red panel of figure [7.8](#)). It allows the user to conduct experiments by changing parameters and displaying the results of a measurement. [ThICS](#) is described in detail in appendix [B](#).

The software connecting and programming the pulse box via Ethernet is the *sequencer2*. It is written in python and serves as the link between [ThICS](#) and the pulse box. The *sequencer2* receives orders from [ThICS](#) and translates these into instructions for the pulse box. Once the pulse box has received the instructions it signals “ready” via a [TTL](#) channel to [ThICS](#), which may then at any time signal “start” via another [TTL](#) channel back to the pulse box. The only other [TTL](#) channel

¹⁶ 3x AD9854 and 7x AD9858

¹⁷ National Instruments PCI-6533 (PCI-DIO-32HS)

¹⁸ Mini-Circuits ZASWA-2-50DR+

¹⁹ Iseg EHS 8020x

between the pulse box and the experiment control computer is the aforementioned [PMT](#)-counter gate.

EXPERIMENTAL RESULTS

Experiments exploring the ion-laser interaction are presented in this chapter. Its first part is an introduction to the mathematical models used to fit, simulate and predict experimental outcomes. The second part then describes the experiments and results in detail and confirms characteristics described in section 6.3. The model described in section 8.1.2 as well as most experimental results presented in sections 8.2.2 through 8.2.5 have been published before in [65].

8.1 PULSE SIMULATION MODELS

Three different kinds of models were developed, tested and used in this thesis to simulate the interaction of a $^{40}\text{Ca}^+$ ion with a pulsed laser field resonant to the ion's $4S_{1/2} \leftrightarrow 4P_{3/2}$ transition. All models can be fit to experimental data in order to extract information about the laser light. In the following subsections each model will be discussed in terms of assumptions, advantages and disadvantages. The first model is an empirical model whose main advantage is the short computational time required to complete the calculation. The second model applies matrix operators to the density matrix to simulate how the pulses affect the ion's state. Its result is more accurate than that of the first model but it is computationally more demanding. Nevertheless, it is still sufficiently fast for fitting it to experimental data. The third model defines the light field either spectrally or temporally and solves the Lindblad master equation for a given Hamiltonian, initial state and collapse operators. It is the only model that can simulate chirped pulses but takes the longest of the three models to compute.

All models assume a three-level system in Λ configuration with a ground state $|1\rangle$, an excited state $|2\rangle$ and a second, quasi-stable ground state $|3\rangle$ as indicated in figure 8.1. The models consider spontaneous decay of state $|2\rangle$ into state $|1\rangle$ with decay rate Γ_{21} and into state $|3\rangle$ with decay rate Γ_{23} . In order to simulate the interaction of laser light with a $^{40}\text{Ca}^+$ ion, its $4S_{1/2}$ state is identified with $|1\rangle$, the $4P_{3/2}$ state with $|2\rangle$ and the $3D_{5/2}$ state with $|3\rangle$. The $3D_{3/2}$ state of $^{40}\text{Ca}^+$ does

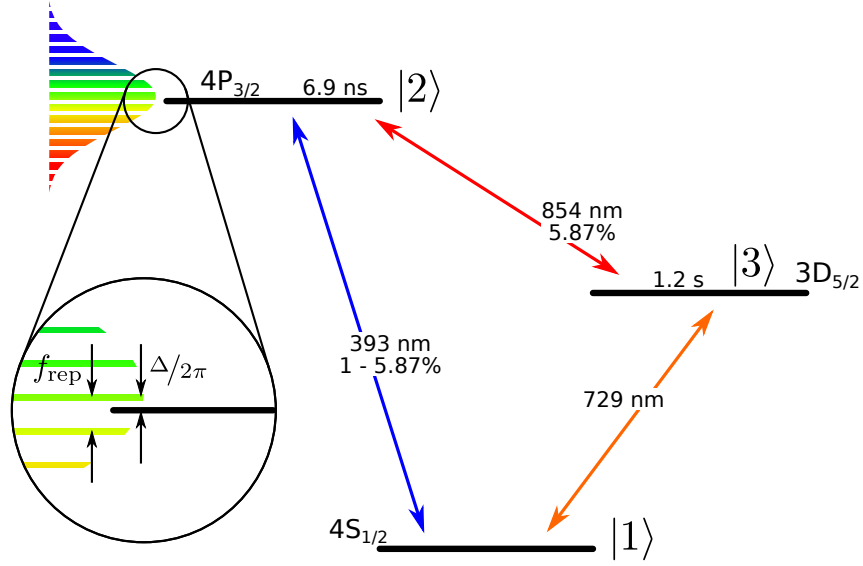


Figure 8.1: Simplified three-level scheme of $^{40}\text{Ca}^+$. Possible transitions are shown with their wavelengths and branching ratios [48], excited electronic states with their lifetimes [50–52]. The bell curve-shaped bars in the upper-left corner are a representation of the pulsed laser’s spectral modes. Image adapted from [65].

not need to be considered because in all experiments simulated by the models any population in this state is pumped back to $4S_{1/2}$ via $4P_{1/2}$ on a timescale of 10 ns with the 866 nm laser. Therefore, any decay to $3D_{3/2}$ effectively becomes a decay to $4S_{1/2}$ and the modified decay rates become

$$\begin{aligned}\Gamma_{21} &= (1 - p_{5/2}) \Gamma, \\ \Gamma_{23} &= p_{5/2} \Gamma,\end{aligned}\tag{8.1}$$

where $\Gamma = \frac{1}{\tau_P}$, $\tau_P = 6.9240(19) \text{ ns}$ is the lifetime of the $4P_{3/2}$ state [50] and $p_{5/2} = 0.0587(2)$ the probability of $4P_{3/2}$ to decay to $3D_{5/2}$ [48]. Any decay of $|3\rangle$ is also neglected, since the $3D_{5/2}$ state’s lifetime $\tau_D = 1168(9) \text{ ms}$ [52] is much longer than the cycle time of the experiments to be simulated of $\mathcal{O}(10 \text{ ms})$.

8.1.1 CW modes model

This model (naïvely) assumes the pulsed laser’s spectral modes are just individual CW lasers. Each mode’s effect on the ion is calculated

independently and contributes independently to the result, coherences between different components do not matter.

First, consider a two-level system with a lower ground state $|1\rangle$ and an upper excited state $|2\rangle$ (also compare with figure 8.1). If a CW laser light field interacts with this system the steady state solution for the upper state population ρ_{22} can be derived from the optical Bloch equations [84]:

$$\rho_{22} = \frac{\Omega^2}{2\Omega^2 + 4\Delta^2 + \Gamma^2}, \quad (8.2)$$

where Ω is the Rabi frequency, Δ is the detuning of the light-field frequency with respect to the atomic transition frequency and Γ the total spontaneous emission rate of the upper state.

If we add a weak decay channel into a third state $|3\rangle$ as described above, we can write the probability $P_{|3\rangle}(t)$ to find the system in state $|3\rangle$ after a light-system interaction time $t \gg 1/\Gamma$ as

$$\begin{aligned} P_{|3\rangle}(t) &= 1 - \exp(-\rho_{22} \Gamma_{23} t) \\ &= 1 - \exp\left(-\frac{\Omega^2}{2\Omega^2 + 4\Delta^2 + \Gamma^2} \Gamma_{23} t\right). \end{aligned} \quad (8.3)$$

This allows one to directly calculate $P_{|3\rangle} \equiv P_{3D_{5/2}}$ as a function of the interaction time t .

If we treat the pulsed laser system as a combination of $2N + 1$ CW lasers where each laser is detuned by the repetition rate f_{rep} with respect to the previous laser we can write the total probability to find the ion in the $3D_{5/2}$ state as

$$P_{D_{5/2}, \text{total}} = 1 - \prod_i \left(1 - P_{D_{5/2}}^i\right), \quad (8.4)$$

where $P_{D_{5/2}}^i$ is given by equation (8.3) with $\Delta \rightarrow \Delta_i = \Delta + i \cdot 2\pi f_{\text{rep}}$ the detuning of laser i and $i \in [-N, N]$. Measuring $P_{D_{5/2}, \text{total}}$ as a function of the detuning Δ and fitting equation (8.4) to the data allows one to extract information on the Rabi frequency and the detuning offset. In the last step it is assumed that the total steady state population of the excited state $\sum_i \rho_{22}^i$ is always small.

Even though the assumptions made in the derivation of this model hold only for pulse trains much longer than τ_P but shorter than τ_D and for weak pulses ($\Omega^2 \not\gg \Delta^2 + \Gamma^2$) such that only the $\pm N$ modes in the spectral vicinity of the transition frequency contribute to the excitation, the model is still useful for finding the laser frequency for which $\Delta = 0$ and to monitor changes in the Rabi frequency.

8.1.2 Quantum operation model

The second model represents the state of the three-level system as a density matrix ρ . Besides the assumptions made in the introduction, the model assumes infinitesimally short pulses. It calculates the effect of a single laser pulse by applying a series of quantum operators (matrix operators) to ρ .

To model the time evolution of the quantum state over one pulse period of duration $\tau_{\text{pulse}} = 1/f_{\text{rep}}$, we first account for the effect of a single picosecond pulse on the initial state by subjecting it to an x-rotation of the $|1\rangle - |2\rangle$ subsystem that transforms the initial density matrix ρ_0 into

$$\rho' = \mathcal{U}_{\mathcal{R}} \rho_0 \mathcal{U}_{\mathcal{R}}^\dagger, \quad (8.5)$$

where

$$\mathcal{U}_{\mathcal{R}} = \exp \left(\frac{i}{2} \theta (|2\rangle \langle 1| + |1\rangle \langle 2|) \right) \quad (8.6)$$

describes the x-rotation with rotation angle θ . It is related to the instantaneous Rabi frequency $\Omega(t)$ by

$$\theta = \int_{\tau_{\text{pulse}}} \Omega(t) dt. \quad (8.7)$$

Next, we take into account the possible detuning Δ of the laser light from the atomic transition $1 \leftrightarrow 2$ (see figure 8.1) and an additional light shift Δ' of the state $|3\rangle$ by a unitary $\mathcal{U}_{\mathcal{Z}}$ inducing phase shifts. The unitary applies z-rotations on two of the state's subsystems: one of the $|1\rangle - |2\rangle$ subsystem and another of the $|1\rangle - |3\rangle$ subsystem. The angles of rotation are proportional to τ_{pulse} , Δ and Δ' , respectively:

$$\rho'' = \mathcal{U}_{\mathcal{Z}} \rho' \mathcal{U}_{\mathcal{Z}}^\dagger, \quad (8.8)$$

with

$$\mathcal{U}_{\mathcal{Z}} = \exp \left(\frac{i}{2} [\Delta (|1\rangle \langle 1| - |2\rangle \langle 2|) + \Delta' (|1\rangle \langle 1| - |3\rangle \langle 3|)] \tau_{\text{pulse}} \right). \quad (8.9)$$

Finally, we account for spontaneous decay of state $|2\rangle$ during the pulse period by introducing the Kraus operators \mathcal{N} (no-decay) and \mathcal{D} (decay) describing this process:

$$\rho''' = \mathcal{N} \rho'' \mathcal{N}^\dagger + \mathcal{D} \rho'' \mathcal{D}^\dagger, \quad (8.10)$$

with

$$\mathcal{N} = |1\rangle \langle 1| + \sqrt{1-p-q} |2\rangle \langle 2| + |3\rangle \langle 3|, \quad (8.11)$$

and

$$\mathcal{D} = \sqrt{p} |1\rangle \langle 2| + \sqrt{q} |3\rangle \langle 2|, \quad (8.12)$$

where $p = 1 - \exp(-\Gamma_{21} \tau_{\text{pulse}})$ and $q = 1 - \exp(-\Gamma_{23} \tau_{\text{pulse}})$. Calculating the decay of the excited state only after applying the x- and z-rotation operators is acceptable, since the pulse length of 2 ps is very short compared to the state's lifetime of 6.9 ns.

To find the density operator ρ_n after a train of n pulses we iteratively apply these operators n times

$$\rho_n = \mathcal{N} \mathcal{U}_Z \mathcal{U}_R \rho_{n-1} \mathcal{U}_R^\dagger \mathcal{U}_Z^\dagger \mathcal{N}^\dagger + \mathcal{D} \mathcal{U}_Z \mathcal{U}_R \rho_{n-1} \mathcal{U}_R^\dagger \mathcal{U}_Z^\dagger \mathcal{D}^\dagger \quad (8.13)$$

and finish the calculation by letting state $|2\rangle$ decay completely. From the final density operator ρ_n we can easily calculate experimentally accessible observables such as populations $\text{Tr}(|1\rangle \langle 1| \rho_n)$, $\text{Tr}(|3\rangle \langle 3| \rho_n)$ and coherences $\text{Tr}(|1\rangle \langle 3| \rho_n)$, $\text{Tr}(|3\rangle \langle 1| \rho_n)$.

In section 6.3, it is discussed that the first pulse in a pulse train possibly has a different (usually higher) peak power and a phase difference with respect to later pulses. To accommodate these observations, we allow for the first pulse to have a different rotation angle θ^{1st} and phase $\delta\phi_{1,4}$, and replace \mathcal{U}_R with $\mathcal{U}_R^{\text{1st}}$ in equation (8.6):

$$\mathcal{U}_R \rightarrow \mathcal{U}_R^{\text{1st}} = \exp\left(\frac{i}{2} \theta^{\text{1st}} \left(e^{i\delta\phi_{1,4}} |2\rangle \langle 1| + e^{-i\delta\phi_{1,4}} |1\rangle \langle 2|\right)\right). \quad (8.14)$$

This model is the one usually to be fit to data as it runs sufficiently fast to allow for even hundreds of iterations in the fit routine and its assumptions are usually met in the conducted experiments.

8.1.3 Lindblad master equation solving models

The last simulation model uses QuTiP's [85, 86] `qutip.mesolve` function to solve the Lindblad master equation [54, 87]

$$\dot{\rho}(t) = -\frac{i}{\hbar} [H(t), \rho(t)] + \sum_n \frac{1}{2} [2C_n \rho(t) C_n^\dagger - \rho(t) C_n^\dagger C_n - C_n^\dagger C_n \rho(t)], \quad (8.15)$$

where H is the ion-light interaction Hamiltonian and the C_n are collapse operators. Since the only decay to be taken into account is that of state $|2\rangle$ into the two lower lying states there are two collapse operators,

$$\begin{aligned} C_1 &= \sqrt{\Gamma_{21}} \cdot |1\rangle\langle 2|, \\ C_2 &= \sqrt{\Gamma_{23}} \cdot |3\rangle\langle 2|. \end{aligned} \quad (8.16)$$

The Hamiltonian contains only a population transfer term between the states $|1\rangle$ and $|2\rangle$ with a complex, time-dependent coefficient $c(t)$

$$H(t) = c(t) |1\rangle\langle 2| + \text{H.c.} \quad , \quad (8.17)$$

which is the same Hamiltonian as that of equation (2.53). As was discussed in section 2.4, the coefficient $c(t)$ can be described either temporally in the time domain or spectrally in the frequency domain. Both ways have been implemented in the fitting routines and give the same results.

8.1.4 Simulation examples

The three models are mainly fit to experimental data and used to simulate the conducted experiments in the next section. This section should give the reader a more intuitive understanding of the interaction between a pulsed laser and an ion and the simulation thereof.

Figure 8.2 shows a temporally defined, chirped, $\pi/10$ pulse of the previously measured **FWHM** pulse length of 1.84 ps and **FWHM** spectral bandwidth of 540 GHz, which evaluates to¹ $\alpha = 1.652 \text{ ps}^{-2}$ and $\alpha' = 0.486 \text{ ps}^2$. The figure illustrates that the linear chirp present in the pulse leads to a quadratic temporal phase (and vice versa).

Figure 8.3 shows the effect of 500 of the above pulses on an ion which is initially in the $4S_{1/2}$ state. Part (a) of the figure shows only the first 50 pulses, simulated with the master equation solver, which allows one to track the ion's state even during the duration of a pulse (vertical parts of the population curves). Part (b) then shows all 500 pulses, simulated with the quantum operator model due to time constraints.

¹ using equations (2.57 - 2.63) and with $\gamma = 2\pi \cdot 540 \text{ GHz} / \sqrt{\ln(16)}$ and $\tau = 1.84 \text{ ps} / \sqrt{\ln(16)}$

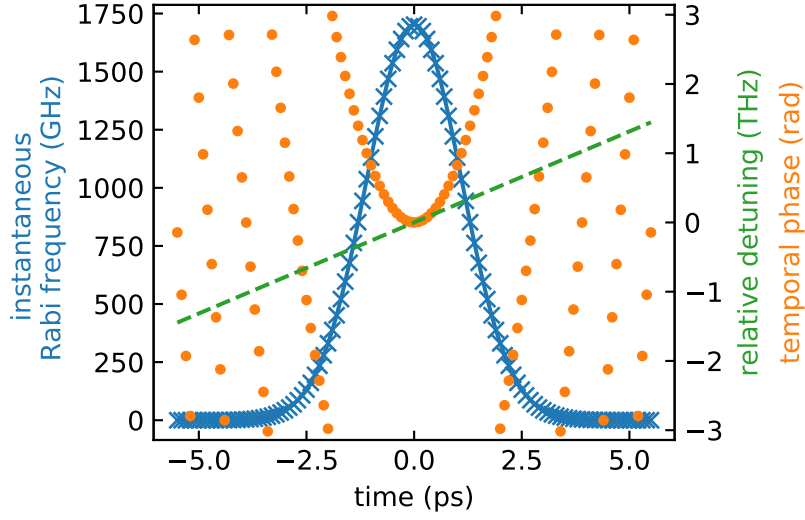


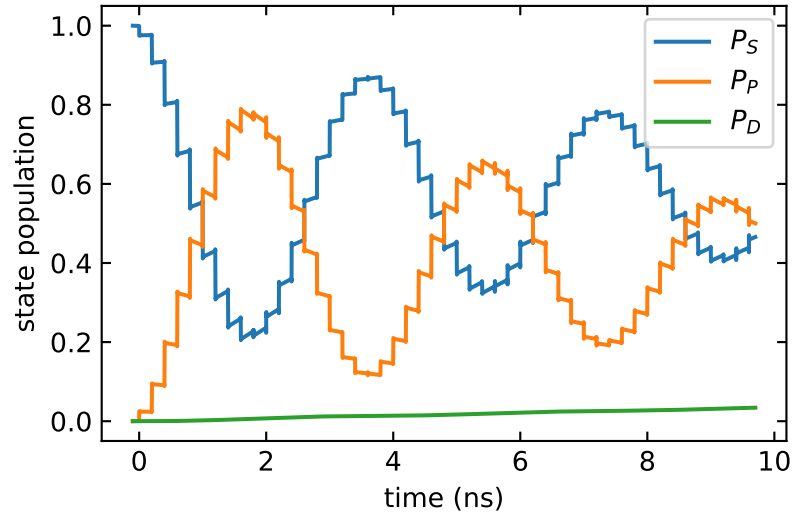
Figure 8.2: Time-dependent Rabi frequency (blue crosses: simulated data points, blue line: Gaussian fit thereof, both plotted on the left ordinate), temporal phase (yellow dots, right ordinate) and relative detuning (green slashed line, right ordinate) of a single pulse calculated from equation 2.58.

8.2 ION-STATE MANIPULATION WITH PULSES

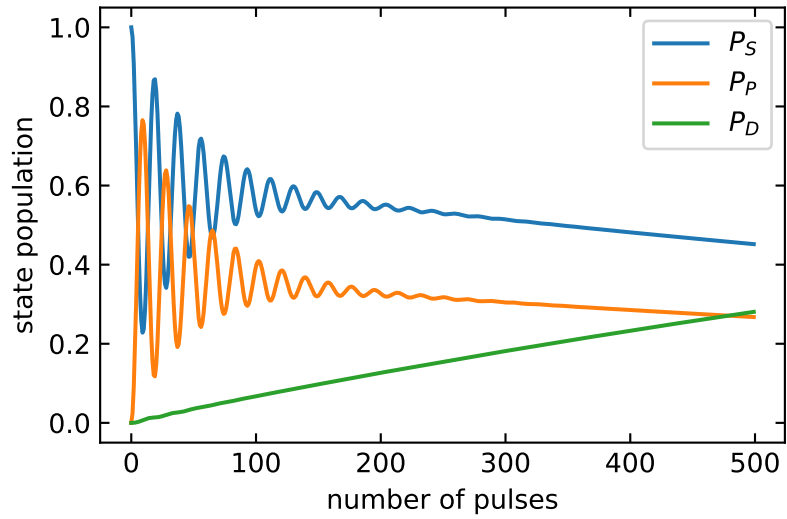
Before trying to implement a fast phase gate operation, the laser needs to prove that it can indeed excite the ion's $4S_{1/2} \leftrightarrow 4P_{3/2}$ transition and that it can do so coherently. Therefore, a series of experiments were devised to check these properties. The experiments described in this section also confirm characteristics presented in chapter 6 such as the phase offset of the first pulse after a dark time with respect to later pulses.

Typically, laser parameters such as power, number of pulses and detuning Δ are varied during the experiments. While it is straightforward to change the power and number of pulses – just by changing the pump diode current of the high power [EDFA](#) and by loading a different bit pattern into the [AWG](#), respectively – the detuning can only² be altered indirectly by changing the output frequency of the tunable [DDS](#) (see figure 5.3 on page 52) which changes the repetition rate of the seed laser. Since a change of $\Delta/2\pi$ by ± 3 GHz only requires a relative change $\Delta f_{\text{rep}}/f_{\text{rep}}$ of $\leq 4 \times 10^{-6}$, the change in f_{rep} is disregarded in

² Another option would be to change f_{CEO} , but in this system f_{CEO} is fixed at 20 MHz.



(a) The first 50 pulses



(b) All 500 pulses

Figure 8.3: Simulation of the effect of 500 pulses on the internal states of a $^{40}\text{Ca}^+$ ion with $\Omega = 2\pi \cdot 250 \text{ MHz}$ ($\theta = 0.05 \text{ rad}$) and $\Delta = 2\pi \cdot 100 \text{ MHz}$. Plotted are the probabilities to find the ion in the states $|4S_{1/2}\rangle$, $|4P_{3/2}\rangle$ and $|3D_{5/2}\rangle$ as a function of time. The first pulse arrives at 0 ns, consecutive pulses arrive with a rate of 5 ns^{-1} .

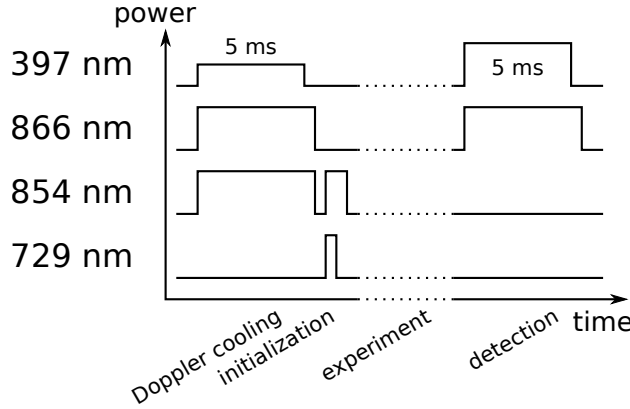


Figure 8.4: Beginning and end of every experimental sequence. Every experiment starts with Doppler cooling the ion crystal. Afterwards, it is initialized in the $|4S_{1/2}, m_J = +1/2\rangle$ state via optical pumping with the 729 nm laser, which is tuned in resonance with the $|4S_{1/2}, m = -1/2\rangle \leftrightarrow |3D_{5/2}, m = +3/2\rangle$ transition. After every experiment, the state of the ion is determined.

the analysis of the experiments. The DDS frequency f_{DDS} is converted to Δ using

$$\Delta = 2\pi \left(\frac{980 \text{ MHz} + f_{\text{DDS}}}{4} - 250 \text{ MHz} \right) \cdot n + \delta, \quad (8.18)$$

where $n \approx \frac{c}{\lambda_{393} \cdot 250 \text{ MHz}} \approx 3\,048\,484$ is the mode number of the frequency comb mode closest to the ion's $4S_{1/2} \leftrightarrow 4P_{3/2}$ transition wavelength λ_{393} (compare with equation (5.1)), c the speed of light and δ the detuning offset from $\Delta|_{f_{\text{DDS}}=20 \text{ MHz}}$. In experiments where the result is measured as a function of Δ , δ is an additional fit parameter in the analysis.

Every experiment starts with Doppler cooling the ion crystal and preparing the ion in the $|4S_{1/2}, m_J = +1/2\rangle$ state, and ends with reading out the ion state by discriminating between the $4S_{1/2}$ and $3D_{5/2}$ states via the electron shelving technique [88, 89]. This general experimental sequence is visualized in figure 8.4.

Unless stated otherwise, all following measurements and experiments presented in this thesis were conducted at a high power EDFA average output power of $\approx 600 \text{ mW}$ (measured after the TOD). During times when the Pockels cell was off and the pulses directed into a beam dump, the high power EDFA was seeded with pulses at $f_{\text{rep}} = 1.25 \text{ GHz}$.

Under these conditions, the average 393 nm power is about 9 mW (see figure 5.11 on page 65). Therefore, 393 nm pulse energies are always

$$E_{\text{pulse}} = \frac{P_{\text{avg}}}{f_{\text{rep}}} \approx \frac{9 \text{ mW}}{1.25 \text{ GHz}} = 7.2 \text{ pJ}.$$

8.2.1 Coherent population trapping

If two coherent laser beams excite the two transitions in a Λ -type atomic system, the atom can get trapped in a state that does not scatter any photons and therefore becomes dark [87]. The condition for this dark state to form is that the frequency difference between the two lasers beams has to be equal to the frequency splitting between the two ground states ($|1\rangle$ and $|3\rangle$ in figure 8.1):

$$E_{|1\rangle} - E_{|3\rangle} = \hbar\omega_{12} - \hbar\omega_{32}, \quad (8.19)$$

with $E_{|i\rangle}$ the energy of state $|i\rangle$ and ω_{i2} the frequency of the laser field exciting the transition $|i\rangle \leftrightarrow |2\rangle$. If the condition is satisfied and the atom either is already in or decays into the state

$$|\psi\rangle = \frac{\Omega_{32}}{\sqrt{\Omega_{12}^2 + \Omega_{32}^2}} |1\rangle - \frac{\Omega_{12}}{\sqrt{\Omega_{12}^2 + \Omega_{32}^2}} |3\rangle \quad (8.20)$$

(with Ω_{i2} the Rabi frequency associated with the laser field exciting the transition $|i\rangle \leftrightarrow |2\rangle$), the atom will stay in this state and can not be excited to $|2\rangle$, can not scatter any photons and hence remains dark. For this destructive interference to occur, it is necessary that both laser fields are coherent. Otherwise, random phase changes would destroy the interference and allow state $|2\rangle$ to be populated. Observing such dark resonance therefore is a way to show that the laser field is indeed coherent.

In order to show that the laser field of the pulsed laser is coherent, it is used instead of the 397 nm laser to excite the ion and collect fluorescence photons at 393 nm wavelength. As figure 8.5 visualizes the 854 nm laser is simultaneously illuminating the ion to provide the necessary second light field. The other repumping laser at 866 nm ensures the ion is not lost in the quasi-stable $3D_{3/2}$ state. In order to improve the signal quality, two measurements are taken. At first, the pulsed laser and the two repumping lasers are sent to the ion while the PMT measures the number of scattered photons. During this time, both photons from the ion fluorescence and photons scattered

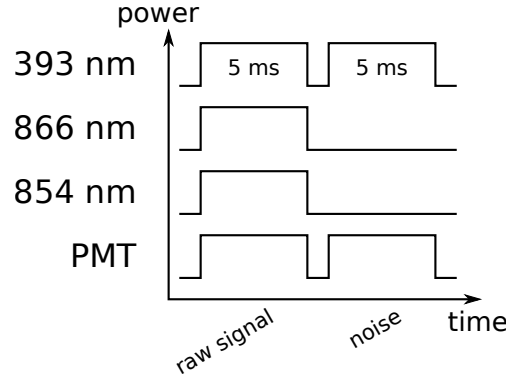


Figure 8.5: Experimental sequence for coherent population trapping. PMT: photomultiplier tube.

off e.g. the trap blades will reach the [PMT](#) and contribute to the “raw signal” \mathcal{S}_{raw} . Next, the measurement is repeated but without the two repumpers. Therefore, the ion will decay into one of the quasi-stable D states within $\mathcal{O}(\tau)$ and not scatter any photons. Any photons still being detected by the [PMT](#) can therefore not stem from the ion and are considered unwanted noise \mathcal{N} . The noise counts can now be deducted from the raw signal counts to yield the “signal” $\mathcal{S} = \mathcal{S}_{\text{raw}} - \mathcal{N}$. Recording the count rate $\mathcal{S}/5\text{ ms}$ as a function of detuning Δ_{393} of the pulsed laser allows one to observe the bright resonance peak and the dark resonance.

The expected count rate r is the product of state $|2\rangle$ population ρ_{22} , the decay rate Γ_{21} and the efficiency of the detection system ϵ_{det}

$$r = \epsilon_{\text{det}} \Gamma_{21} \rho_{22}. \quad (8.21)$$

The population ρ_{22} in turn is a function of the laser detunings Δ_{393} and Δ_{854} , the Rabi frequencies Ω_{393} and Ω_{854} , the decay rates Γ_{21} and Γ_{23} , and the optical decoherences $\gamma_1 = \gamma_2 = \Gamma/2$ (also compare with equation (8.1)). The steady-state expression of γ_{22} can be found in reference [90] and will not be reproduced here. Due to the large number of pulses (25×10^6), pulse switching effects described in section 6.3 and affecting only the first one or two pulses can be disregarded. For the same reason the experiment does not necessitate the use of a pulse picker that is faster than the fundamental repetition rate.

Figure 8.6 shows the count rate as a function of Δ_{393} for five different pulsed laser powers P_{393} . The fit curves were obtained in a simultaneous fit to all five data sets, the fit parameters were Δ_{854} , Ω_{854} , δ_{393} , ϵ_{det}

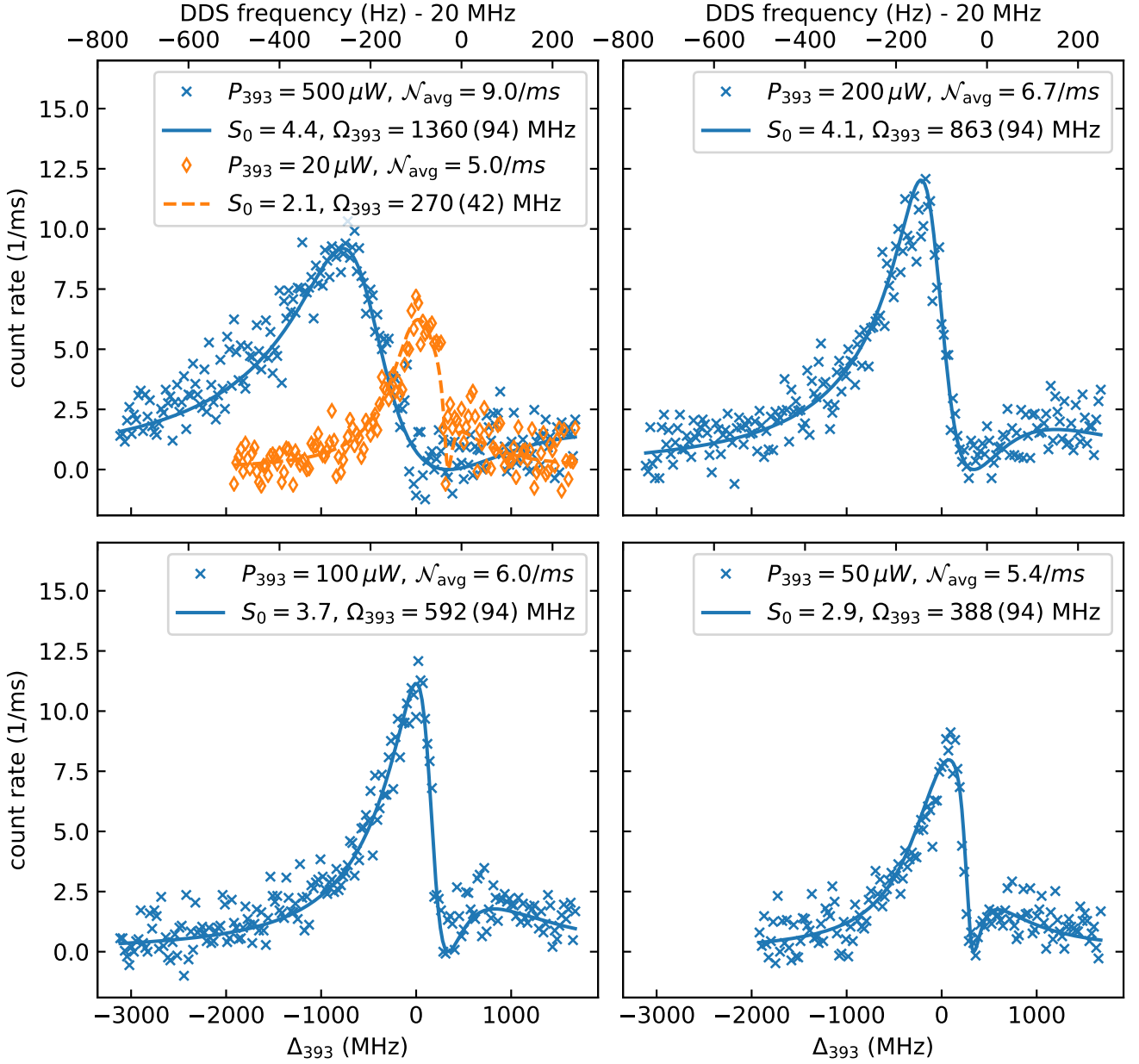


Figure 8.6: Experimental observation of a dark resonance for five different 393 nm laser powers P_{393} . The power and frequency of the 854 nm laser were kept constant during the measurement. The data points are the difference of two measurements, “raw signal” and “noise”, which is why some show a negative count rate. The lines are a simultaneous fit of equation (8.21) to all five data sets and only differ in the value of Ω_{393} . S_0 is the saturation parameter [90]. The common fit parameters are $\Delta_{854} = 338(21)$ MHz, $\Omega_{854} = 75.1(56)$ MHz, $\delta_{393} = -477(36)$ MHz, $\epsilon_{\text{det}} = 0.0017(15)$. The error values are one standard deviation of the fit parameter estimate.

and the five different values of Ω_{393} . The most notable feature is that the count rate drops to 0 in all five data sets for $\Delta_{393} = \Delta_{854}$, which demonstrates that the laser field of the 393 nm pulsed laser is indeed coherent.

A disadvantage of this experiment is that the measured count rate is proportional to ϵ_{det} which therefore needs to either be precisely known or added to the fit parameters which is the case here. Another problem is that the signal-to-noise ratio (SNR) \mathcal{S}/\mathcal{N} can become small ($\ll 1$) either when \mathcal{S} drops to 0 in the dark resonance or for large P_{393} because this leads to a lot of photons scattered by e.g. the trap blades and contributing to \mathcal{N} . This is why many of the relative errors of the fit parameters shown in the figure are $> 10\%$.

8.2.2 Coherent excitation using many pulses

Experiments populating the $3D_{5/2}$ state and using the electron shelving technique to determine state populations instead of measuring photons scattered directly from the laser field under consideration are a way to avoid the low SNRs of the experiment discussed in the previous section. A disadvantage is that the population of the excited state can not be measured directly but can only be inferred using measured populations of the (quasi-) stable ground states and known decay rates.

Exciting the $4S_{1/2} \leftrightarrow 4P_{3/2}$ transition with the pulsed laser without also using the 854 nm laser to excite the $3D_{5/2} \leftrightarrow 4P_{3/2}$ transition causes the ion to decay into the $3D_{5/2}$ state with rate $\rho_{22}\Gamma_{23}$ where it is lost to the 393 nm excitation. Instead, it will stay there until the end of the experiment – one cycle of the experiment takes only $T_{\text{cycle}} \approx 10 \text{ ms} \ll \tau_D$ – at which point the ion's state is determined. The probabilities to find the ion either in the $4S_{1/2}$ or $3D_{5/2}$ state are independent of ϵ_{det} and the probability errors are independent of \mathcal{N} . Both disadvantages of the experiment described in the previous section are therefore avoided here.

Pulse trains of between $n = 500$ and $n = 5000$ pulses are sent to the initialized ion as seen in figure 8.7 (with $m = 1$). The measurement is repeated 100 times to statistically determine the probability of the ion having decayed into the $3D_{5/2}$ state. Just as in the experiment described in the previous subsection, the number of pulses is sufficiently large to disregard pulse switching effects described in section 6.3.

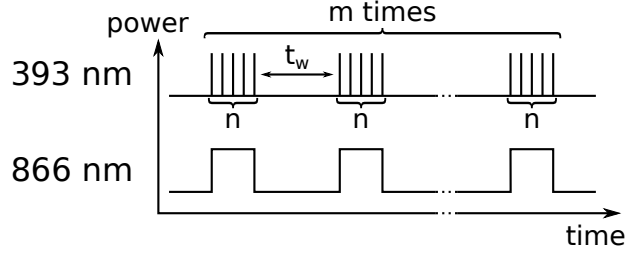


Figure 8.7: Experimental sequence of coherent excitation with pulse trains. A pulse train of n pulses coherently drives the $4S_{1/2} \leftrightarrow 4P_{3/2}$ transition. The pulse train is repeated a total of m times with a waiting time t_w between each two repetitions. Usually, $t_w = 20 \mu\text{s} \gg \tau_P = 6.924 \text{ ns}$, with τ_P the $4P_{3/2}$ state's lifetime. This figure was taken from [65].

The $3D_{5/2}$ state population P_D is measured as a function of laser detuning and pulse train length. Figure 8.8 shows data sets for repetition rates ranging from 1.25 GHz to 5 GHz. Each data set consists of four data sub-sets which differ only in the number of pulses. In order to extract θ , both the [CW](#) modes model and the quantum operator model were fit to the data. In each case the simulation is fit simultaneously to each of the four sub-sets such that the result is a single value for θ . The only other fit parameter is a detuning offset which is eliminated in the figure. For the repetition rates of 5 GHz (2.5 GHz, 5/3 GHz, 1.25 GHz) and using the [CW](#) modes model, the obtained values are $\theta = 0.23(5)^\circ$ ($0.35(4)^\circ$, $0.40(8)^\circ$, $0.39(17)^\circ$). Using the quantum operations model, the obtained values are $\theta = 0.22(5)^\circ$ ($0.32(4)^\circ$, $0.36(7)^\circ$, $0.35(21)^\circ$). All fit values of the two models are within the respective fit errors of each other. Under the conditions presented here, the two models perform equally well, the differences would hardly be visible in figure 8.8. For that reason, only the quantum optics model fit is plotted there.

Simulations of this experiment with perfect π -pulses ($\theta = 1$) predict on the one hand the outcome of the experiment under such conditions and on the other hand point out shortcomings of the [CW](#) modes model. Figure 8.9 shows the result of the two simulation models ([CW](#) modes model in panels (a) and (c), quantum operation model in panels (b) and (d)), for $n = 500$ (panels (a) and (b)) and $n = 5000$ (panels (c) and (d)) π -pulses and for four different repetition rates. Since each pulse always swaps the $4S_{1/2}$ and $4P_{3/2}$ state populations, one would expect to find a result independent of Δ . Looking at the figure, it is apparent

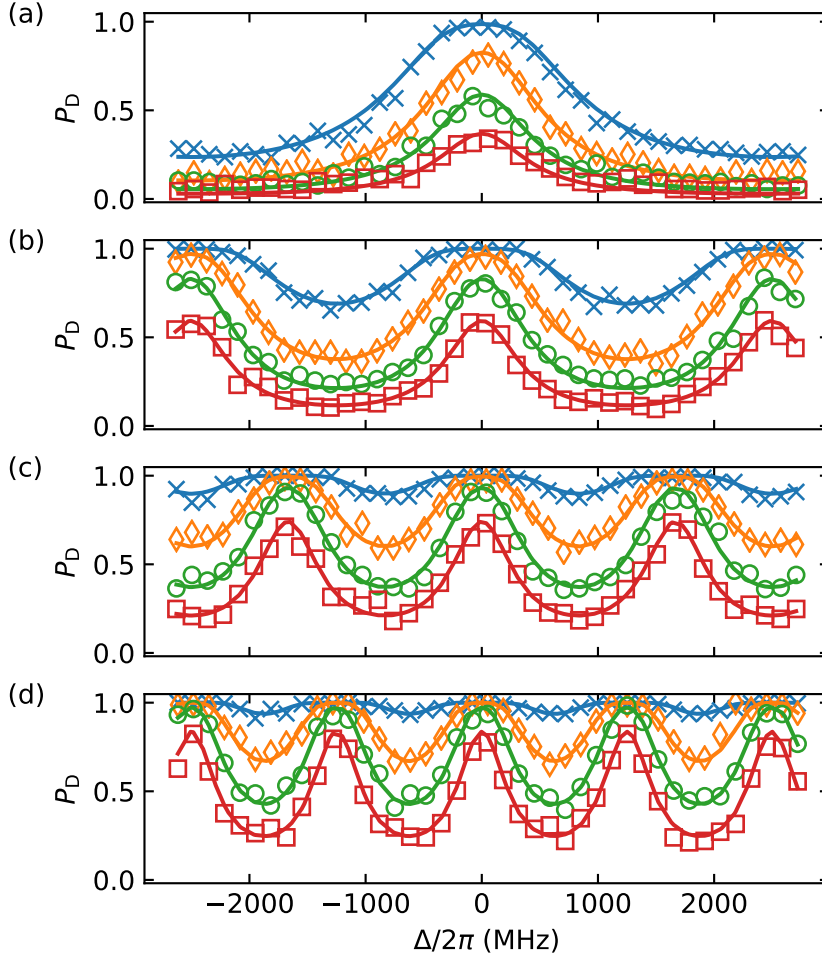


Figure 8.8: Probability P_D to find the ion in the $3D_{5/2}$ state as a function of the detuning Δ of the laser frequency with respect to the $4S_{1/2} \leftrightarrow 4P_{3/2}$ transition frequency. Blue crosses using 5000 pulses, yellow diamonds 2000 pulses, green circles 1000 pulses, red squares 500 pulses. The lines in each graph are a model fit to the respective data as described in the text, allowing the determination of θ . (a) 5 GHz repetition rate, $\theta = 0.22(5) \text{ \AA}$. (b) 2.5 GHz repetition rate, $\theta = 0.32(4) \text{ \AA}$. (c) 5/3 GHz repetition rate, $\theta = 0.36(7) \text{ \AA}$. (d) 1.25 GHz repetition rate, $\theta = 0.35(21) \text{ \AA}$. This figure was taken from [68].

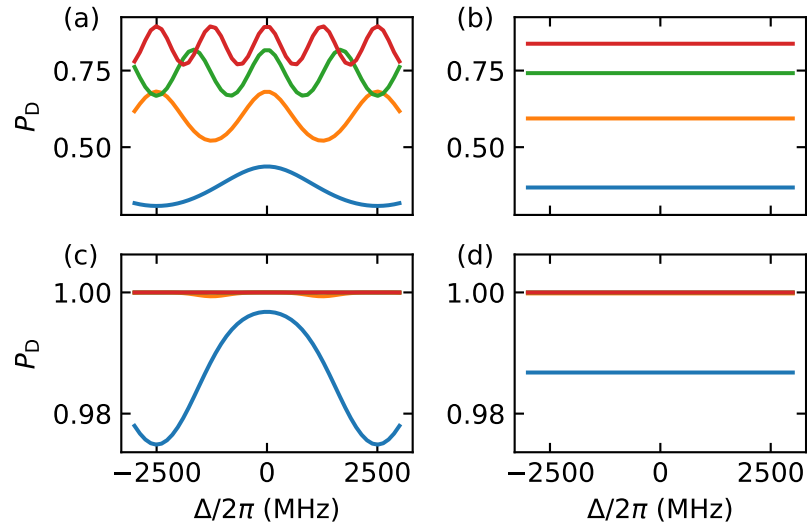


Figure 8.9: Simulated probability P_D to find the ion in the $3D_{5/2}$ state as a function of the detuning Δ using perfect π -pulses. The panels show simulations of the **CW** modes model (left column) and the quantum operation model (right column), the experiment was simulated using $n = 500$ pulses (top row) and $n = 5000$ pulses (bottom row) and at the repetition rates of 5 GHz (blue), 2.5 GHz (yellow), 5/3 GHz (green) and 1.25 GHz (red). Expecting P_D to be independent of Δ for π -pulses, it is obvious that the assumptions used in the **CW** modes model are violated here.

that only the quantum operation model predicts values for P_D that are independent of Δ . In contrast, the [CW](#) modes model fails for such high Rabi frequencies ($\Omega/2\pi = f_{\text{rep}}/2 \Leftrightarrow \theta = 1$), as it still shows a Δ dependence. Both statements hold for both $n = 500$ and $n = 5000$ pulses. This shows that the [CW](#) modes model only performs well for weak pulses with $\theta < 1$, as was stated before.

8.2.3 Coherent excitation using few pulses

Using few-pulse trains to excite the ion allows one to gain crucial insights into single pulse dynamics and characteristics, and to confirm the results from section 6.3. After initializing the ion, pulse trains of between 1 and 12 pulses are sent to the ion. The signal is amplified by repeating the pulse train m times as shown in the experimental sequence in figure 8.7 to accumulate population in the $3D_{5/2}$ state [48], choosing $m \approx 1/p_{5/2}$. Between repetitions, a waiting time $t_w = 20 \mu\text{s}$ much larger than the $4P_{3/2}$ state's lifetime ensures that any population in that state has decayed. Afterwards, ion fluorescence on the $4S_{1/2} \leftrightarrow 4P_{1/2}$ transition is collected in order to determine whether the ion has decayed into the dark $3D_{5/2}$ state. The measurement is repeated 100 times to statistically determine the $3D_{5/2}$ state population as a function of the laser detuning for different pulse train lengths.

Figure 8.10 shows experimental data and a simulation of the quantum operations model of the probability for being in the $3D_{5/2}$ state after $m = 20$ pulse trains. The detuning Δ and the number of pulses are varied for different repetition rates. The simulation parameters are obtained by a fit to the data. Free fit parameters are θ , the phase offset of the first pulse $\delta\phi_{1,4}$ and a detuning offset. It is known from earlier measurements described in section 6.3 that the first pulse in the case of $f_{\text{rep}} = 5 \text{ GHz}$ also has a different intensity, an additional fit parameter is used in that case: the rotation angle of the first pulse θ^{1st} . All fit values are within three standard deviations of those acquired previously with long pulse trains (section 8.2.2), as well as those acquired with the Michelson interferometer (section 6.3). Contrary to measuring $\delta\phi_{i,j}$ with the interferometer, this measurement is able to also determine the sign of $\delta\phi_{i,j}$ and therefore to distinguish between phases $\delta\phi_{i,j} = \Phi$ and $\delta\phi_{i,j} = -\Phi$ (the latter being the same as $\delta\phi_{i,j} = 2\pi - \Phi$). Therefore, $\delta\phi_{1,4}$ at 5 GHz is about 1.25β and not 0.75β as the ellipse fit suggested. Furthermore, θ^{1st} is found to be a factor of about $\sqrt{3}$ larger than θ for

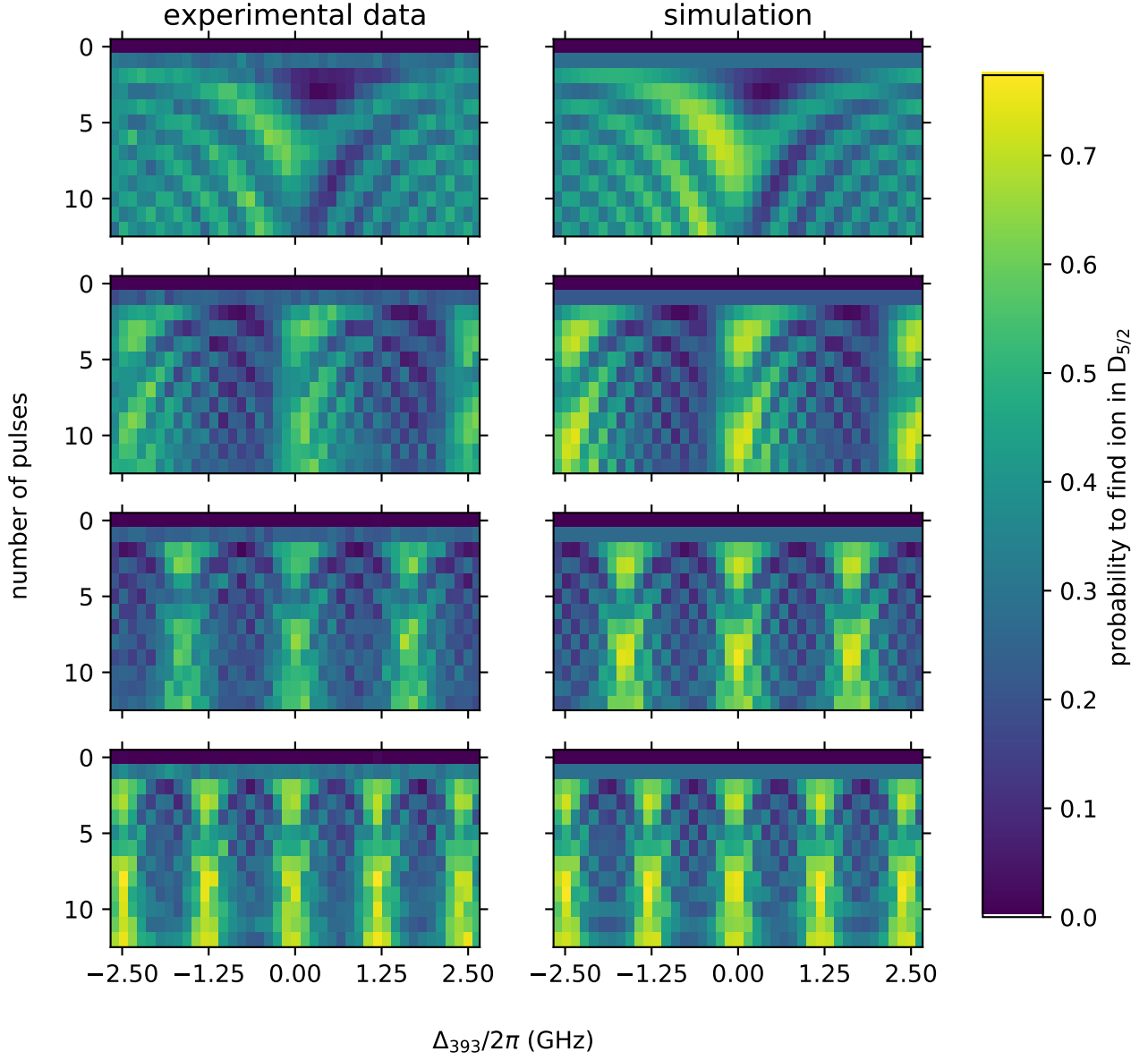


Figure 8.10: Probability to excite the ion to $3D_{5/2}$ with different numbers of pulses and detuning. Left column: experimental data; right column: simulation/fit of the quantum operations model. 1st row: $f_{\text{rep}} = 5 \text{ GHz}$, $\theta^{1\text{st}} = 0.353(1) \text{ rad}$, $\theta = 0.195(18) \text{ rad}$, $\delta\phi_{1,4} = 1.282(1) \text{ rad}$. 2nd row: $f_{\text{rep}} = 2.5 \text{ GHz}$, $\theta = 0.312(10) \text{ rad}$, $\delta\phi_{1,4} = 0.361(2) \text{ rad}$. 3rd row: $f_{\text{rep}} = 5/3 \text{ GHz}$, $\theta = 0.339(7) \text{ rad}$, $\delta\phi_{1,4} = 0.088(3) \text{ rad}$. 4th row: $f_{\text{rep}} = 1.25 \text{ GHz}$, $\theta = 0.358(3) \text{ rad}$, $\delta\phi_{1,4} = 0.051(1) \text{ rad}$. The asymmetry evident in the first two rows is due to the phase shift of the first pulse with respect to later pulses. This figure was taken from [65].

the 5 GHz repetition rate, which is the expected amount for a three times larger pulse intensity area (also compare with section 6.3).

8.2.4 Single pulse with area π

In order to check if a single pulse can act as a π -pulse the previous experiment is repeated with only one pulse while varying the 393 nm light power ($n = 1$, $m = 15$, n and m as in figure 8.7). From the experimentally determined $3D_{5/2}$ state probability P_D after the $m = 15$ repetitions of a single pulse the $4P_{3/2}$ state probability P_P after only one single pulse is calculated using

$$P_P = \frac{1}{p_{5/2}} \left(1 - (1 - P_D)^{\frac{1}{m}} \right). \quad (8.22)$$

Due to measurement fluctuations, this can sometimes lead to unphysical values of $P_P > 1$ if a value for P_D is measured that happens to be larger than the maximum expectation value of $P_{D, \max} = 1 - (1 - p_{5/2})^m \approx 0.60$.

The excitation probability is a function of the sine squared of a phase, which is proportional to the Rabi frequency Ω . Hence, P_P is plotted versus the square root of the 393 nm pulse energy, which is also proportional to Ω (and θ), in figure 8.11. The data points should therefore follow the curve

$$P_P = P_{P, \max} \cdot \sin^2 \left(\pi \sqrt{E_{\text{pulse}}} / \xi \right), \quad (8.23)$$

where ξ is a proportionality factor and $P_{P, \max}$ is the maximum probability of a single pulse exciting the ion to the $4P_{3/2}$ state. A fit of this curve to the data yields $\xi = 11.3(3) \sqrt{\text{pJ}}$ and $P_{P, \max} = 96(2) \%$, showing how close the pulses are to achieving a π -pulse. The experimental value for $E_{\pi\text{-pulse}} = (\xi/2)^2 = 32(3) \text{ pJ}$ is in agreement with the theoretical prediction of 30 pJ calculated using the transition's well-known decay rate and wavelength, and the measured beam parameters³ [44].

The maximum transfer efficiency is currently limited either by a detuning of the center frequency of the pulse spectrum with respect to the ion's resonance frequency or by self-phase modulation (SPM) induced by the fiber, both effects would reduce the maximum transfer efficiency, but neither is incorporated in equation (8.23). Simulations

³ Please note that the maximum 393 nm light power plotted in figure 5.11e (110 mW) and figure 8.11 (58 mW) was measured at the same fundamental light power. The discrepancy is due to coupling losses in the fiber guiding the 393 nm light to the ion.

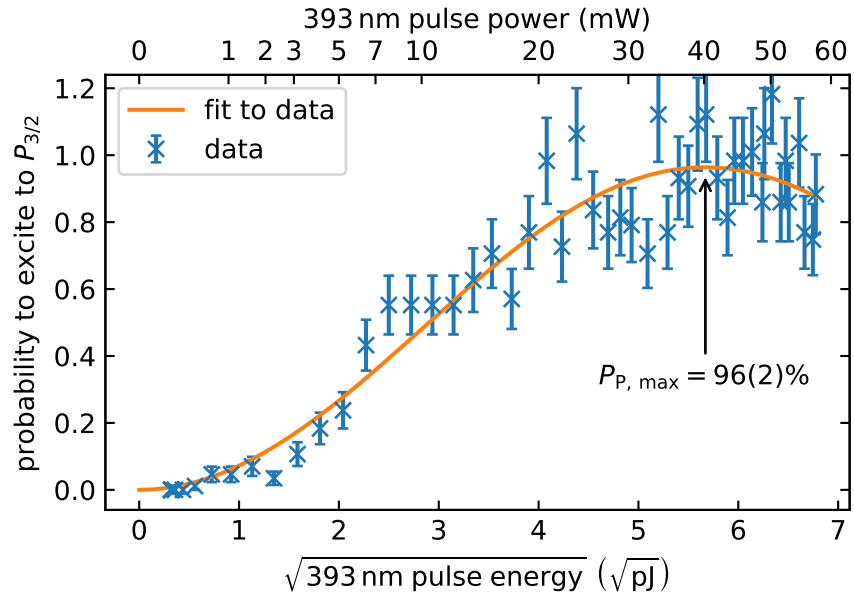


Figure 8.11: Probability to excite the ion to $4P_{3/2}$ with a single pulse as a function of 393 nm light power. $P_{p, \max}$ is the maximum excitation probability to the $4P_{3/2}$ state and determined by a fit to the data. Measurement noise can cause unphysical values of $P_p > 1$ (see text). Picture taken from [65].

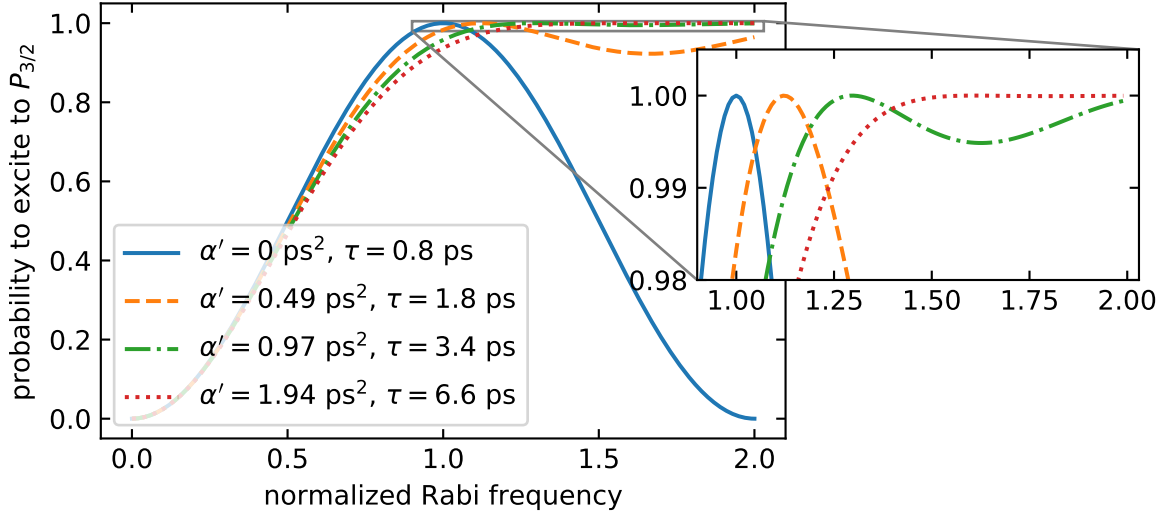


Figure 8.12: Simulated probability to excite the ion to $4P_{3/2}$ with a single pulse as a function of normalized Rabi frequency Ω/Ω_0 , where $\Omega_0/2\pi = \frac{1}{2}f_{\text{rep}}$ ($\Leftrightarrow \theta = 1$) for $\alpha' = 0$. All curves were simulated using the same spectral bandwidth of 0.54 THz (FWHM) but different linear spectral chirp α' . The dashed yellow curve corresponds to the measured spectral bandwidth, pulse width and linear spectral chirp.

indicate that the SPM-induced maximum phase shift is $\sim 0.4\beta$ in a 30 pJ pulse, which reduces the maximum transfer efficiency to $< 75\%$ for the current experimental settings. However, the experimental data presented above shows that the maximum transfer efficiency is well above 75%. The discrepancy is most likely due to an uncertainty in the nonlinear refractive index n_2 of fused silica fiber at 393 nm which is assumed to be $n_2 = 1.5 \times 10^{-20} \text{ m}^2/\text{W}$ [91].

Malinovsky and Krause have shown that population transfer with chirped pulses is more robust and more selective than population transfer with transform-limited pulses [59]. The process is known as adiabatic rapid passage (ARP) and especially makes the population transfer insensitive to intensity fluctuations. In order to find conditions for robust population transfer, the experiment is simulated using the master equation solver – which is the only model that can simulate chirped pulses – for four pulses of different linear spectral chirp α' . The result is shown in figure 8.12. If there is no chirp ($\alpha' = 0$) the probability of a single pulse to excite the ion from the $4S_{1/2}$ to the $4P_{3/2}$ state as a function of Rabi frequency follows a \sin^2 shaped curve. Simulated pulses with the same amount of chirp as measured in the 393 nm pulses require a 12 % higher Rabi frequency to reach the maxi-

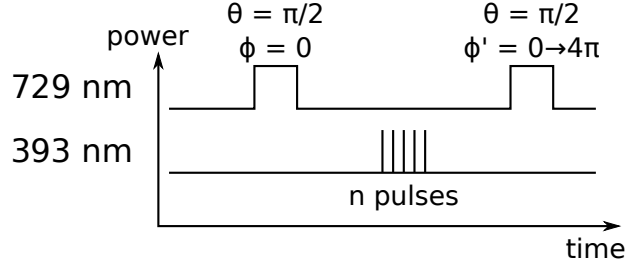


Figure 8.13: Sequence of a Ramsey contrast decay and revival experiment. The first 729 nm laser pulse creates a coherent superposition of the ion's internal $4S_{1/2}$ and $3D_{5/2}$ states. A controlled and variable number of 393 nm laser pulses act on the remaining $4S_{1/2}$ state population, transferring population to the $4P_{3/2}$ state and possibly back, potentially reducing the S-D coherence. Finally, it is analyzed how much coherence remains by varying the phase of the second 729 nm laser pulse and measuring the $3D_{5/2}$ state probability, while keeping the Ramsey time $t_R = 10 \mu\text{s}$ much shorter than the coherence time of the superposition ($\mathcal{O}(1 \text{ ms})$). Picture taken from [65].

imum excitation probability, but the excitation probability only drops to a minimum of 91 % after the first maximum. A simulated pulse with twice the observed chirp requires a 30 % higher Rabi frequency to reach the maximum excitation probability, but the excitation probability never drops below 99.5 % after the first maximum and therefore is more robust against intensity fluctuations than the unchirped pulse. Adding even more chirp further improves these values, but requires an even higher Rabi frequency to reach the maximum excitation probability. The simulations therefore suggest that it would be advantageous to add more chirp to the 393 nm pulses, as long as the required Rabi frequency can be reached.

8.2.5 Ramsey contrast decay and revival

The coherent manipulation of a qubit entails a precise quantum control of the relative phase of the two qubit states' amplitudes. The experiments of the previous subsections used only one of the two qubit states and the relative phase appeared only as an unobservable global phase. By designing experiments where the second qubit state serves as a phase reference, access to the desired information is obtained.

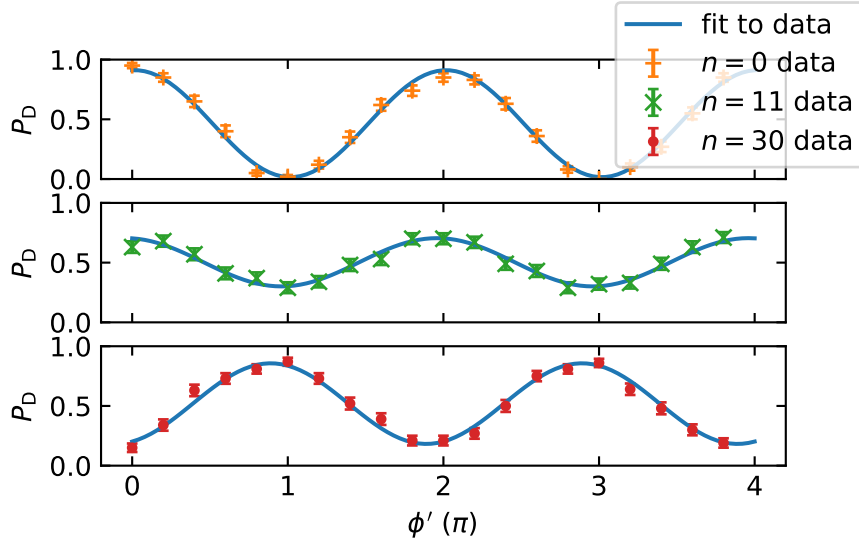


Figure 8.14: Three exemplary data sets of a Ramsey experiment. From the sinusoidal fit contrast and phase are determined and plotted in figure 8.15. Note how the contrast diminishes from $n = 0$ to $n = 11$ and then increases again from $n = 11$ to $n = 30$ while the phase changes by π .

Towards this end, few-pulse trains are interacting with the ion during the waiting time of a Ramsey experiment probing the qubit coherence [32]. The phase coherence at the end of the Ramsey sequence is monitored by first creating a coherent superposition of the two qubit states by a $\frac{\pi}{2}$ -pulse on the qubit transition with a 729 nm laser as illustrated in figure 8.13:

$$|\psi\rangle = \frac{1}{\sqrt{2}} (|1\rangle + |3\rangle) \equiv \frac{1}{\sqrt{2}} (|4S_{1/2}\rangle + |3D_{5/2}\rangle)$$

Next, variable numbers of picosecond pulses are used to coherently drive the $4S_{1/2} \leftrightarrow 4P_{3/2}$ transition. If there is any population remaining in the $4P_{3/2}$ state after the pulses, this part of the population will undergo spontaneous decay and thus destroy the coherence. Finally, the amount of remaining coherence of the superposition state and the phase between the two qubit states is extracted: The Ramsey interferometer is closed with a second $\frac{\pi}{2}$ -pulse and the $3D_{5/2}$ state population $P_{D_{5/2}}$ is measured as a function of the phase ϕ' of this pulse. The resulting experimental data is fitted by a sinusoidal curve,

$$P_{D_{5/2}} = \frac{1}{2} (1 + C \cdot \cos(\phi' + \Phi)) \quad (8.24)$$

in order to extract the contrast C and the phase Φ of the interference signal as seen in figure 8.14. There are two limiting cases: If the contrast is equal to one, the ion was still in a fully coherent superposition of the $4S_{1/2}$ and $3D_{5/2}$ states and there was no spontaneous decay of the $4P_{3/2}$ state. If the contrast is zero, all the initial $4S_{1/2}$ state population had been transferred to the $4P_{3/2}$ state and spontaneous decay has destroyed all coherence. For a resonant excitation of the $4S_{1/2} \leftrightarrow 4P_{3/2}$ transition, the phase is expected to undergo jumps of π each time the ion's state population is transferred to the $4P_{3/2}$ state and back again to the $4S_{1/2}$ state by the pulse train. This is due to the fact that the quantum states of a two-level system undergoing a 2π rotation pick up a minus sign, $|0\rangle \xrightarrow{2\pi} -|0\rangle$.

From a given density matrix ρ , C and Φ can be calculated using

$$C = \gamma \sqrt{\text{Tr}^2(\sigma_x^{13}\rho) + \text{Tr}^2(\sigma_y^{13}\rho)} \quad (8.25)$$

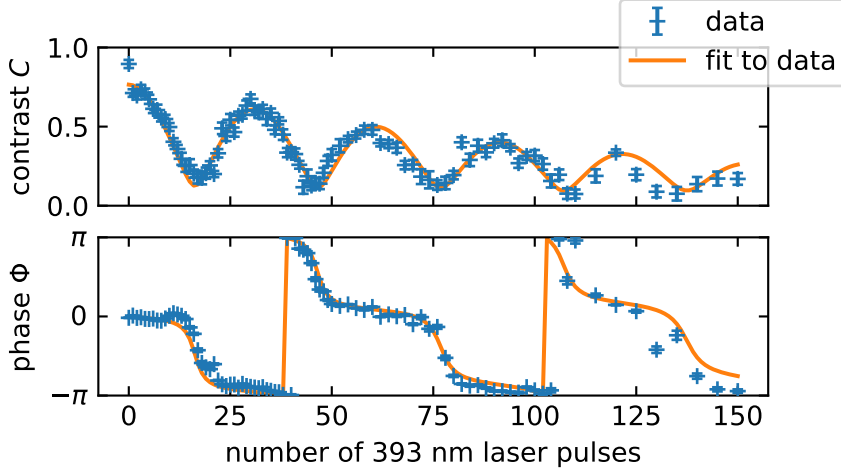
and

$$\Phi = \arg [\text{Tr}(\sigma_x^{13}\rho) + i \text{Tr}(\sigma_y^{13}\rho)] , \quad (8.26)$$

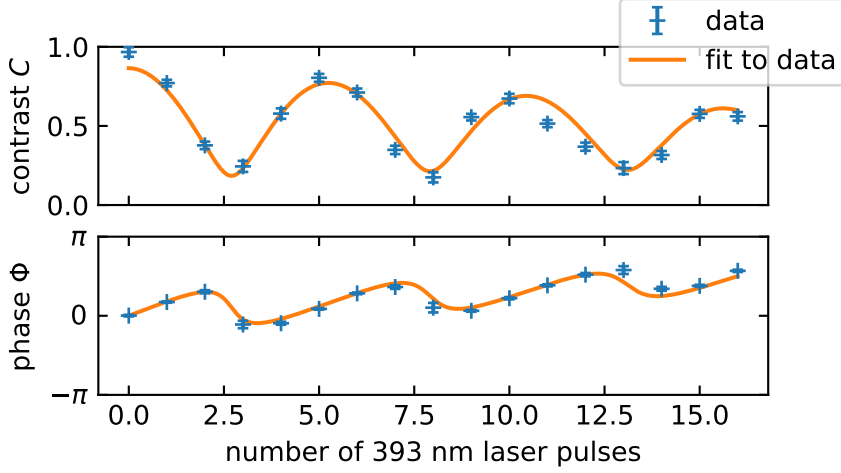
with $\sigma_x^{13} = |3\rangle\langle 1| + |1\rangle\langle 3|$ and $\sigma_y^{13} = i(|3\rangle\langle 1| - |1\rangle\langle 3|)$, and where γ is an additional scaling factor to account for a reduced contrast due to experimental imperfections.

The measurement is repeated as a function of the number n of 393 nm laser pulses. For a dataset taken with low pulse power (figure 8.15a), it took about 15 optical pulses at $f_{\text{rep}} = 5$ GHz to complete a π -pulse, which corresponds to $\theta \approx 0.065(1)$ rad. The fitted detuning of $\Delta/2\pi = 0.029(4)$ GHz of the nearest comb mode to the ion transition shows that the transition was resonantly excited. The data shows that the $4S_{1/2} \leftrightarrow 4P_{3/2}$ transition is driven coherently and that each time the ion returns to the $4S_{1/2}$ state, the data is consistent with the observation of phase jumps by π . Figure 8.15b shows another measurement which was carried out at a higher pulse power, that was the same as for the measurements presented in the other subsections. The same structure as in the first data set can be observed but only about 2.5 optical pulses are needed to complete one π -pulse on the transition. The phase jumps are washed out, because the Bloch vector does not cross the poles of the $|S\rangle - |P\rangle$ Bloch sphere. A fit of the simulation of the ion-light interaction to the experimental data returns $\theta = 0.375(4)$ rad and $\Delta/2\pi = 0.14(2)$ GHz.

The result of a simulation of the experiment using π -pulses shows the contrast jumping between 0 and 1 for each pulse as seen in fig-



(a) Data set taken at $f_{\text{rep}} = 5 \text{ GHz}$ at low light power ($\theta = 0.065(1) \text{ B}$, $\Delta/2\pi = 0.029(4) \text{ GHz}$, $\Delta'/2\pi = -0.005(1) \text{ GHz}$, $\gamma = 0.77(7)$).



(b) Data set taken at $f_{\text{rep}} = 1.25 \text{ GHz}$. We determine $\theta = 0.375(4) \text{ B}$, $\Delta/2\pi = 0.14(2) \text{ GHz}$, $\Delta'/2\pi = -0.184(4) \text{ GHz}$, $\gamma = 0.87(5)$.

Figure 8.15: Contrast and phase of Ramsey experiments enclosing a picosecond pulse train (see figure 8.13). For a given number of 393 nm laser pulses, the contrast and phase of the Ramsey fringe were obtained by scanning the phase of the second Ramsey pulse (see figure 8.14 for a exemplary Ramsey fringes). The fit (solid line) results from a model based on equations (8.13), (8.25) and (8.26), using fractional numbers of pulses in order to obtain a continuous curve as a guide to the eye. The reduction of the initial contrast visible in the plot is most likely caused by unwanted leaking light during the experiment. Figure taken from [65].

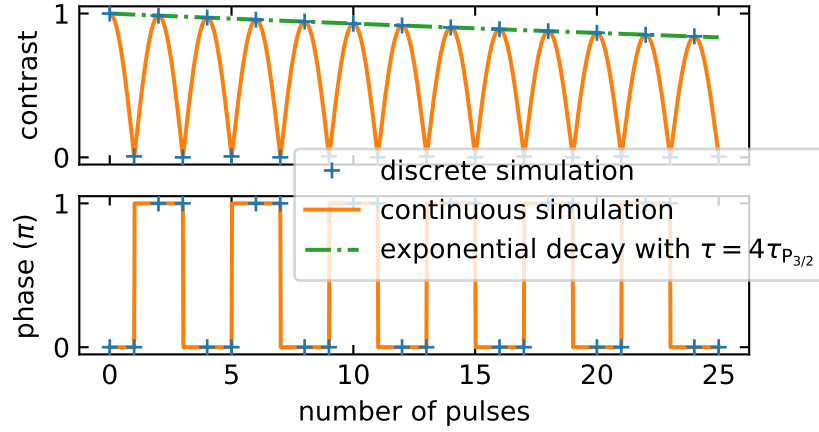


Figure 8.16: Contrast and phase of a simulation of a Ramsey contrast decay and revival experiment using perfect π -pulses with $f_{\text{rep}} = 5\text{GHz}$. The quantum operation model was used for both the discrete simulation (simulating integer numbers of pulses) and the continuous simulation (simulating fractional numbers of pulses).

ure 8.16, while the higher level contrast shows an exponential decay with a decay constant of $\tau = 4\tau_{4P_{3/2}}$.

8.2.6 Conclusion

The angle θ by which a single laser pulse rotates the Bloch vector of a sub-state about an equatorial axis can be measured in several ways. Letting an ion interact with hundreds of consecutive pulses and afterwards measuring the probability of finding the ion in the $3D_{5/2}$ state allows the experimenter to deduce θ , yet does not require picking single pulses. The measured data can be analyzed and interpreted quickly using a number of simplifying assumptions, as discussed in section 8.1.1. Sending only a few pulses instead of hundreds allows measuring not only θ , but also the phase offset of the first pulse after a dark time, i.e. a pause in the pulse train. By injecting few-pulse trains into the waiting time between the two $\pi/2$ -pulses of a Ramsey experiment, θ , as well as the phase change of the $|4S_{1/2}\rangle$ state due to the pulses can be measured. The results of these three measurements are summarized in table 8.1. The methods produce the same results within their respective error margins but each has its advantages and disadvantages as described below.

REP. RATE (GHz)	EXPERIMENT	θ (π)	$\delta\phi_{1,4}$ (π)
5	interferometer		0.74 or 1.26
	many pulses	0.22(5)	
	few pulses	0.195(18)	1.282(1)
2.5	interferometer		0.37
	many pulses	0.32(4)	
	few pulses	0.312(10)	0.361(2)
5/3	interferometer		0.10
	many pulses	0.36(7)	
	few pulses	0.339(7)	0.088(3)
1.25	interferometer		0.04
	many pulses	0.35(21)	
	few pulses	0.358(3)	0.051(1)
	Ramsey exp.	0.375(4)	

Table 8.1: Summary of fit parameters for the different experiments

Using many pulses to coherently excite the ion transition provides information about the pulse characteristics, such as pulse intensity and detuning. The method requires neither the ability to pick single pulses nor a laser resonant to the $4S_{1/2} \leftrightarrow 3D_{5/2}$, 1 Hz linewidth transition. Rather, only readily available lasers stabilized to a linewidth of $\lesssim 1$ MHz are needed. The only parameters required to fit the data are the number of pulses n and the well-known decay rates Γ_{PS} and Γ_{PD} . From the fit, θ and the detuning offset between the transition frequency and a laser mode can be extracted. This allows tuning the laser into resonance with the transition.

The method works well for any laser repetition rate f_{rep} as long as it is much larger than the $4S_{1/2} \leftrightarrow 4P_{3/2}$ transitions linewidth. Also, the rotation angle should satisfy $\theta \leq \pi$, since rotation angles $\theta' = \pi + \delta$ can not be discerned from $\theta = \pi - \delta$.

By using only few pulses to excite the ion (method 2), single pulse dynamics can be observed and additional information about the pulse characteristics gained, such as changing phase shifts and pulse powers. These measurements reproduced the results obtained both with long pulse trains and with the Michelson interferometer.

The Ramsey contrast technique is experimentally more challenging than the procedures described in the previous paragraphs. It is necessary to create a coherent superposition of the $4S_{1/2}$ and $3D_{5/2}$ states which requires a few-kHz linewidth laser. However, the method allows tracking the phase of the $4S_{1/2}$ state with respect to the phase reference provided by the $3D_{5/2}$ qubit state. Furthermore, the signal does not need to be amplified and hence amplification noise is avoided.

As stated before and unless noted otherwise, all experiments presented in this thesis were conducted at an average output power of the high power EDFA of ≈ 600 mW (measured after the [TOD](#) compressor) which corresponds to ≈ 9 mW 393 nm light power and results in a pulse energy of $E_{\text{pulse}} \approx 7.2$ pJ. Nevertheless, it was possible to increase the 393 nm light power to $\gtrsim 100$ mW as seen in [figure 5.11](#), which results in $E_{\text{pulse}} \gtrsim 45$ pJ, and which suffices to create pulses that act as π -pulses with 96.4(19) % probability.

Part III

SUMMARY, OUTLOOK AND APPENDIX

SUMMARY AND OUTLOOK

9.1 SUMMARY

The possible advantages of a quantum computer over classical computers have spurred a great research effort in this domain. The requirements of a scalable quantum computer have been identified and condensed into the DiVincenzo criteria [11]. They include, *inter alia*, a transformation which is able to entangle the qubits. Previous entangling gate operations in trapped ions have a physical lower limit in their duration because they have to spectroscopically resolve motional sidebands of the ion crystal. In 2003, it was proposed to instead use ultrafast laser pulses to apply state-dependent momentum kicks to a two-ion crystal in order to create an entangling phase gate operation that takes less – possibly orders of magnitude less – time than previous such operations.

In this thesis, both a large amount of technical work and a publication in the field of quantum information processing and atomic physics [65] is covered. The technical work involves the setup of a new laser spectroscopy experiment and the development and implementation of a flexible, python-based scripting API for the integration of scientific hardware into the experiment control software. The publication covers the design and setup of a pulsed laser system for implementing a fast phase gate operation as well as its characterization. The thesis picks up the content of the publication and expands upon it. The thesis' main purpose is to develop, build and characterize a pulsed laser system for the realization of the fast phase gate operation. The state-dependent momentum kicks are implemented by resonantly exciting the $4S_{1/2} \leftrightarrow 4P_{3/2}$ transition at 393 nm in $^{40}\text{Ca}^+$.

The pulsed laser system is seeded by an optical frequency comb and inherits its stability. The repetition rate is increased to 5 GHz, a pulse picker allows to select arbitrary pulse sequences. The picked sequence is amplified and the pulses are frequency-doubled twice to the desired wavelength of 393 nm and a maximum average power of 110 mW. Finally, the pulses are guided to the ion trap in an optical fiber and focused on the ion with a waist of $11.8(3) \mu\text{m}$.

Measurements with a frequency-resolved optical gating (FROG) device reveal a pulse width of 1.8 ps and a spectral bandwidth of 540 GHz, which means the pulses are chirped. Assuming Gaussian shaped pulses and a linear chirp, the (linear) temporal chirp is $\alpha = 1.652 \text{ ps}^{-2}$. Interferometric measurements show that both intensity and phase of the first pulse after a dark time are different from those of subsequent pulses. By now, the element responsible for both effects has been identified and is being replaced.

The ion is confined in a linear Paul trap and oscillates axially at a frequency of typically 819 kHz. Ion fluorescence is detected by both a photomultiplier tube (PMT) and an electron-multiplying charge-coupled device (EMCCD). The laser setup for ionizing, Doppler cooling, state initialization and state detection are all external cavity diode lasers (ECDLs) and locked to a wavelength meter (WLM). An ultra stable laser (linewidth $\sim 1 \text{ Hz}$) is available for exciting the ion's qubit transition ($4S_{1/2} \leftrightarrow 3D_{5/2}$). The lasers and other electronic devices are controlled by Trapped Ion Control Software (TrICS). TrICS allows the experimenter to integrate and control new electronic equipment as well as take and save data with an ion crystal. Its development was progressed as part of the thesis.

In order to analyze and predict the interaction of the pulsed laser light with an ion, three interaction models were developed. The first model assumes the spectral modes of a long pulse train are independent continuous wave (CW) lasers acting on the ion and contributing to its excitation. It is limited in its application but is nevertheless useful to tune one spectral line into resonance with the ion transition as it requires very little computing time. The second model assumes infinitesimally short pulses that turn the Bloch vector of the $4S_{1/2}/3D_{5/2}$ sub-state by fixed angles around different axes to account for the excitation and detuning. The model can therefore simulate the effect of a single pulse on the ion and still runs sufficiently fast on a standard computer to fit it to experimental data. The third model uses either spectrally or temporally defined pulses and calculates their effect on an ion by solving the master equation. This is computationally demanding but it is the only model that can account for chirped pulses.

The first experiments conducted with an ion in this thesis excite the ion transition with long trains of pulses, and therefore do not require picking individual pulses. One experiment collects fluorescence at 393 nm while simultaneously illuminating the ion with the

pulsed laser light and another laser at 854 nm, nearly resonant with the $3D_{5/2} \leftrightarrow 4P_{3/2}$ transition. This leads to coherent population trapping and the observation of a dark resonance, and therefore already shows that the laser is exciting the ion transition coherently. Another experiment used the pulsed laser to populate the $4P_{3/2}$ state from where the ion can decay into the $3D_{5/2}$ state. By afterwards measuring the $3D_{5/2}$ state probability, it is possible to calculate the Rabi frequency with which the ion transition is excited.

Further experiments used single pulses – mostly between 1 and 16, but also up to 150 – to excite the ion transition. The earlier interferometric measurements are confirmed by exciting the $4S_{1/2} \leftrightarrow 3D_{5/2}$ transition with single pulses, waiting for the excited state to decay and measuring the $3D_{5/2}$ state probability. An experiment using a single pulse showed that one pulse can excite the ion to the $4P_{3/2}$ state with a probability of 96.4 %. Finally, an experiment where single pulses are injected during the waiting time of a Ramsey sequence gives access to the phase that the pulses transfer to the ion state and which was an unobservable global phase in all other experiments.

9.2 OUTLOOK

The next steps in the realization of a fast phase gate are the following: First, the phase shifts described in section 6.3 should be eliminated. At the time of this writing, the source of the phase shifts has been identified as the second semiconductor optical amplifier (SOA), which is currently being replaced by a new erbium doped fiber amplifier (EDFA). It has been confirmed that the new amplifier does not exhibit the undesired behavior.

Second, the pulses have to be split in order to send them in counter-propagating pairs to the ions. Furthermore, there needs to be a way to select which pulse of a pair arrives at the ions first. Figure 9.1 shows a proposed scheme for switching between two different beam paths. The scheme allows switching between the paths while the laser light is still red (786 nm), but uses the same non-linear crystal for second harmonic generation (SHG). The former condition results in a greater extinction ratio compared to splitting blue light (393 nm) as explained in section 5.4, the latter one ensures that two pulses traveling along the two different paths still have equal properties after the frequency conversion. The small angle between the two paths inside the non-linear crystal should not pose an issue since the crystal is periodically

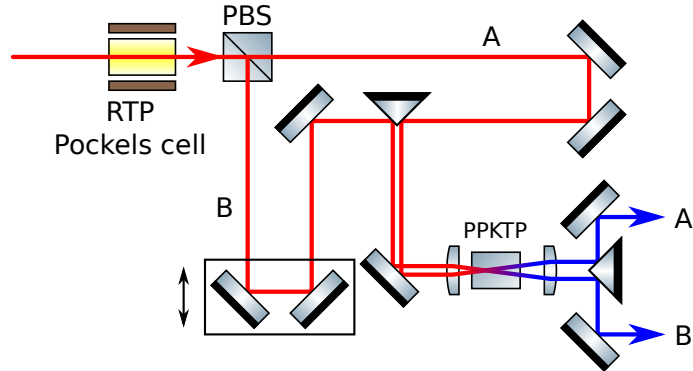


Figure 9.1: Proposed scheme for switching between two beam paths. The scheme allows switching between the paths while the laser light is still red (786 nm), but requires only one non-linear crystal.

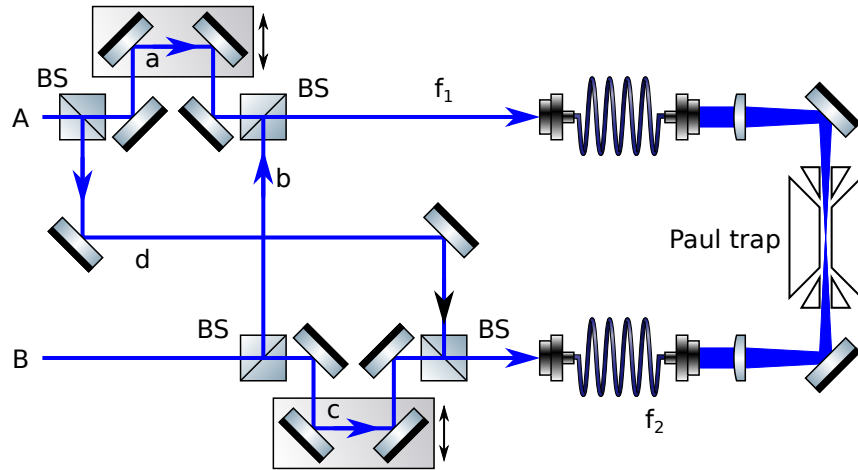


Figure 9.2: Proposed scheme to split and combine pulses from two different beam paths. A pulse originating in path A (B) is split into a pulse pair and sent to the ion crystal such, that the “top” (“bottom”) pulse reaches the crystal first. Path lengths should be chosen, such that $(d + f_2) - (a + f_1) \approx (b + f_1) - (c + f_2) \approx c_0 \cdot 10 \text{ ps}$, where c_0 is the speed of light. BS: 50:50 beam splitter.

poled for quasi-phase matching, where the angle of the input light beam is not a sensitive parameter. After the switching, the pulses of each path can then be split and combined in 50:50 beam splitters with the respective other path as depicted in figure 9.2. By appropriately choosing the optical path length differences, one can ensure that a pulse entering one path is split into a pulse pair and sent to the ion crystal such that the first pulse of the pair to reach the ions is coming from, say, the left, and vice-versa for the other path. In order to compensate splitting and combining the pulses in 50:50 beam splitters, pulses with an initially by a factor-of-four larger intensity area are required. For this purpose, a new high power EDFA with an average output power of up to 10 W has already been ordered. The proposed scheme comes with two potential problems, but both can be resolved as follows: For one, one could be concerned about the phase stability between the two pulses of a pulse pair. The phase difference between a single pair of pulses is in this scheme indeed subject to drifts. If we denote the optical path lengths between the beam splitters by a , b , c and d , and the optical path lengths between the beam splitters and the ions by f_1 and f_2 as seen in figure 9.2, the phase difference $\Delta\phi_A$ ($\Delta\phi_B$) of pair of pulses that originated from a single pulse coming from input A (B) is

$$\Delta\phi_A = k(f_1 + a - d - f_2) \quad (9.1)$$

$$\Delta\phi_B = k(-f_1 - b + c + f_2), \quad (9.2)$$

with k the light's wave vector. In both equations, the term $\pm(f_1 - f_2)$ appears, which is in general not equal to zero and will dominate the phase fluctuations due to acoustic noise picked up by the fibers. Also, since there is no CW light¹ traveling along the fiber, standard methods for fiber noise cancellation will not work. The reason this problem is mitigated in a phase gate operation is the following observation. All pulse sequences proposed so far and covered in this thesis require an equal number of momentum kicks in the positive and negative direction (compare the numbers of positive and negative z_k parameters in section 4.2). This implies that for every pulse in input A there will be exactly one other pulse in input B within the total time of the gate T and the phase difference of these pulses adds up to

$$\delta\phi = \Delta\phi_A + \Delta\phi_B = k(a - b + c - d). \quad (9.3)$$

Here, the f_i terms have canceled out under the assumption that they are constant on time scales of $\mathcal{O}(T)$. The remaining terms of $\delta\phi$ can

¹ or at least an uninterrupted pulse train

be considered constant on time scales of at least hours and can be compensated by single qubit rotations after a gate operation was completed. Furthermore, the two fibers could add dispersion to the pulses and therefore stretch them in time. It was shown in section 8.2.4 that additional dispersion (i. e. chirp) would make the pulses more robust against intensity fluctuations, as long as the two pulses of every pulse pair have an equal amount of chirp.

The third step will then be the characterization of the π -pulses, of the momentum they transfer onto the ions and of the phase acquired by the qubit states under the effect of a pulse sequence, which will hence lead to the desired phase gate operation.

After the phase gate has been successfully demonstrated, it would be interesting to add more ions to the trapped crystal and perform the gate operation between any two of them. For an L -ion crystal, the commensurability conditions in equation (4.12) would be replaced by [28]

$$0 = \sum_{k=1}^N z_k e^{i\omega_p t_k}, \quad (9.4)$$

and equation (4.14) by

$$\Theta = 8 \sum_{p=1}^L \eta_p^2 b_1^{(p)} b_2^{(p)} \sum_{m=2}^N \sum_{k=1}^{m-1} z_m z_k \sin(\omega_p \Delta t_{mk}). \quad (9.5)$$

While it would be increasingly difficult to solve these $L + 1$ equations individually, the authors of [28] argue, that this is not even necessary: Since the fast phase gate would be faster than the oscillation period in the ion crystal, at least a gate for two neighboring ions would only need to satisfy the condition equations for local ions.

9.3 CONCLUSIONS

This thesis made key steps toward the realization of an ultrafast phase gate operation. Once the pulse energy has been increased by about a factor of four, the system should be able to implement the gate operation with a fidelity of $1 - 10^{-8}$ in about 170 ns using the fast robust antisymmetric gate (FRAG) scheme, which is much shorter than our trap period of about 1.2 μ s. The duration is limited by the laser system's maximum repetition rate of 5 GHz and could be further reduced by increasing the repetition rate. Such fast entangling gate

operations would increase the maximum number of gate operations that can be performed within an ion-qubit's coherence time by about two orders of magnitude.

PREPARING THE LASER SYSTEM FOR DAILY WORK

This appendix chapter is meant as a guide for future scientists working with the picosecond-laser system described in this thesis. The chapter lays out the steps necessary to switch on the system and to start the experimental day. It is formatted as a numerated list so it can be used similar to a preflight checklist.

1. Ensure that the frequency comb is mode-locked and the AC and DC values which are displayed in the control program are $AC > 1400$ and $DC > 650$. If one of these conditions is not met, refer to the frequency comb manual.
2. Ensure that the carrier envelope offset (CEO) beat note has an SNR of at least 30 dB (compare with figure A.1). Lock the CEO and the repetition rate to the radio frequency (RF) reference. Optically locking the repetition rate does not provide sufficient flexibility in changing its set-point.
3. Occasionally, usually only after maintenance of the frequency comb, the polarization controllers shown in figure A.2 have to be adjusted, such that the output of the monitor port is minimized to < 15 mW.
4. On the experiment control computer, in Trapped Ion Control Software (TICS) start the UserAPI process `freq_comb`. Check that it is now possible to control the fiber comb's 20 MHz tunable direct digital synthesizer (DDS) (see figure 5.3, panel B).
5. In the electronics rack of the pulsed laser, check the temperatures of the two cavities and the continuous wave (CW) fiber laser. Cavity 1 is usually held at a temperature around 22 °C, cavity 2 around 23 °C and the CW laser's fiber around 37 °C.
6. Lock the CW laser to the frequency comb mode with the highest transmission signal as seen in figure A.3a. Panel (b) of that figure shows a typical comb/CW-laser beat note. Then lock first cavity 1 and then cavity 2 to the CW laser. The cavities' transmission signals should resemble those in panels (c) and (d). If they do

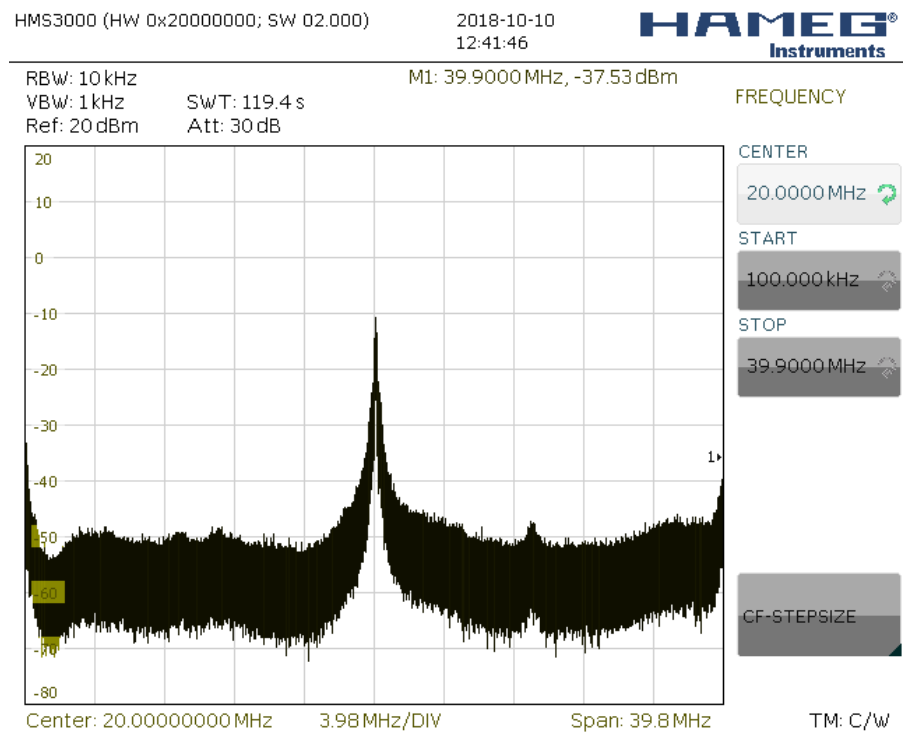


Figure A.1: Typical f_{CEO} beat signal at 20 MHz. The SNR should be at least 30 dB.

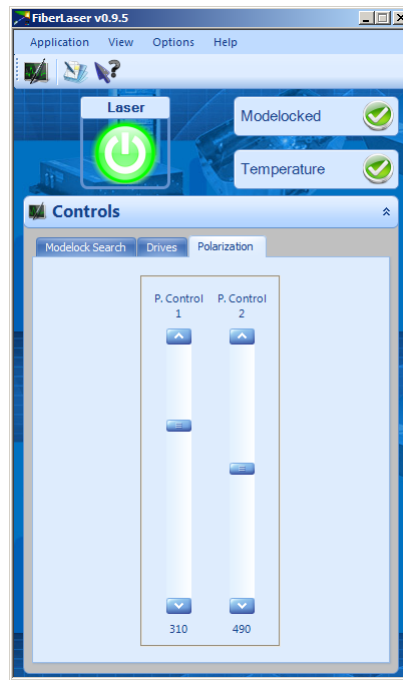
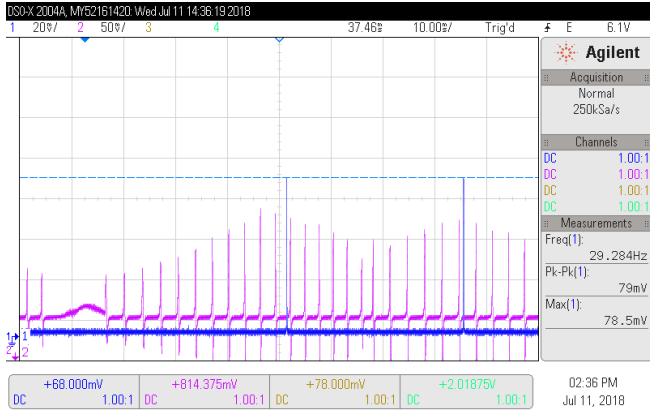


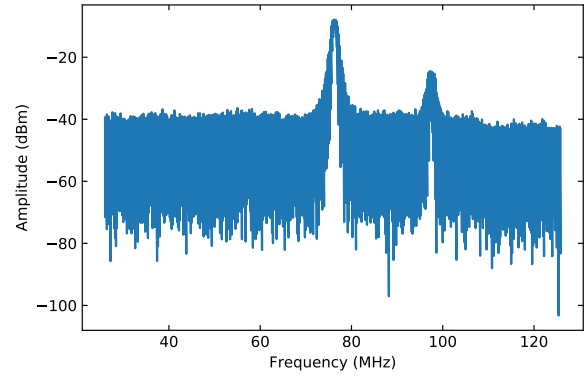
Figure A.2: Screenshot of the FiberLaser tool. The shown scroll bars are used to minimize the output of the monitor port.

not, temperature tune the corresponding cavity to see neighboring modes and choose the mode with the highest transmission signal.

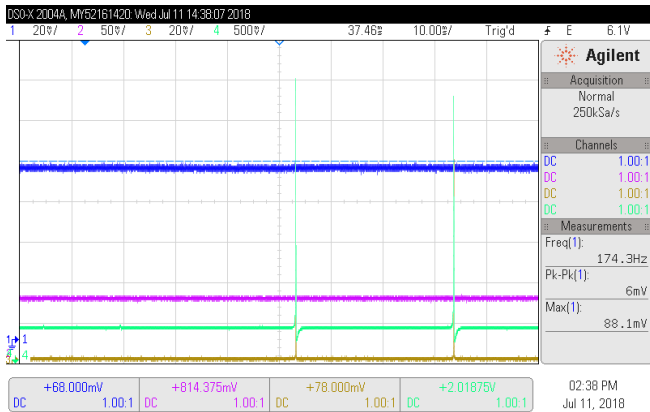
7. Turn on the arbitrary waveform generator (AWG) and in TrICS start the UserAPI process `ultrafast_electronics`. This process initializes both the AWG and the high power erbium doped fiber amplifier (EDFA), and allows the user to control them.
8. Activate both output channels of the AWG. Channel 1 should now output the idle signal (see section 5.3.1), channel 2 a 156 MHz clock signal for the delay generator (see figure 5.6).
9. Turn on the driver and the bias control of the pulse picker.
10. Next, the AWG phase and the pulse picker's DC bias voltage have to be adjusted: The AWG's sample rate of 25 GS/s is five times the repetition rate of the unpicked pulse train of 5 GHz. Therefore, the phase of the AWG can take one of five values. The manual delay of the pulse picker is adjusted such that these values are one of $\{n \cdot 180^\circ \mid n \in \{0, \pm 1, \pm 2\}\}$. The value usually



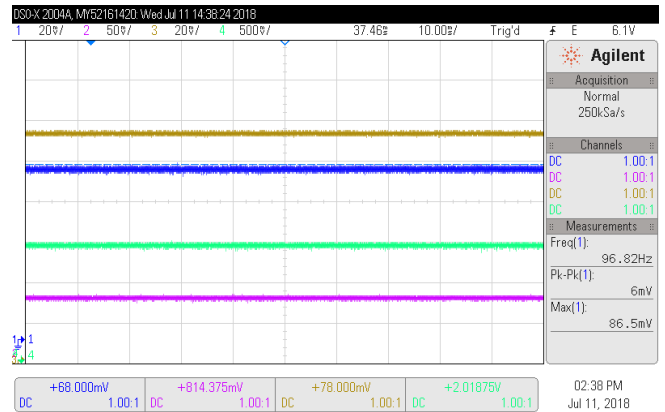
(a) Typical transmission signals of unlocked cavity 1 while modulating its length. Blue: CW laser transmission (also unlocked), purple: frequency comb transmission. Care must be taken to lock the CW laser to the frequency comb mode with the highest transmission signal.



(b) Typical beat note between the frequency comb and the auxiliary CW laser at 76 MHz. The SNR should be at least 30 dB. The smaller peak at 98 MHz is a higher order sideband and can be ignored.



(c) Typical transmission signals of locked cavity 1 and unlocked cavity 2 while modulating its length. Blue: CW laser transmission (locked to comb) through cavity 1, purple: frequency comb transmission through cavity 1, yellow: CW laser transmission (locked to comb) through cavity 2, green: frequency comb transmission through cavity 2.



(d) Typical transmission signals of locked cavities 1 and 2. Blue: CW laser transmission (locked to comb) through cavity 1, purple: frequency comb transmission through cavity 1, yellow: CW laser transmission (locked to comb) through cavity 2, green: frequency comb transmission through cavity 2.

Figure A.3: Cavity lock signals

only changes if the [AWG](#) loses its 250 MHz clock signal from the frequency comb. The correct value maximizes the output power of the pulse picker, but only if the DC bias voltage is at least roughly right (see next item).

11. Usually, the DC bias voltage should be between -7 V and -5 V . The exact value depends on the repetition rate of the idle signal and is subject to drift. It therefore has to be adjusted at least about once per day and every time the repetition rate of the idle signal is changed. A correct value maximizes the extinction ratio between wanted and unwanted pulses. It can be determined in two different ways. If the repetition rate of the idle signal is anything but the full 5 GHz, the DC bias voltage can be adjusted such that the light power of the doubled light at either 786 nm or 393 nm is maximized. Alternatively, the extinction ratio can be observed on an oscilloscope by using any sequence that picks at least some pulses and detecting the light on a fast photodiode.

Typically, the system is prepared in the single pulses mode (see page [62](#)) and the residual 786 nm light after the second second harmonic generation ([SHG](#)) stage is detected: Either start the User-API process `ultrafast_dg_single_pulses` or manually load the `single_pulse_workaround.g0x` file into the delay generator software. Load the sequence `general_pulses_ultrafast.py` in [TrICS](#) and the Check DC bias settings on the fast oscilloscope. This should now display the [AWG](#)'s electrical signal and the corresponding optical signal once the amplifiers are turned on. Adjust the DC bias voltage such that the optical signal during the dark time (compare with figure [5.10](#) on page [63](#)) is minimized.

12. Next, the fiber coupling needs to be optimized. In order to be able to just switch the barium borate ([BBO](#)) Pockels cell – and therefore the 393 nm light – on or off, either stop the UserAPI process `ultrafast_dg_single_pulses` and instead start `ultrafast_dg_general_pulse`, or load the `BBO_general_pulse_test.g0x` file into the delay generator software. In [TrICS](#), switch the channel `393_DG_gate` on, off and on again. The 393 nm light should now be continuously on, and the fiber coupling can be optimized.
13. Finally, the alignment of the light with the ion has to be optimized. Switch off the `393_DG_gate` channel and load the sequence `general_pulse_ultrafast.py` into [TrICS](#). Starting with a

long pulse length ($>100\text{ }\mu\text{s}$) if necessary, maximize the excitation probability by aligning the laser with the ion with the help of the motorized fiber collimator holder¹. Typically, the maximum excitation probability is 75 % for 15 % pump power level, 5 GHz idle repetition rate, $0.5\text{ }\mu\text{s}$ pulse length and $f_{\text{DDS}} = 19\,999\,960\text{ Hz}$.

¹ New Focus Picomotor

The experiment described in this thesis would not have been possible without the research group in which it was conducted. Experiments such as this one take more work than can be performed in a single thesis' time. They have become so complicated that no single scientist knows every single aspect of his or her experiment. Likewise, the development of the software that controls these experiments takes a collaboration effort, at least among the members of the research group. Most notably, much of [TrICS](#) was developed by Thomas Holleis, our former full-time developer. He did almost all of the C++ heavy lifting in the [TrICS](#) GUI and daemon. Other major contributors will be mentioned in the respective sections without the claim to be exhaustive.

[TrICS](#) is split into three parts: the *GUI*, the *daemon*, and *trixit*, see the blue panel in figure [B.1](#). Independent of, but closely linked to [TrICS](#) are the *sequencer2*, the program controlling the pulse box, and the [WLM server](#), which controls the wavelength meter ([WLM](#)).

B.1 TRICS GUI

The GUI is the part of [TrICS](#) with which the user typically comes into contact first and with which the user interacts the most. It is written in C++ and uses the Qt toolkit for displaying the user interface. It communicates with the other components of [TrICS](#) via D-Bus and enables them to read and change input field values. The GUI allows the user to control connected hardware and conduct experiments by changing parameters such as frequencies, powers and timings. It calculates transition frequencies between qubit states of different ion species based on a laser offset, the magnetic field at the point of the ion, and the magnetic quantum numbers of the states. Measurement results are displayed in different histograms and plots.

UserAPI

The UserAPI is a way for the user to quickly implement new features. It is the preferred way to add new hardware to [TrICS](#). A few example

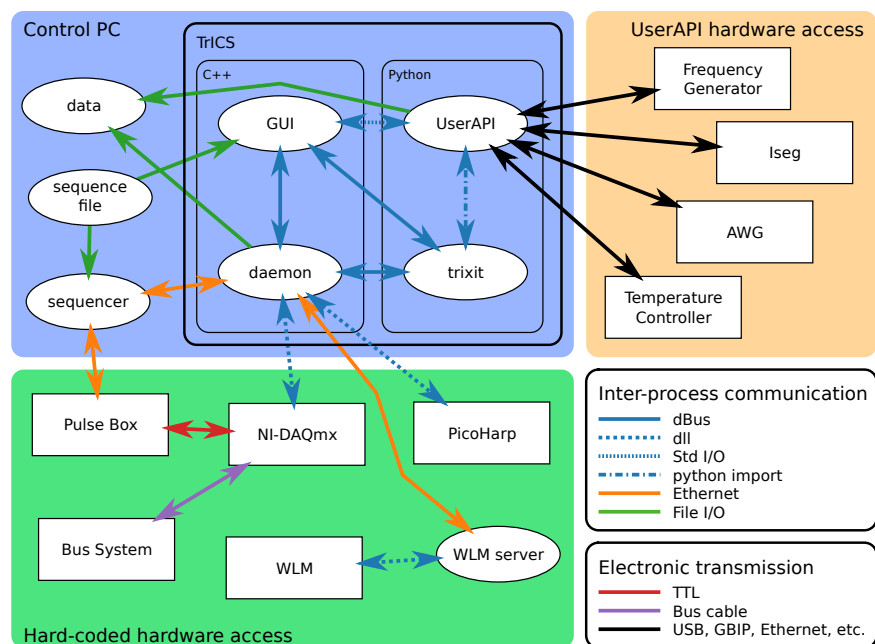


Figure B.1: Schematic overview of the experiment control software. Software programs are represented by ellipses, hardware devices by rectangles. Arrows indicate a form of communication between two entities, with the arrow head pointing in the direction of communication, and color and shape of the arrow line indicating the form of communication (see legend).

hardware devices are pictured in the yellow panel of figure B.1. The UserAPI consists of two parts: an event-based control which is part of the [TrICS](#) GUI and UserAPI processes. UserAPI processes are external programs that are launched by the control part and react to events. Events are emitted by e.g. a change of a parameter or the start and end of an experiment. The reference implementation of the UserAPI processes is written in python, which is the reason that all current UserAPI processes are python scripts. This allows the user to easily put any device – hardware or software – that can be controlled via python under control of [TrICS](#). Bernardo Casabone came up with the initial concept of the UserAPI, Bryan Luu developed the control part within the [TrICS](#) GUI and I programmed the reference implementation of the UserAPI process.

B.2 TRICS DAEMON

The [TrICS](#) daemon is a separate program that runs in the background. Like the GUI, it is written in C++ and communicates with the other components of [TrICS](#) via D-Bus. The daemon coordinates the experimental queue and handles the communication with hard-coded hardware which is pictured in the green panel of figure B.1. In particular, it takes control of any installed and configured NI-DAQmx card, which are used to communicate with the pulse box, count photomultiplier tube (PMT) pulses and control the bus system. Furthermore, the daemon can periodically execute scripts for automated measurements. This feature is called the *script manager* and is controlled via a separate python GUI.

B.3 TRIKIT

Trikit is a python module which allows the user to control [TrICS](#) via python scripts. Via trikit, the user can read and change any [TrICS](#) GUI parameter, set-up and queue scans, and receive measurement results for post-processing. Noteably and together with the daemon's script manager, trikit allows for automatically measuring, analyzing, and compensating for drifting laser offset frequencies and magnetic fields. Other typical use cases are n -dimensional scans, i.e. systematically changing n experimental parameters, and repeating the same measurement time and again, e.g. to initialize experimental parameters

in the morning. Trixit development was started by Florian Zähringer and continued by me.

B.4 VERSION CONTROL AND CONTINUOUS INTEGRATION

The [TrICS](#) source code is hosted in a git repository on a university server. Every new commit pushed to the repository is automatically checked out and built by a continuous integration server. The server is a Debian based Docker container that cross compiles [TrICS](#) for the 32-bit Windows architecture and uploads the compiled binaries together with all necessary libraries back to the university server.

BIBLIOGRAPHY

- [1] A. M. Turing. "On Computable Numbers, with an Application to the Entscheidungsproblem." In: *Proc. London Math. Soc.* s2-42.1 (1937), pp. 230–265. DOI: [10.1112/plms/s2-42.1.230](https://doi.org/10.1112/plms/s2-42.1.230).
- [2] G. E. Moore. "Cramming More Components onto Integrated Circuits." In: *Electronics* 38.8 (Jan. 1965), pp. 114–117.
- [3] P. Benioff. "The computer as a physical system: A microscopic quantum mechanical Hamiltonian model of computers as represented by Turing machines." In: *J. Stat. Phys.* 22.5 (May 1980), pp. 563–591. DOI: [10.1007/BF01011339](https://doi.org/10.1007/BF01011339).
- [4] R. P. Feynman. "Simulating physics with computers." In: *Int. J. Theor. Phys.* 21.6-7 (June 1982), pp. 467–488. DOI: [10.1007/BF02650179](https://doi.org/10.1007/BF02650179).
- [5] S. Lloyd. "Universal Quantum Simulators." In: *Science* (80-.). 273.5278 (Aug. 1996), pp. 1073–1078. DOI: [10.1126/science.273.5278.1073](https://doi.org/10.1126/science.273.5278.1073).
- [6] P. W. Shor. "Polynomial-Time Algorithms for Prime Factorization and Discrete Logarithms on a Quantum Computer." In: *SIAM J. Comput.* 26.5 (Oct. 1997), pp. 1484–1509. DOI: [10.1137/S0097539795293172](https://doi.org/10.1137/S0097539795293172).
- [7] D. Deutsch and R. Jozsa. "Rapid Solution of Problems by Quantum Computation." In: *Proc. R. Soc. A Math. Phys. Eng. Sci.* 439.1907 (Dec. 1992), pp. 553–558. DOI: [10.1098/rspa.1992.0167](https://doi.org/10.1098/rspa.1992.0167).
- [8] Lov K. Grover. "A fast quantum mechanical algorithm for database search." In: *Proc. twenty-eighth Annu. ACM Symp. Theory Comput. - STOC '96*. New York, New York, USA: ACM Press, 1996, pp. 212–219. DOI: [10.1145/237814.237866](https://doi.org/10.1145/237814.237866).
- [9] P. W. Shor. "Scheme for reducing decoherence in quantum computer memory." In: *Phys. Rev. A* 52.4 (Oct. 1995), R2493–R2496. DOI: [10.1103/PhysRevA.52.R2493](https://doi.org/10.1103/PhysRevA.52.R2493).

- [10] A. Steane. "Multiple-particle interference and quantum error correction." In: *Proc. R. Soc. London. Ser. A Math. Phys. Eng. Sci.* 452.1954 (Nov. 1996), pp. 2551–2577. DOI: [10.1098/rspa.1996.0136](https://doi.org/10.1098/rspa.1996.0136).
- [11] D. P. Divincenzo. "Topics in Quantum Computers." In: *Mesoscopic Electron Transp.* Dordrecht: Springer Netherlands, 1997, pp. 657–677. DOI: [10.1007/978-94-015-8839-3_18](https://doi.org/10.1007/978-94-015-8839-3_18).
- [12] J. I. Cirac and P. Zoller. "Quantum Computations with Cold Trapped Ions." In: *Phys. Rev. Lett.* 74.20 (May 1995), pp. 4091–4094. DOI: [10.1103/PhysRevLett.74.4091](https://doi.org/10.1103/PhysRevLett.74.4091).
- [13] D. Kielpinski, C. Monroe, and D. J. Wineland. "Architecture for a large-scale ion-trap quantum computer." In: *Nature* 417.6890 (June 2002), pp. 709–711. DOI: [10.1038/nature00784](https://doi.org/10.1038/nature00784).
- [14] D. J. Wineland et al. "Quantum information processing with trapped ions." In: *Philos. Trans. R. Soc. A Math. Phys. Eng. Sci.* 361.1808 (July 2003), pp. 1349–1361. DOI: [10.1098/rsta.2003.1205](https://doi.org/10.1098/rsta.2003.1205).
- [15] J. J. García-Ripoll, P. Zoller, and J. I. Cirac. "Quantum information processing with cold atoms and trapped ions." In: *J. Phys. B At. Mol. Opt. Phys.* 38.9 (May 2005), S567–S578. DOI: [10.1088/0953-4075/38/9/008](https://doi.org/10.1088/0953-4075/38/9/008).
- [16] H. Häffner, C. F. Roos, and R. Blatt. "Quantum computing with trapped ions." In: *Phys. Rep.* 469.4 (Dec. 2008), pp. 155–203. DOI: [10.1016/j.physrep.2008.09.003](https://doi.org/10.1016/j.physrep.2008.09.003).
- [17] F. Schmidt-Kaler, H. Häffner, M. Riebe, S. Gulde, G. P. T. Lancaster, T. Deuschle, C. Becher, C. F. Roos, J. Eschner, and R. Blatt. "Realization of the Cirac-Zoller controlled-NOT quantum gate." In: *Nature* 422.6930 (Mar. 2003), pp. 408–11. DOI: [10.1038/nature01494](https://doi.org/10.1038/nature01494).
- [18] D. Leibfried et al. "Experimental demonstration of a robust, high-fidelity geometric two ion-qubit phase gate." In: *Nature* 422.6930 (Mar. 2003), pp. 412–415. DOI: [10.1038/nature01492](https://doi.org/10.1038/nature01492).
- [19] C. J. Ballance, T. P. Harty, N. M. Linke, M. A. Sepiol, and D. M. Lucas. "High-Fidelity Quantum Logic Gates Using Trapped-Ion Hyperfine Qubits." In: *Phys. Rev. Lett.* 117.6 (Aug. 2016), p. 060504. DOI: [10.1103/PhysRevLett.117.060504](https://doi.org/10.1103/PhysRevLett.117.060504).

- [20] J. P. Gaebler et al. “High-Fidelity Universal Gate Set for $^9\text{Be}^+$ Ion Qubits.” In: *Phys. Rev. Lett.* 117.6 (Aug. 2016), p. 060505. DOI: [10.1103/PhysRevLett.117.060505](https://doi.org/10.1103/PhysRevLett.117.060505).
- [21] F. Schmidt-Kaler et al. “How to realize a universal quantum gate with trapped ions.” In: *Appl. Phys. B* 77.8 (Dec. 2003), pp. 789–796. DOI: [10.1007/s00340-003-1346-9](https://doi.org/10.1007/s00340-003-1346-9).
- [22] P. Schindler et al. “A quantum information processor with trapped ions.” In: *New J. Phys.* 15.12 (Dec. 2013), p. 123012. DOI: [10.1088/1367-2630/15/12/123012](https://doi.org/10.1088/1367-2630/15/12/123012).
- [23] S. Debnath, N. M. Linke, C. Figgatt, K. A. Landsman, K. Wright, and C. Monroe. “Demonstration of a small programmable quantum computer with atomic qubits.” In: *Nature* 536.7614 (Aug. 2016), pp. 63–66. DOI: [10.1038/nature18648](https://doi.org/10.1038/nature18648).
- [24] J. J. García-Ripoll, P. Zoller, and J. I. Cirac. “Speed Optimized Two-Qubit Gates with Laser Coherent Control Techniques for Ion Trap Quantum Computing.” In: *Phys. Rev. Lett.* 91.15 (Oct. 2003), p. 157901. DOI: [10.1103/PhysRevLett.91.157901](https://doi.org/10.1103/PhysRevLett.91.157901).
- [25] L.-M. Duan. “Scaling Ion Trap Quantum Computation through Fast Quantum Gates.” In: *Phys. Rev. Lett.* 93.10 (Sept. 2004), p. 100502. DOI: [10.1103/PhysRevLett.93.100502](https://doi.org/10.1103/PhysRevLett.93.100502).
- [26] J. J. García-Ripoll, P. Zoller, and J. I. Cirac. “Coherent control of trapped ions using off-resonant lasers.” In: *Phys. Rev. A* 71.6 (June 2005), p. 062309. DOI: [10.1103/PhysRevA.71.062309](https://doi.org/10.1103/PhysRevA.71.062309).
- [27] C. D. B. Bentley, A. R. R. Carvalho, D. Kielpinski, and J. J. Hope. “Fast gates for ion traps by splitting laser pulses.” In: *New J. Phys.* 15.4 (Apr. 2013), p. 043006. DOI: [10.1088/1367-2630/15/4/043006](https://doi.org/10.1088/1367-2630/15/4/043006).
- [28] C. D. B. Bentley, A. R. R. Carvalho, and J. J. Hope. “Trapped ion scaling with pulsed fast gates.” In: *New J. Phys.* 17.10 (Oct. 2015), p. 103025. DOI: [10.1088/1367-2630/17/10/103025](https://doi.org/10.1088/1367-2630/17/10/103025).
- [29] R. L. Taylor, C. D. B. Bentley, J. S. Pedernales, L. Lamata, E. Solano, A. R. R. Carvalho, and J. J. Hope. “A Study on Fast Gates for Large-Scale Quantum Simulation with Trapped Ions.” In: *Sci. Rep.* 7.1 (Dec. 2017), p. 46197. DOI: [10.1038/srep46197](https://doi.org/10.1038/srep46197).
- [30] J. Mizrahi, B. Neyenhuis, K. G. Johnson, W. C. Campbell, C. Senko, D. Hayes, and C. Monroe. “Quantum control of qubits and atomic motion using ultrafast laser pulses.” In: *Appl. Phys. B* 114.1-2 (Jan. 2014), pp. 45–61. DOI: [10.1007/s00340-013-5717-6](https://doi.org/10.1007/s00340-013-5717-6).

- [31] M. I. Hussain, M. J. Petراسiunas, C. D. B. Bentley, R. L. Taylor, A. R. R. Carvalho, J. J. Hope, E. W. Streed, M. Lobino, and D. Kielpinski. "Ultrafast, high repetition rate, ultraviolet, fiber-laser-based source: application towards Yb+ fast quantum-logic." In: *Opt. Express* 24.15 (July 2016), p. 16638. DOI: [10.1364/OE.24.016638](https://doi.org/10.1364/OE.24.016638).
- [32] M. J. Madsen, D. L. Moehring, P. Maunz, R. N. Kohn, L.-M. Duan, and C. Monroe. "Ultrafast Coherent Excitation of a Trapped Ion Qubit for Fast Gates and Photon Frequency Qubits." In: *Phys. Rev. Lett.* 97.4 (July 2006), p. 040505. DOI: [10.1103/PhysRevLett.97.040505](https://doi.org/10.1103/PhysRevLett.97.040505).
- [33] W. C. Campbell, J. Mizrahi, Q. Quraishi, C. Senko, D. Hayes, D. Hucul, D. N. Matsukevich, P. Maunz, and C. Monroe. "Ultrafast Gates for Single Atomic Qubits." In: *Phys. Rev. Lett.* 105.9 (Aug. 2010), p. 090502. DOI: [10.1103/PhysRevLett.105.090502](https://doi.org/10.1103/PhysRevLett.105.090502).
- [34] J. Mizrahi, C. Senko, B. Neyenhuis, K. G. Johnson, W. C. Campbell, C. W. S. Conover, and C. Monroe. "Ultrafast Spin-Motion Entanglement and Interferometry with a Single Atom." In: *Phys. Rev. Lett.* 110.20 (May 2013), p. 203001. DOI: [10.1103/PhysRevLett.110.203001](https://doi.org/10.1103/PhysRevLett.110.203001).
- [35] J. D. Wong-Campos, S. A. Moses, K. G. Johnson, and C. Monroe. "Demonstration of Two-Atom Entanglement with Ultrafast Optical Pulses." In: *Phys. Rev. Lett.* 119.23 (Dec. 2017), p. 230501. DOI: [10.1103/PhysRevLett.119.230501](https://doi.org/10.1103/PhysRevLett.119.230501).
- [36] V. M. Schäfer, C. J. Ballance, K. Thirumalai, L. J. Stephenson, T. G. Ballance, A. M. Steane, and D. M. Lucas. "Fast quantum logic gates with trapped-ion qubits." In: *Nature* 555.7694 (Feb. 2018), pp. 75–78. DOI: [10.1038/nature25737](https://doi.org/10.1038/nature25737).
- [37] A. Jechow, M. J. Petراسiunas, M. G. Pullen, J. Canning, M. Stevenson, P. S. Westbrook, K. S. Feder, and D. Kielpinski. "High-power ultrafast laser source with 300 MHz repetition rate for trapped-ion quantum logic." In: *2011 Conf. Lasers Electro-Optics Eur. 12th Eur. Quantum Electron. Conf. (CLEO Eur. IEEE, May 2011, pp. 1–1*. DOI: [10.1109/CLEOE.2011.5943009](https://doi.org/10.1109/CLEOE.2011.5943009).
- [38] P. K. Ghosh. *Ion Traps*. Oxford: Clarendon Press, 1995. ISBN: 0198539959.
- [39] A. Steane. "The ion trap quantum information processor." In: *Appl. Phys. B Lasers Opt.* 64.6 (June 1997), pp. 623–643. DOI: [10.1007/s003400050225](https://doi.org/10.1007/s003400050225).

- [40] M. Guggemos. “Precision spectroscopy with trapped $^{40}\text{Ca}^+$ and $^{27}\text{Al}^+$ ions.” PhD thesis. University of Innsbruck, 2017. URL: https://quantumoptics.at/images/publications/dissertation/2017_guggemos_diss.pdf.
- [41] M. Guggemos, D. Heinrich, Ó. A. Herrera-Sancho, R. Blatt, and C. F. Roos. “Sympathetic cooling and detection of a hot trapped ion by a cold one.” In: *New J. Phys.* 17.10 (2015), p. 103001. DOI: [10.1088/1367-2630/17/10/103001](https://doi.org/10.1088/1367-2630/17/10/103001).
- [42] C. Cohen-Tannoudji, B. Diu, and F. Laloe. *Quantum Mechanics Vol. I*. John Wiley & Sons, 1977. ISBN: 047116433X.
- [43] W. P. Schleich. *Quantum Optics in Phase Space*. 2001. ISBN: 3-527-29435-X.
- [44] D. F. V. James. “Quantum dynamics of cold trapped ions with application to quantum computation.” In: *Appl. Phys. B Lasers Opt.* 66.2 (Feb. 1998), pp. 181–190. DOI: [10.1007/s003400050373](https://doi.org/10.1007/s003400050373).
- [45] C. Hempel. “Digital quantum simulation, Schrödinger cat state spectroscopy and setting up a linear ion trap.” PhD thesis. University of Innsbruck, 2014. URL: http://www.quantumoptics.at/images/publications/dissertation/hempel_diss.pdf.
- [46] C. Cohen-Tannoudji, B. Diu, and F. Laloe. *Quantum Mechanics, Vol. II*. John Wiley & Sons, 1977. ISBN: 0471164356.
- [47] J. Benhelm. “Precision spectroscopy and quantum information processing with trapped calcium ions.” PhD thesis. University of Innsbruck, 2008. URL: https://quantumoptics.at/images/publications/dissertation/benhelm_diss.pdf.
- [48] R. Gerritsma, G. Kirchmair, F. Zähringer, J. Benhelm, R. Blatt, and C. F. Roos. “Precision measurement of the branching fractions of the $4p\ ^2P_{3/2}$ decay of Ca II.” In: *Eur. Phys. J. D* 50.1 (Nov. 2008), pp. 13–19. DOI: [10.1140/epjd/e2008-00196-9](https://doi.org/10.1140/epjd/e2008-00196-9).
- [49] M. Ramm, T. Pruttivarasin, M. Kokish, I. Talukdar, and H. Häffner. “Precision Measurement Method for Branching Fractions of Excited $P_{1/2}$ States Applied to $^{40}\text{Ca}^+$.” In: *Phys. Rev. Lett.* 111.2 (July 2013), p. 023004. DOI: [10.1103/PhysRevLett.111.023004](https://doi.org/10.1103/PhysRevLett.111.023004).
- [50] J. Jin and D. A. Church. “Precision lifetimes for the $\text{Ca}^+ 4p\ ^2P$ Levels: Experiment Challenges Theory at the 1% Level.” In: *Phys. Rev. Lett.* 70.21 (May 1993), pp. 3213–3216. DOI: [10.1103/PhysRevLett.70.3213](https://doi.org/10.1103/PhysRevLett.70.3213).

- [51] P. A. Barton, C. J. S. Donald, D. M. Lucas, D. A. Stevens, A. M. Steane, and D. N. Stacey. "Measurement of the lifetime of the $3d\ ^2D_{5/2}$ state in $^{40}\text{Ca}^+$." In: *Phys. Rev. A* 62.3 (Aug. 2000), p. 032503. DOI: [10.1103/PhysRevA.62.032503](https://doi.org/10.1103/PhysRevA.62.032503).
- [52] A. Kreuter et al. "Experimental and theoretical study of the $3d\ ^2D$ -level lifetimes of $^{40}\text{Ca}^+$." In: *Phys. Rev. A* 71.3 (Mar. 2005), p. 032504. DOI: [10.1103/PhysRevA.71.032504](https://doi.org/10.1103/PhysRevA.71.032504).
- [53] D. Leibfried, R. Blatt, C. Monroe, and D. J. Wineland. "Quantum dynamics of single trapped ions." In: *Rev. Mod. Phys.* 75.1 (Mar. 2003), pp. 281–324. DOI: [10.1103/RevModPhys.75.281](https://doi.org/10.1103/RevModPhys.75.281).
- [54] C. C. Gerry and P. L. Knight. *Introductory quantum optics*. Cambridge: Cambridge Univ. Press, 2006. ISBN: 978-0-521-52735-4.
- [55] C. Cohen-Tannoudji, J. Dupont-Roc, and G. Grynberg. *Photons and Atoms*. Wiley, Mar. 1997. ISBN: 9780471184331. DOI: [10.1002/9783527618422](https://doi.org/10.1002/9783527618422).
- [56] C. D. B. Bentley. "Fast gates and steady states: entangling trapped ions." PhD thesis. Australian National University, 2015. URL: <https://openresearch-repository.anu.edu.au/bitstream/1885/104996/1/BentleyThesis%202016.pdf>.
- [57] J F Poyatos, J I Cirac, R. Blatt, and P Zoller. "Trapped ions in the strong-excitation regime: Ion interferometry and nonclassical states." In: *Phys. Rev. A* 54.2 (Aug. 1996), pp. 1532–1540. DOI: [10.1103/PhysRevA.54.1532](https://doi.org/10.1103/PhysRevA.54.1532).
- [58] R. Trebino, K. W. DeLong, D. N. Fittinghoff, J. N. Sweetser, M. A. Krumbügel, B. A. Richman, and D. J. Kane. "Measuring ultrashort laser pulses in the time-frequency domain using frequency-resolved optical gating." In: *Rev. Sci. Instrum.* 68.9 (Sept. 1997), pp. 3277–3295. DOI: [10.1063/1.1148286](https://doi.org/10.1063/1.1148286).
- [59] V. S. Malinovsky and J. L. Krause. "General theory of population transfer by adiabatic rapid passage with intense, chirped laser pulses." In: *Eur. Phys. J. D* 14.2 (May 2001), pp. 147–155. DOI: [10.1007/s100530170212](https://doi.org/10.1007/s100530170212).
- [60] D. Deutsch. "Quantum Theory, the Church-Turing Principle and the Universal Quantum Computer." In: *Proc. R. Soc. A Math. Phys. Eng. Sci.* 400.1818 (July 1985), pp. 97–117. DOI: [10.1098/rspa.1985.0070](https://doi.org/10.1098/rspa.1985.0070).

- [61] M. A. Nielsen and I. L. Chuang. *Quantum Computation and Quantum Information*. Cambridge: Cambridge University Press, 2010. DOI: [10.1017/CB09780511976667](https://doi.org/10.1017/CB09780511976667).
- [62] V. Nebendahl, H. Häffner, and C. F. Roos. “Optimal control of entangling operations for trapped-ion quantum computing.” In: *Phys. Rev. A* 79.1 (Jan. 2009), p. 012312. DOI: [10.1103/PhysRevA.79.012312](https://doi.org/10.1103/PhysRevA.79.012312).
- [63] C. D. B. Bentley, R. L. Taylor, A. R. R. Carvalho, and J. J. Hope. “Stability thresholds and calculation techniques for fast entangling gates on trapped ions.” In: *Phys. Rev. A* 93.4 (Apr. 2016), p. 042342. DOI: [10.1103/PhysRevA.93.042342](https://doi.org/10.1103/PhysRevA.93.042342).
- [64] X. Long, S. S. Yu, A. M. Jayich, and W. C. Campbell. *Suppressed spontaneous emission for coherent momentum transfer*. 2019. arXiv: [1903.01627](https://arxiv.org/abs/1903.01627).
- [65] D. Heinrich, M. Guggemos, M. Guevara-Bertsch, M. I. Hussain, C. F. Roos, and R. Blatt. “Ultrafast coherent excitation of a $^{40}\text{Ca}^+$ ion.” In: *New J. Phys.* 21.7 (2019), p. 073017. DOI: [10.1088/1367-2630/ab2a7e](https://doi.org/10.1088/1367-2630/ab2a7e).
- [66] D. Strickland and G. Mourou. “Compression of amplified chirped optical pulses.” In: *Opt. Commun.* 56.3 (Dec. 1985), pp. 219–221. DOI: [10.1016/0030-4018\(85\)90120-8](https://doi.org/10.1016/0030-4018(85)90120-8).
- [67] G. P. Agrawal and N. A. Olsson. “Self-phase modulation and spectral broadening of optical pulses in semiconductor laser amplifiers.” In: *IEEE J. Quantum Electron.* 25.11 (1989), pp. 2297–2306. DOI: [10.1109/3.42059](https://doi.org/10.1109/3.42059).
- [68] D. Heinrich, M. Guggemos, M. Guevara-Bertsch, M. I. Hussain, C. F. Roos, and R. Blatt. *Ultrafast coherent excitation of a $^{40}\text{Ca}^+$ ion*. 2018. arXiv: [1812.08537v1](https://arxiv.org/abs/1812.08537v1).
- [69] D. J. Kane and R. Trebino. “Characterization of arbitrary femtosecond pulses using frequency-resolved optical gating.” In: *IEEE J. Quantum Electron.* 29.2 (1993), pp. 571–579. DOI: [10.1109/3.199311](https://doi.org/10.1109/3.199311).
- [70] R. Trebino and D. J. Kane. “Using phase retrieval to measure the intensity and phase of ultrashort pulses: frequency-resolved optical gating.” In: *J. Opt. Soc. Am. A* 10.5 (May 1993), p. 1101. DOI: [10.1364/JOSAA.10.001101](https://doi.org/10.1364/JOSAA.10.001101).

- [71] K. W. DeLong, R. Trebino, J. Hunter, and W. E. White. "Frequency-resolved optical gating with the use of second-harmonic generation." In: *J. Opt. Soc. Am. B* 11.11 (Nov. 1994), p. 2206. DOI: [10.1364/JOSAB.11.002206](https://doi.org/10.1364/JOSAB.11.002206).
- [72] S. Linden, H. Giessen, and J. Kuhl. "XFROG – A New Method for Amplitude and Phase Characterization of Weak Ultrashort Pulses." In: *Phys. status solidi* 206.1 (Mar. 1998), pp. 119–124. DOI: [10.1002/\(SICI\)1521-3951\(199803\)206:1<119::AID-PSSB119>3.0.CO;2-X](https://doi.org/10.1002/(SICI)1521-3951(199803)206:1<119::AID-PSSB119>3.0.CO;2-X).
- [73] S. Linden, J. Kuhl, and H. Giessen. "Amplitude and phase characterization of weak blue ultrashort pulses by downconversion." In: *Opt. Lett.* 24.8 (Apr. 1999), p. 569. DOI: [10.1364/OL.24.000569](https://doi.org/10.1364/OL.24.000569).
- [74] R. Paschotta. *Time–bandwidth Product*. URL: https://www.rp-photonics.com/time_bandwidth_product.html (visited on 07/10/2018).
- [75] D. J. Kane. "Real-time measurement of ultrashort laser pulses using principal component generalized projections." In: *IEEE J. Sel. Top. Quantum Electron.* 4.2 (1998), pp. 278–284. DOI: [10.1109/2944.686733](https://doi.org/10.1109/2944.686733).
- [76] R. J. Manning, A. D. Ellis, A. J. Poustie, and K. J. Blow. "Semiconductor laser amplifiers for ultrafast all-optical signal processing." In: *J. Opt. Soc. Am. B* 14.11 (Nov. 1997), p. 3204. DOI: [10.1364/JOSAB.14.003204](https://doi.org/10.1364/JOSAB.14.003204).
- [77] Z. V. Rizou, K. E. Zoiros, and M. J. Connelly. "Semiconductor Optical Amplifier Pattern Effect Suppression Using Optical Notch Filtering." In: *J. Eng. Sci. Technol. Rev.* 9.4 (Aug. 2016), pp. 198–201. DOI: [10.25103/jestr.094.28](https://doi.org/10.25103/jestr.094.28).
- [78] W. Paul and H. Steinwedel. "Notizen: Ein neues Massenspektrometer ohne Magnetfeld." In: *Zeitschrift für Naturforsch. A* 8.7 (Jan. 1953), p. 448. DOI: [10.1515/zna-1953-0710](https://doi.org/10.1515/zna-1953-0710).
- [79] S. Gulde. "Experimental Realization of Quantum Gates and the Deutsch-Jozsa Algorithm with Trapped $^{40}\text{Ca}^+$ Ions." PhD thesis. University of Innsbruck, 2003. URL: https://quantumoptics.at/images/publications/dissertation/gulde_diss.pdf.

- [80] G. Kirchmair. “Frequency stabilization of a Titanium-Sapphire laser for precision spectroscopy on Calcium ions.” diploma thesis. University of Innsbruck, 2006. URL: https://quantumoptics.at/images/publications/diploma/diplom_kirchmair.pdf.
- [81] M. F. Brandl. “Towards Cryogenic Scalable Quantum Computing with Trapped Ions.” PhD thesis. University of Innsbruck, 2017. URL: https://quantumoptics.at/images/publications/dissertation/brandl_diss_web.pdf.
- [82] P. Schindler. “Frequency synthesis and pulse shaping for quantum information processing with trapped ions.” diploma thesis. University of Innsbruck, 2008. URL: https://quantumoptics.at/images/publications/diploma/diplom_schindler.pdf.
- [83] F. Schreck. *Control system*. URL: <http://www.strontiumbec.com/> (visited on 07/11/2018).
- [84] C. Cohen-Tannoudji, J. Dupont-Roc, and G. Grynberg. *Atom—Photon Interactions*. Wiley, Apr. 1998. ISBN: 9780471293361. DOI: [10.1002/9783527617197](https://doi.org/10.1002/9783527617197).
- [85] J. R. Johansson, P. D. Nation, and F. Nori. “QuTiP: An open-source Python framework for the dynamics of open quantum systems.” In: *Comput. Phys. Commun.* 183.8 (Aug. 2012), pp. 1760–1772. DOI: [10.1016/j.cpc.2012.02.021](https://doi.org/10.1016/j.cpc.2012.02.021).
- [86] J. R. Johansson, P. D. Nation, and F. Nori. “QuTiP 2: A Python framework for the dynamics of open quantum systems.” In: *Comput. Phys. Commun.* 184.4 (Apr. 2013), pp. 1234–1240. DOI: [10.1016/j.cpc.2012.11.019](https://doi.org/10.1016/j.cpc.2012.11.019).
- [87] C. Cohen-Tannoudji and D. Guéry-Odelin. *Advances in Atomic Physics*. World Scientific, 2011. ISBN: 9789812774965.
- [88] D. J. Wineland and H. G. Dehmelt. “Proposed $10^{14} \delta\nu < \nu$ Laser Fluorescence Spectroscopy on Ti^+ Ion Mono-Oscillator.” In: *Bull. Am. Phys. Soc.* 20.637 (1975).
- [89] C. F. Roos, T. Zeiger, H. Rohde, H. C. Nägerl, J. Eschner, D. Leibfried, F. Schmidt-Kaler, and R. Blatt. “Quantum State Engineering on an Optical Transition and Decoherence in a Paul Trap.” In: *Phys. Rev. Lett.* 83.23 (Dec. 1999), pp. 4713–4716. DOI: [10.1103/PhysRevLett.83.4713](https://doi.org/10.1103/PhysRevLett.83.4713).

- [90] T. Zanon-Willette, E. de Clercq, and E. Arimondo. "Ultrahigh-resolution spectroscopy with atomic or molecular dark resonances: Exact steady-state line shapes and asymptotic profiles in the adiabatic pulsed regime." In: *Phys. Rev. A* 84.6 (Dec. 2011), p. 062502. DOI: [10.1103/PhysRevA.84.062502](https://doi.org/10.1103/PhysRevA.84.062502).
- [91] G. Boudebs and K. Fedus. "Absolute measurement of the non-linear refractive indices of reference materials." In: *J. Appl. Phys.* 105.10 (May 2009), p. 103106. DOI: [10.1063/1.3129680](https://doi.org/10.1063/1.3129680).

COLOPHON

This document was typeset using the typographical look-and-feel `classicthesis` developed by André Miede and Ivo Pletikosić. The style was inspired by Robert Bringhurst's seminal book on typography "*The Elements of Typographic Style*". `classicthesis` is available for both L^AT_EX and L^yX:

<https://bitbucket.org/amiede/classicthesis/>